Electron Detection Systems for KATRIN Detector and Spectrometer Section

Eric L. Martin

A dissertation
submitted in partial fulfillment of the
requirements for the degree of

Doctor of Philosophy

University of Washington

2017

Reading Committee:

R. G. Hamish Robertson, Chair

Peter Doe

Gray Rybka

Program Authorized to Offer Degree:
Physics

University of Washington

Abstract

Electron Detection Systems for KATRIN Detector and Spectrometer Section

Eric L. Martin

Chair of the Supervisory Committee:
Professor R. G. Hamish Robertson
Department of Physics

A time-of-flight mode is proposed for the upcoming KATRIN experiment β-decay spectrum measurement, and methods toward the necessary passive detection of a single electron through a large aperture are explored. A sub-fA current measurement was performed to determine the detector system's absolute detection efficiency, and faults in the silicon wafer were detected by an automated tester.

TABLE OF CONTENTS

Page

List of Figures iv

Chapter 1: Introduction to Neutrino Mass 1
1.1 A Brief History of Neutrinos 1
1.2 Neutrino Oscillation 6
1.3 Neutrino to Antineutrino Conversion 8
1.4 Indirect Neutrino Mass Measurement 10
1.5 Supernova Direct Neutrino Mass Measurement 11
1.6 Beta Decay Direct Neutrino Mass Measurement 12

Chapter 2: KATRIN 15
2.1 KATRIN Overview 15
2.2 MAC-E Filter 16
2.3 Detector 18
2.3.1 Calibration 21

Chapter 3: Electron Source Current Meter (PULCINELLA) 31
3.1 PULCINELLA Overview 31
3.1.1 LED Degradation 34
3.2 Detector Absolute Calibration 35
3.2.1 Correction for Emission from the Back of the Electron Source Disk . 36
3.2.2 Filtering 37

Chapter 4: Wafer Testing 41
4.1 Wafer Overview 41
4.2 KATRIN Focal-Plane Detector Performance Degradation 47
4.2.1 Interpixel Resistance 48

4.2.2 Sheet Resistance . . . 54
4.2.3 Forward Bias Resistance . . . 64
4.2.4 Wafer Testing Conclusions . . . 66

Chapter 5: MAC-E Time-of-Flight . . . 68
5.1 Time-of-Flight Overview . . . 68
5.2 Calculating Time-of-Flight Spectrum . . . 69
5.3 Electron Tagger . . . 71

Chapter 6: Electron Tagger . . . 72
6.1 Electron Tagger Methods Considered . . . 72
6.1.1 Cyclotron Radiation . . . 73
6.1.2 Image Charge . . . 74
6.1.3 Current Induced by Magnetic Field . . . 76
6.1.4 Image Current . . . 78
6.2 Energy Exchanged with Resonator . . . 79
6.2.1 Cylindrical Cavity TM_{010} . . . 81
6.2.2 Ring Resonator . . . 85
6.2.3 Energy Exchange with Cavity for Any Mode . . . 88
6.2.4 Readout Electronics . . . 93
6.2.5 Loop Pickup . . . 95
6.2.6 Improved Readout Technique . . . 105
6.2.7 Sense Current with SQUID . . . 114
6.3 Electron Tagger Conclusions . . . 114

Chapter 7: Electron Tagger Background . . . 116
7.1 Sources Considered . . . 116
7.1.1 Electrons Passing Through the Pre-spectrometer . . . 116
7.1.2 Electrons Trapped in the Penning Trap . . . 118
7.1.3 Penning Trap Wipers . . . 124

Chapter 8: Conclusions . . . 126

Bibliography . . . 128

Appendix A: Maximum Current and Instantaneous Charge Limits of FPD 136
A.1 Maximum Current Derivation 136
A.1.1 Deposition Disk to Cylinder 138
A.1.2 Hemispherical Region 139
A.1.3 Wafer Region 140
A.1.4 Wafer to Flange 141
A.1.5 Overall 141
A.2 Maximum Instantaneous Charge Derivation 141

Appendix B: Electron Source Illumination LED Drive Circuit 143
B.1 Description 143
B.2 Timing 145

LIST OF FIGURES

Figure Number		Page
1.1	Beta energy spectrum for tritium beta decay.	2
1.2	Normal and inverted neutrino mass hierarchy.	9
1.3	Neutrinoless double beta decay Feynman diagram	10
1.4	Tritium beta decay beta energy spectrum near the endpoint.	14
2.1	The KATRIN beam line.	16
2.2	MAC-E filter principle.	18
2.3	KATRIN detector section.	19
2.4	FPD wafer sectioning.	20
2.5	Detector calibration systems.	22
2.6	PULCINELLA bias filter electrical distribution.	24
2.7	Electron source probe.	25
2.8	Electron source disk illumination profile	27
2.9	Electron source disk and illumination device orientation.	28
2.10	Electron source illumination device.	29
2.11	UV LED mounting in the electron source illumination device.	30
3.1	PULCINELLA block diagram	32
3.2	Sample function fits for determining electron emission from the back of the electron source disk.	38
3.3	Back-of-disk current function fit values.	39
3.4	Current noise measured by PULCINELLA.	40
4.1	Wafer mounting assembly.	42
4.2	FPD wafer tester assembly drawing.	43
4.3	FPD wafer tester measurement circuit.	45
4.4	FPD wafer circuit model.	48
4.5	FPD wafer pin layout	49

4.6 FPD wafer interpixel resistance test board. 51
4.7 FPD wafer interpixel resistance measurement circuit. 52
4.8 FPD wafer 1115876. 55
4.9 Wafer 76040 sheet resistance fits. 61
4.10 Wafer 115876 sheet resistance fits. 63
4.11 Diode and series resistor current vs. voltage example. 65

5.1 Electric potential and magnetic field along axis of KATRIN main spectrometer. 70
5.2 Time-of-flight spectra. 70

6.1 Expected blackbody background to cyclotron radiation. 74
6.2 Charge transformer. 76
6.3 Cylindrical cavity. 84
6.4 Ring resonator. 86
6.5 Ring resonator electric field, axial (z) component. 87
6.6 Mean cavity energy exchange squared. 91
6.7 Cavity readout electronics. 93
6.8 Zero volt equipotential cross section for a ring of charge and a point charge. 100
6.9 Comparison of image charge calculated by simple model to best fit approximation using ring of charge and point charge. 101
6.10 Loop pickup response. 103
6.11 Expected signal and readout sample points. 105
6.12 Loop and LC π resonator signal-to-noise. 112

7.1 Rate of source electrons passing the electron tagger. 118
7.2 Rate of source electrons trapped due to cyclotron radiation. 122
7.3 Rate of electrons trapped due to radiation passing the electron tagger. 123

A.1 Heat transfer stages used to calculate maximum charge deposition in FPD. . 137

B.1 LED timing circuit. 144
B.2 UV LED driver circuit. 147
B.3 Red LED sensor circuit. 148

ACKNOWLEDGMENTS

I would like to thank my advisor, Hamish Robertson. He not only provided continuous support and direction, he was also a tremendous role model. Hopefully some of his positive attitude rubbed off along with his ingenuity. I would also like to thank Tim Van Wechel for his invaluable technical assistance. I owe a special thanks to my mentor, Peter Doe, who provided valuable guidance and feedback, and never bothers me about all the beer I owe him. Thank you to Diana Parno for her generous feedback on talks and papers.

My thanks to the flexible Gray Rybka for joining my reading committee on short notice. And thanks to the rest of my committee members: John Sahr, Boris Blinov, and especially Gerald Miller, who was also my academic advisor when I first began my graduate studies.

This material is based upon work supported by the U.S. Department of Energy, Office of Science, Office of Nuclear Physics under Award Number DE-FG02-97ER41020.

DEDICATION

Dedicated to my wonderful wife, Katherine, for her love, support, and especially her tolerance.

Chapter 1

INTRODUCTION TO NEUTRINO MASS

1.1 A Brief History of Neutrinos

In the early 20th century physicists faced a troublesome puzzle over beta decay experiments. Atoms were observed to decay into a single daughter nucleus by emitting a single electron, but the energy of the emitted electrons filled out a wide spectrum. When a single initial particle decays into two products, conservation of energy and momentum allow only a single value for the kinetic energy of each of the products.

Many thought electrons were emitted with a single energy and lost energy in secondary effects, which resulted in the observed energy spectrum. But, in 1927 Ellis and Wooster [1] performed a calorimeter experiment using bismuth-210. They showed the average electron energy from a spectrum measurement agreed with the average heat deposited in the calorimeter. This ruled out the possibility that secondary effects were responsible and called into question the validity of the law of conservation of energy. Some physicists were even ready to do away with energy conservation as a natural law.

In a letter to a conference on radioactivity in Tübingen in 1930, Pauli [2] proposed an explanation that preserved conservation of energy. He suggested there was a third, until then undetected, product of the decay. He postulated another subatomic particle contained in the atom, and named it the neutron. He expected it to be a spin $1/2$, neutral particle, with about the same mass as the electron. When another nucleon with about the same mass as the proton was discovered by Chadwick [3] in 1932 and dubbed the neutron, the missing third particle in beta decay was renamed the neutrino, meaning little neutral one, by Fermi.

In 1934 Fermi [4] introduced a theoretical model for beta decay. He based this model on particle creation and annihilation, similar to photons, and assumed the existence of neutrinos.

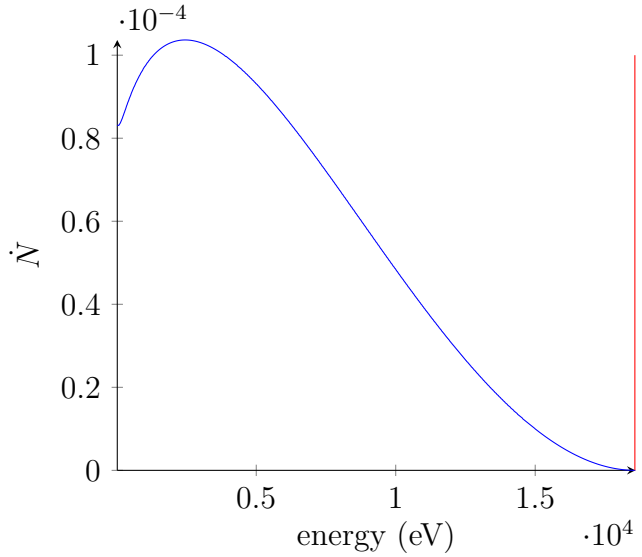

Figure 1.1: Beta energy spectrum for tritium beta decay, for two particle decay a single peak at 18.6 keV would be expected. The two curves are not to the same decay rate $\left(\dot{N}\right)$ scale.

His model showed that the shape of the energy spectrum was highly dependent on neutrino mass, especially at the end point, and Fermi noted that the spectra observed at the time were consistent with a neutrino mass of zero. His conclusion was that the neutrino mass was either zero, or it was far less massive than the electron and could be ignored. He assumed it was zero for further calculations — an assumption that took decades to finally prove incorrect.

Pauli was concerned he had predicted a particle that would never be detected, yet it only took two decades. Early calculations put the penetration power for neutrinos in matter at 10^{16} km [5], an estimate that is still considered decently accurate. Until nuclear fission reactors were developed, which provide an intense source of neutrinos, it was thought neutrinos could never be observed. Initial experiments to detect neutrinos from reactors relied on neutrino induced inverse beta decay of chlorine-37 to argon-37, proposed by Pontecorvo in 1946 [6].

$$\nu_e + {}^{37}Cl \rightarrow e^- + {}^{37}Ar \tag{1.1}$$

The argon was then collected and counted to determine how many interactions had occurred. However, the experiments failed to detect any argon from interaction with reactor neutrinos because, unknown at the time, the method only detects left-handed neutrinos and reactors only produce right-handed antineutrinos. Based on Fermi's work, along with the Dirac theory of positrons, it was postulated that a proton could capture a neutrino and produce a neutron and positron.

$$\bar{\nu}_e + p \rightarrow e^+ + n \tag{1.2}$$

Using the Savannah River reactor as an intense neutrino source, and observing gamma radiation from electron-positron annihilation of the positrons created from neutrino-induced inverse beta decay, the first direct detection of neutrinos was made in 1953 by Reines and Cowan [7].

Starting in 1954 Davis [8] performed experiments which established that neutrinos from reactors could produce positrons (equation 1.2), but could not produce electrons (equation 1.1). This showed that the neutrinos and antineutrinos interact differently, explaining why earlier reactor experiments failed. That decays producing electrons produced only antineutrinos is consistent with lepton number conservation and neutrinos and antineutrinos having different lepton number. But, it is also consistent with lepton number not being conserved, and the observed difference in the neutrinos being due to the parity violation of the charge current weak interaction. Possibly demonstrating that neutrinos and antineutrinos are the same particle is discussed further in section 1.3.

Helicity, the projection of the angular momentum pseudo-vector onto the linear momentum vector, is invariant under translation and rotation transformations. But, a sufficient boost in the direction of propagation will switch direction of the linear momentum vector and change helicity. Since massless particles travel at the speed of light it is impossible to

change their helicity through a boost. This makes the helicity of massless particles the same as chirality, like the difference between a left and a right hand it is also invariant under boost transformations, but changes if the coordinate system parity is changed, like looking at hands in a mirror. Selecting a right-handed angular momentum as positive was thought to be an arbitrary convention. If all the descriptions changed to a left-handed convention, a change in parity of the coordinate system, it was assumed physics would be the same.

That physics is not symmetric with a change in parity was perhaps the biggest surprise from neutrino interactions. Experiments in the 1950s studying kaon decay observed kaons decaying into products with different parity, yet, no difference in the kaons could be found. This was referred to as the $\theta-\tau$ problem. In 1956 Lee and Yang [9] claimed that while experimental evidence supported parity conservation in strong and electromagnetic interactions, there was no evidence to support parity conservation in weak interactions. They proposed parity violation may explain the $\theta - \tau$ puzzle. In 1957 Wu et al. [10] performed an experiment observing beta decay of cobalt-60 in a magnetic field. The observed asymmetry of the decay was a clear indication of parity violation. The Goldhaber, Grodzins and Sunyar [11] experiment that followed shortly after established that neutrinos had left-handed helicity.

When parity violation was observed and neutrinos were established as left-handed, the previously dismissed — because it violated parity — massless two-component neutrino theory gained attention [12]. The neutrino field was separated into left-handed and right-handed fields, and it was assumed the neutrino field was only the left-handed field. The theory only works if neutrinos are massless, so helicity is the same as chirality, or neutrinos could change helicity through a boost.

Soon after the massless two-component theory, the universal V-A (vector, axial vector) theory for the weak interaction followed, extending the theory to all fermions in the weak interaction [13]. This dropped the massless assumption and attributed the parity violation to the interaction, instead of the neutrino itself, though the massless neutrino assumption remained as the standard model of particle physics developed.

The standard model includes unified theory for weak interactions and electromagnetic

interactions, the Glashow-Weinberg-Salam model [14, 15, 16]. In the GWS model the electroweak force is mediated by four bosons: the massless photon, the two massive charged $W^{\pm}$ bosons, and also a massive neutral Z^0 boson. The Gargamelle bubble chamber at CERN first observed the neutral current from the Z^0 boson in 1973 [17]. Parity violation in the neutral current was later observed at SLAC in 1978 [18] — which showed parity violation is due to the underlying interaction, not neutrinos themselves.

The possibility of massive neutrinos became important over the next couple decades. The Homestake experiment of Davis [19, 20] was the first to make a direct measurement of the solar neutrino flux in 1968, which used the inverse beta decay of chlorine-37 to produce argon-37 (equation 1.1). However, the observed neutrino flux was only around a third of that expected from the standard solar model. The calculations were checked with no errors found. Further experiments using radiochemical and Cherenkov detectors verified the Homestake result. This became known as the solar neutrino problem, and the eventual resolution proved neutrinos do have mass.

The next difference between neutrinos discovered was that neutrinos came in different flavors. In 1962 Danby et. al. [21] studied the generation of leptons using neutrinos from pion decay at Brookhaven National Laboratory. Pions almost always produced a muon, and very rarely an electron. Using a neutrino beam from pion decay, they observed that when these neutrinos that interacted with a nucleon they only generated muons, never electrons, and concluded the two flavors of neutrinos were distinct. The tau was discovered in 1975 by Perl [22], bringing the number of known neutrino flavors up to three. The distinctness of the neutrino flavors turned out to be another faulty assumption when neutrino flavor oscillation was later discovered.

Pontecorvo [23] had proposed in 1968 that if neutrinos had mass they could change flavor states. Flavor oscillation is enhanced when traveling through matter, as was shown by Wolfenstein [24] in 1977. Further work by Mikheyev and Smirnov [25] led to the predicted resonance enhancement of neutrino oscillations by what is now called the Mikheyev–Smirnov–Wolfenstein effect. This matter enhancement of neutrino oscillations was thought to be a

possible explanation of the solar neutrino problem.

Evidence for neutrino flavor oscillation came from underground Cherenkov detectors monitoring atmospheric neutrinos. The ratio of muon neutrinos to electron antineutrinos measured wasn't as expected. In 1998 The Super-Kamiokande Collaboration [26] published a paper detailing how the the observed neutrino flux and the zenith angle dependence were consistent with neutrino oscillation. In 2002 the Sudbury Neutrino Observatory Collaboration [27] confirmed neutrino oscillation and explained the solar neutrino problem. The SNO experiment measured not only the electron neutrino flux, but also the total neutrino flux by detecting the neutron generated by a neutral current interaction with deuterium, and found the ratio was consistent with neutrino oscillation.

$$\nu_x + {}^2_1 H \rightarrow {}^1_1 p + {}^1_0 n + \nu_x \tag{1.3}$$

Further experiments have confirmed neutrino oscillation and measured the oscillation parameters.

1.2 Neutrino Oscillation

Neutrino flavor oscillation relies not only on neutrinos having mass, but also that neutrino flavor states are a non-trivial mixture of different mass states. Thus a neutrino born in a particular flavor eigenstate is in a superposition of different mass eigenstate, and propagates as a mixture of waves that have different wavelengths. The flavor states and the mass states can be related by the Pontecorvo–Maki–Nakagawa–Sakata matrix, which is constructed from four fundamental constants: three mixing angles and a phase factor related to charge-parity violation. In addition there may be a diagonal matrix containing two additional CP violation phases if neutrinos are their own antiparticles, known as Majorana particles [28, p. 247]:

$$U = \begin{vmatrix} c_{12}c_{13} & s_{12}c_{13} & s_{13}e^{-i\delta} \\ -s_{12}c_{23} - c_{12}s_{23}s_{13}e^{i\delta} & c_{12}c_{23} - s_{12}s_{23}s_{13}e^{i\delta} & s_{23}c_{13} \\ s_{12}s_{23} - c_{12}s_{23}s_{13}e^{i\delta} & -c_{12}s_{23} - s_{12}c_{23}s_{13}e^{i\delta} & c_{23}c_{13} \end{vmatrix} \begin{vmatrix} 1 & 0 & 0 \\ 0 & e^{i\frac{\alpha_{21}}{2}} & 0 \\ 0 & 0 & e^{i\frac{\alpha_{31}}{2}} \end{vmatrix} \tag{1.4}$$

where $c_{\alpha\beta} = \cos\theta_{\alpha\beta}$ and $s_{\alpha\beta} = \sin\theta_{\alpha\beta}$.The mixing angles relate the neutrino oscillation amplitudes between flavor states.

The wavelength of the oscillation relates to the difference in mass squared. The propagation for a particular neutrino mass state is given by:

$$e^{-iE_j t/\hbar} \tag{1.5}$$

The overlap of two propagating mass states, with different masses and the same momentum, the oscillation difference comes from energy difference:

$$E_i - E_j \approx \frac{m_i^2 - m_j^2}{2E} c^4 \tag{1.6}$$

This leads to an oscillation length of [29, p. 392]:

$$L = \frac{2\pi\hbar E}{\Delta m_{ij}^2 c^3} \tag{1.7}$$

That neutrinos oscillate is mostly likely explained by neutrinos having mass, and the oscillation length allows determining the difference of masses squared. However, neutrino oscillation does not give any information on the neutrino mass scale. It also allows for two different orderings of the mass states, which is referred to as the neutrino mass hierarchy. Either the neutrino with the largest mass difference from the other two is the heaviest — similar to the mass hierarchy for charged leptons and quarks, which is called the normal hierarchy — or it is the lightest, which is called the inverted hierarchy.

The 2016 best fit values from the Particle Data Group [28] for neutrino mass differences:

Parameter	Best Fit ($\mathrm{eV}^2/\mathrm{c}^4$)
Δm_{21}^2	$7.37 \cdot 10^{-5}$
$\Delta m_{32}^2 \, (\Delta m_{31}^2)$	$2.50 \, (2.46) \cdot 10^{-3}$

The 2.50 value is for the normal hierarchy where $m_1 < m_2 < m_3$, which the 2.46 value is for the inverted hierarchy where $m_3 < m_1 < m_2$. The Δm_{21}^2 is for the neutrinos closest in

mass and is responsible for solar electron neutrino oscillation. The $|\Delta m^2_{32}|$ ($|\Delta m^2_{31}|$) term is the larger mass splitting for the normal (inverted) neutrino mass hierarchy, and is associated with atmospheric muon neutrino oscillation.

1.3 Neutrino to Antineutrino Conversion

Since neutrinos have mass, their helicity is dependent on the observation frame. All observed interactions are with left-handed neutrinos, but as a massive particle it cannot be traveling at the speed of light. So, a sufficient boost of reference frame in the direction of propagation will result in a flip in helicity.

As helicity is the only observed difference between neutrinos and antineutrinos, it is unknown whether the neutrino its own antiparticle, also called a Majorana particle after the man who demonstrated the possibility in 1937 [30]. If the parity violation in the charge current weak decay is due to a helicity preference, and not some underlying difference in the neutrinos, then it should be possible for some isotopes to undergo neutrinoless double beta decay — in which two virtual anti-electron neutrinos are emitted, but one converts to an electron neutrino and the pair annihilate. Thus nearly all the energy goes into the two electrons, with a negligible amount to the daughter nucleus.

The search for neutrinoless double beta decay is performed on nuclei where single beta decay is energetically forbidden, but double beta decay is allowed. Double beta decay with the emission of two neutrinos has been observed for many such isotopes. If neutrinoless double beta decay is possible, then there would be a bump at the end of the beta energy spectrum. If such a decay were observed it would show that the neutrino is a Majorana particle, and that lepton number is not conserved by the weak interaction. However, neutrinoless double beta decay would be very suppressed and efforts to observe such decays have so far placed lower limits on decay lifetimes.

Lower limits on neutrinoless double beta decay lifetimes do give an upper limit on neutrino mass, but only under the assumption the neutrino is a Majorana particle. It also is a limit on an effective neutrino mass for neutrinoless double beta decay, which relates to neutrino mass

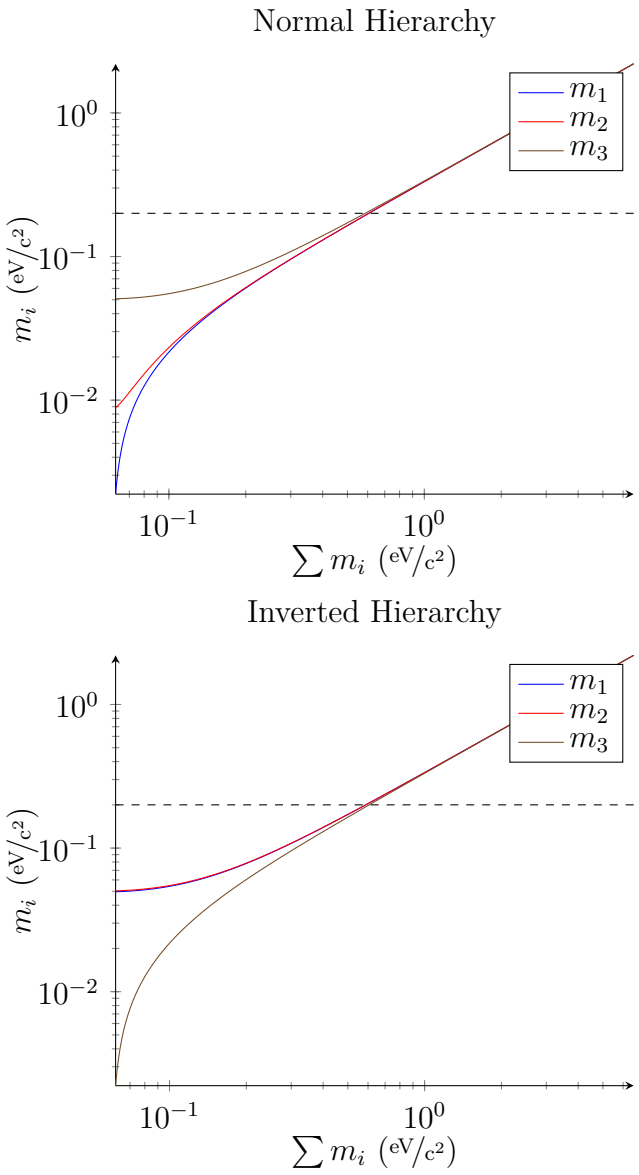

Figure 1.2: Normal and inverted neutrino mass hierarchy, shown up to the current direct mass measurement limit of $2.05\,\mathrm{eV/c^2}$. The dashed line is at the KATRIN design sensitivity of $0.2\,\mathrm{eV/c^2}$. For the inverted hierarchy the $7.37{\cdot}10^{-5}$ eV mass difference is difficult to see on a scale showing all three neutrino masses.

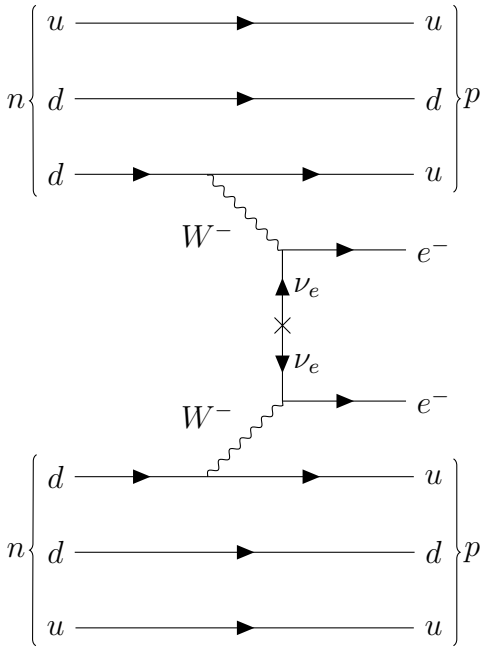

Figure 1.3: Neutrinoless double beta decay Feynman diagram

through two unknown phases (see equation 1.4). Observation of neutrinoless double beta decay wouldn't provide a direct neutrino mass measurement, instead, it would give a possible neutrino mass range — which, depending on the range, could determine the neutrino mass hierarchy [31].

1.4 Indirect Neutrino Mass Measurement

Another method of determining neutrino mass is from fits of observations to models for the evolution of the universe involving neutrino mass as a fit parameter. The commonly used basic model that reasonably explains observations is the ΛCDM model, which has a cosmological constant and cold dark matter. The ΛCDM model has six fit parameters, and neutrino mass is not one of them. The basic assumption is that the normal mass hierarchy is the correct one and the difference between the mass of the heaviest neutrino to the others is large compared to the mass of the lightest neutrino, which puts the sum of neutrino masses

at around 0.06 eV for the basic model. The basic model can be extended to include the sum of neutrino masses as a fit parameter, which gives an indirect method of determining neutrino mass [32].

Anisotropies in the cosmic microwave background are mainly influenced by relic neutrinos when they were still relativistic, so the effect of neutrino mass is small. However, they can still provide an indirect neutrino mass measurement. Large scale structure formation has a dependence on the neutrino free-streaming length, which goes through a mass-dependent minimum as the universe expands. However, the neutrino mass dependence resembles that of other parameters, so it must be used with a simultaneous fit to other data in order to lift the degeneracy in the fit parameters [33]. The Planck collaboration [34] observations of cosmic microwave background, along with large scale structure formation, fit a neutrino mass extension of the basic ΛCDM model, which gave an upper limit on the sum of neutrino masses of < 0.21 eV with 95% confidence.

While this suggests the neutrino mass is below the limit of the current generation of direct neutrino mass experiments, this neutrino mass determination depends on the validity of the ΛCDM model. Some ΛCDM fit parameters disagree with other measurements significantly. For example: the fit value for the Hubble constant of 67.8±0.9 km/s/Mpc disagrees with a direct measurement of the Hubble constant [35] of 73.8±2.4 km/s/Mpc by 2.3σ. This higher direct measurement value for the Hubble constant actually suggests an even lower value for neutrino mass than that found using a 6+1 ΛCDM fit to the Planck data. But, this tension also hints there are likely problems with the ΛCDM model, which gives further motivation for a direct measurement of neutrino mass as an important test.

1.5 Supernova Direct Neutrino Mass Measurement

As a massive particle, the speed of a neutrino is dependent on its mass and energy. Thus if a burst of neutrinos occurs in a short time span from a localized source, the spread in travel time will broaden as it travels due to energy difference, and the amount of broadening can be used to determine the neutrino mass. On February 23rd, 1987 a supernova was observed

in the Large Magellanic Cloud. Preceding the light from the supernova, a burst of neutrinos was observed in the Kamiokande II, IMB, and the Baksan neutrino detectors.

Bahcall and Glashow [36] used the difference in neutrino arrival time and energy in the Kamiokande II observations to determine neutrino mass. Some of the lower-energy events arrived before higher-energy events, which they used to establish a lower limit on the source pulse duration. From the observed energy and time spread they placed an upper limit on the broadening. They assumed that if some phenomenon compressed the neutrino burst in time during propagation, it wasn't by more than a factor of 2. With this assumption they used the observed spread in arrival time and the distance to the source to place an upper limit of 11 eV on neutrino mass — a limit more stringent than any direct mass measurement experiment at the time.

There are now more neutrino detectors with higher sensitivity. Another nearby supernova could give better results, though it would be unlikely to compete with the current generation of beta decay direct neutrino mass measurement experiments. The Jiangman Underground Neutrino Observatory may be able to set an upper limit around 1 eV, depending on the distance to and mass of the progenitor star [37].

1.6 Beta Decay Direct Neutrino Mass Measurement

When he developed his theory of beta decay Fermi [4] established the shape of the beta energy spectrum as a method of determining neutrino mass. Experiments measuring beta decay spectra had been performed before the neutrino was even postulated, allowing Fermi to give the first result for a direct neutrino mass measurement while he was developing his beta decay theory. This same method has been employed by many experiments since, and with one notable exception, later shown to be in error, only a reduced upper mass limit has resulted.

At the time Fermi developed his beta decay theory it wasn't known that there were different neutrino flavors or masses. The basic idea remains the same, but the distribution needs to be summed over the different neutrino flavors. The final state of the daughter

nucleus can be an excited state, which reduces the energy given to the neutrino and electron, thus a sum over final states is also required. The spectrum for an allowed decay such as tritium, or super allowed decay, from Bodine et al. [38]:

$$\frac{dN}{dE_e} = C\,F\left(Z, E_e\right)\frac{p_e E_e}{\epsilon^2}\left(1-\frac{E_e}{M}\right) \cdot \sum_i \left(\Delta_i - E_e\right)\left|U_{ei}^2\right|\sqrt{\left(\Delta_i - E_e\right)^2 - m_{\nu i}^2\epsilon^2}\,\Theta\left(E_{ei,max} - E_e\right) \tag{1.8}$$

$$C = \frac{G_F^2 m_e^5 \cos^2\Theta_C}{2\pi^3}\left|M_{nucl}^2\right| \tag{1.9}$$

$$\Delta_i = \frac{1}{2M}\left(M^2 - M_{(f)}^2 + m_e^2 + m_{\nu i}^2\right) \tag{1.10}$$

$$E_{ei,max} = \frac{1}{2M}\left(M^2 - M_{(f)}^2 + m_e^2 - m_{\nu i}^2 - 2m_{\nu i}M_{(f)}\right) \tag{1.11}$$

$$\epsilon = 1 - \frac{2m_e}{M} + \frac{m_e^2}{M^2} \tag{1.12}$$

Where: Z is the charge on the daughter nucleus, E_e is the electron energy, p_e is the electron momentum, G_F is the Fermi weak coupling constant, Θ_C is the Cabibbo angle, $m_{\nu i}$ is the neutrino mass, m_e is the electron mass, M_{nucl} is the nuclear portion of the transition matrix, U_{ei} is the neutrino mixing matrix element, and $E_{ei,max}$ is the maximum electron energy for a neutrino mass eigenstate. The initial state mass, M, and the final state mass, $M_{(f)}$, including excitation energy. The extrapolated endpoint energy, Δ_i, is the endpoint energy if neutrino mass is set to zero. The Heaviside function, $\Theta\left(E_{ei,max} - E_e\right)$, ensures the state is energetically accessible. The Fermi function, which accounts for the Coulomb attraction of the electron and the nucleus, is approximated by [39]:

$$F\left(Z, E_e\right) \approx \frac{2\pi\eta}{1 - e^{-2\pi\eta}} \tag{1.13}$$

where $\eta = {}^{\alpha Z}/_{\beta}$ is the Sommerfeld parameter where α is the fine-structure constant and β is the ratio of the electron speed to the speed of light.

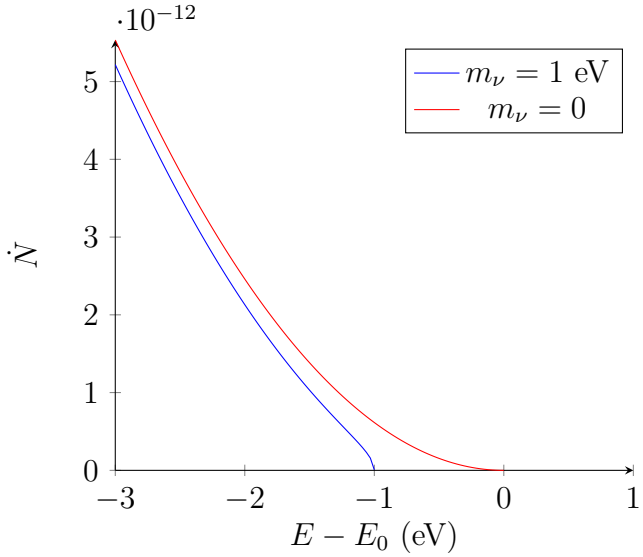

Figure 1.4: Tritium beta decay beta energy spectrum for massless neutrinos, and electron neutrino mass of 1 eV. Shown only for decay to the He-3 ground state.

The neutrino mass differences are small compared to the sensitivity of KATRIN, thus if KATRIN is able to measure the neutrino mass they will be quasi degenerate and the spectrum can be calculated assuming a single mass representing the mass of an electron neutrino. This won't be true for heavier sterile neutrinos, but the effect of such neutrinos would show up farther down the energy spectrum than the region of interest near the endpoint for light neutrino mass determination.

Chapter 2

KATRIN

2.1 KATRIN Overview

The KArlsruhe TRItium Neutrino experiment [40], or KATRIN, is the latest generation in MAC-E filter neutrino mass experiments that aims to measure the neutrino mass by measuring the beta energy spectrum from beta decay. It is designed to improve the direct neutrino mass measurement upper limit to $< 0.2\,{}^{\mathrm{eV}}/_{\mathrm{c}^2}$ at 90% confidence, or measure the mass if it is above $0.35\,{}^{\mathrm{eV}}/_{\mathrm{c}^2}$. KATRIN is currently scheduled to start taking tritium data in late 2017. The major components are shown in figure 2.1.

KATRIN will use a Windowless Gaseous Tritium Source (WGTS). The source will be continuously supplied with tritium gas in the middle of the 10 m source tube, which will be pumped out at both ends. Pressure will be maintained at $3.4 \cdot 10^{-3}$ mbar and temperature at 27 K. The design field strength in the source is 3.6 T and the source diameter is 90 mm. This will deliver $9.5 \cdot 10^{10}$ disintegrations per second.

Electrons from the source will be guided to the spectrometer section by the transport section. To achieve a low background from tritium decay in the spectrometer, it is necessary to reduce the tritium partial pressure to 10^{-20} mbar [40, p. 146]. This is accomplished by two pumping sections, each constructed with kinks in the beam tube so electrons are magnetically guided around the kinks while tritium will encounter pumping surfaces. The first pumping section is a differential pumping section using turbomolecular pumps, which will reduce tritium flow by more than a factor of 10^5. This is followed by a cryogenic pumping section, which will be maintained between 3 to 4.5 K and covered in argon frost to adsorb tritium. The cryogenic pumping section will reduce tritium flow by more than a factor of 10^7.

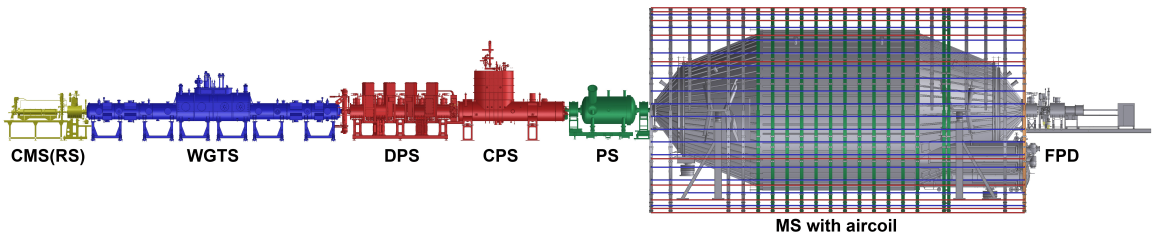

Figure 2.1: The KATRIN beam line. Rear Section (RS) in yellow, Windowless Gaseous Tritium source (WGTS) in blue, Differential Pumping Section (DPS) followed by Cryogenic Pumping Section (CPS) in red, Pre-spectrometer (PS) in green, Main Spectrometer (MS) followed by Focal-Plane Detector (FPD) in gray.

Following the transport section, KATRIN has two spectrometer sections both of which are MAC-E filters. The KATRIN pre-spectrometer comes directly after the transport section, and has a minimum magnetic field of 20 mT. Compared to the strongest design magnetic field in the beam line of 6 T, this gives an energy resolution of 62 eV (see equation 2.3), and will be used to reduce the electron flux entering the main spectrometer. The main spectrometer will have a minimum magnetic field of 300 μT, resulting in an energy resolution of 0.93 eV. For the source strength of $9.5 \cdot 10^{10}$ disintegrations per second and the angular acceptance of 51 degrees, a retarding potential 6.4 V below the decay endpoint would result in only one electron making it through the main spectrometer per second, neglecting tritium decay final states. The vast majority of electrons will end up being absorbed in the rear section. Those important few electrons near the endpoint, which carry the neutrino mass information, are counted by the detector.

2.2 MAC-E Filter

Making an accurate neutrino mass measurement requires a high energy resolution and high luminosity. Magnetic Adiabatic Collimation with an Electrostatic filter (MAC-E filter) is an idea first proposed by Beamson et al. [41] in 1980. Lobashev and Spivak [42] proposed

using such a filter to determine electron antineutrino rest mass by measuring the tritium beta decay beta energy spectrum in 1985. And Picard et al. [43] built one and tested it with krypton 83 in 1991. A MAC-E filter provides a high resolution and a high luminosity. As the name suggests, it collimates the electron beam using magnetic field prior to application of the electrostatic filter (see figure 2.2). The electrons are produced in a high magnetic field region, and guided down the beam line by a gradually changing magnetic field. The magnetic field changes slowly compared to the gyration of the electron, thus the total energy and the magnetic moment of the electron are constant [40, p. 35]:

$$(\gamma + 1)\,\frac{E_{\perp}}{B} = constant \tag{2.1}$$

where γ is the Lorentz factor, $E_{\perp}$ is the kinetic energy stored in the momentum perpendicular to the magnetic field, and B is the magnetic field. This puts a limit on the starting pitch angle in the source that electrons can have, and still make it through the maximum magnetic field.

$$\sin\theta_{max} = \sqrt{\frac{B_{source}}{B_{max}}} \tag{2.2}$$

Those electrons with a higher initial pitch angle will be reflected by the magnetic mirror effect. The electrostatic field is applied parallel to the magnetic field, so only electrons with a kinetic energy associated with momentum parallel to the magnetic field higher than the electrostatic retarding potential are transmitted. For this type of filter the energy resolution is the difference in minimum energy to pass the retarding potential of an electron at the maximum pitch angle compared to zero pitch angle. At the electrostatic filter γ can be assumed to be one, which gives an energy resolution equal to the maximum energy still associated with the momentum perpendicular to the magnetic field, for an electron at the maximum initial pitch angle:

$$\frac{\triangle E}{E} \approx \frac{\gamma + 1}{2}\frac{B_{min}}{B_{max}} \tag{2.3}$$

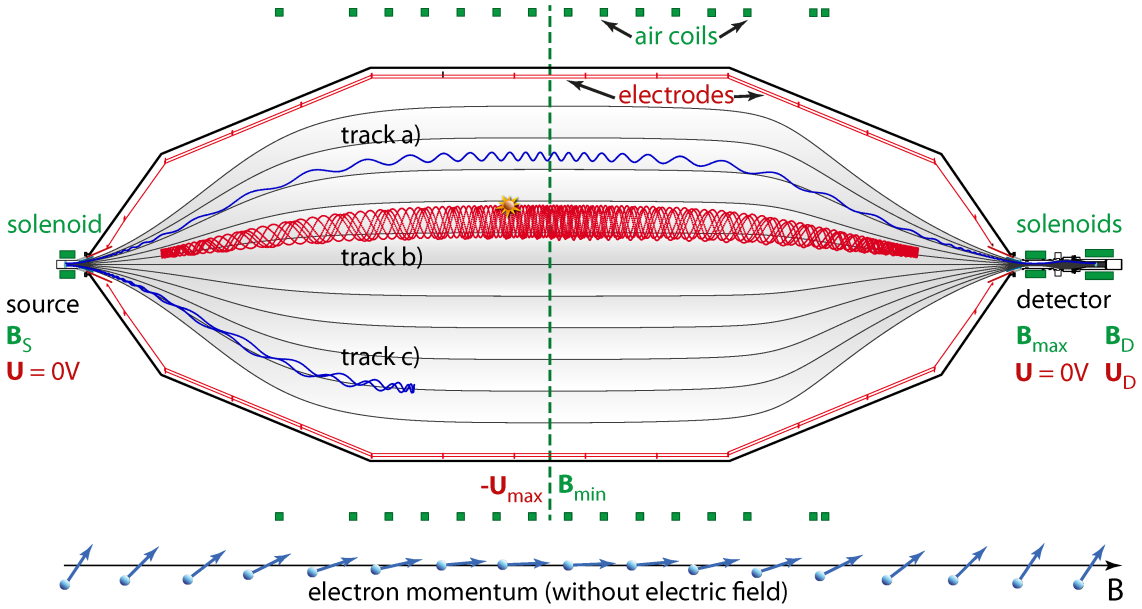

Figure 2.2: MAC-E filter principle. Track a is for an electron that passes the retarding potential, and track c is for a reflected electron. Track b is for an electron that scattered and was magnetically trapped. Reprinted from Arenz et al. [46].

This type of spectrometer was used by the Mainz experiment [44], and the Troitsk experiment [45], to attain the lowest limits on neutrino mass from direct measurement so far of $< 2.2\,^{eV}/_{c^2}$ and $< 2.05\,^{eV}/_{c^2}$ respectively at 95% confidence.

2.3 Detector

The detector section contains two vacuum chambers, each pumped by turbomolecular pumps and cryogenic pumps. When the magnets are operating, only the cryogenic pumps are used and the turbomolecular pumps are removed, as they cannot tolerate the high magnetic field. The ultra-high vacuum chamber is connected to the main spectrometer and houses the detector wafer. The high vacuum chamber houses the detector preamplifiers, and is isolated from the ultra-high vacuum chamber to prevent outgassing from the electronics from entering the ultra-high vacuum system.

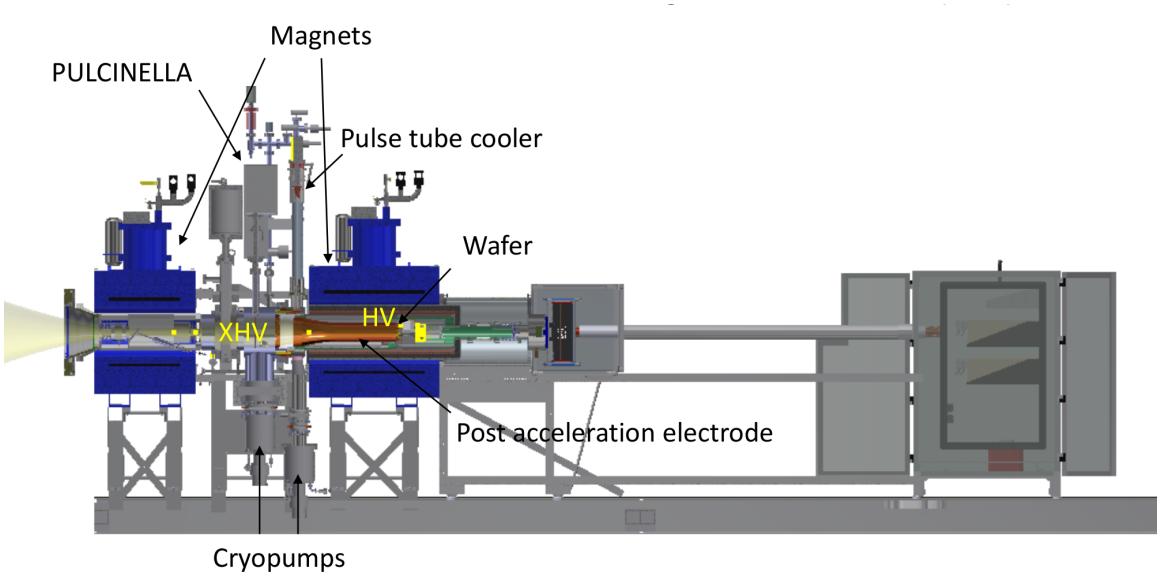

Figure 2.3: KATRIN detector section. XHV is the ultra high vacuum chamber, while HV is the high vacuum chamber.

Electrons from the main spectrometer are guided by the magnetic field of the 6 T pinch magnet, which is the highest magnetic field in the beam line, and the 3.6 T detector magnet to the detector wafer. The wafer and the electronics housed in the high vacuum chamber are cooled by a pulse tube cooler, which supplies cooling through the Post-Acceleration Electrode (PAE). The PAE is positively biased to accelerate the electrons to a higher energy, lower background, region of the detector. This requires the detector wafer and in-vacuum electronics to be elevated to the PAE voltage. The signal is optically isolated by using LEDs and fiber optic cables to send the signal to a data-acquisition crate at ground potential.

KATRIN uses a 503 μm-thick, 125 mm-diameter silicon wafer PIN diode for electron detection [47]. The front of the wafer is positively biased, which is applied by pins contacting the outer ring of the back of the wafer. A conductive titanium nitride (TiN) coating on the back of the wafer wraps around the edges of the wafer to connect the bias the front of the wafer. The front of the wafer is n++ doped to apply bias across the face of the wafer. The

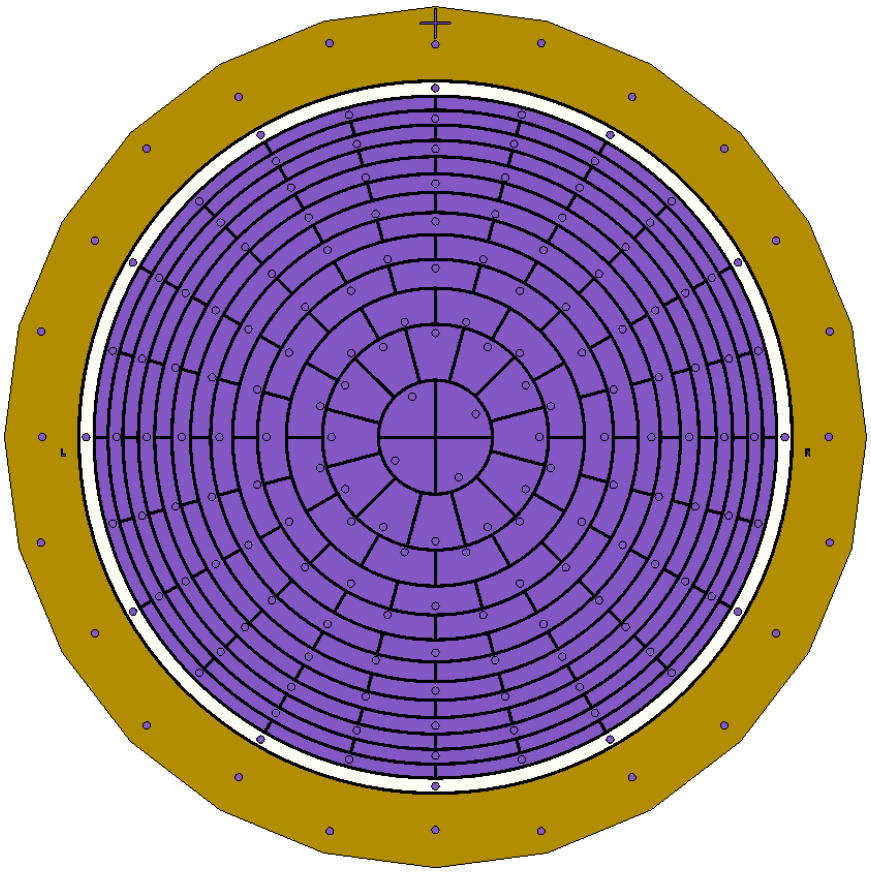

Figure 2.4: FPD wafer sectioning: bias ring is shown in gold, guard ring in silver, and pixels in violet. The small purple dots are where pins make contact. Wafer diameter is 114 mm.

rear of the wafer is segmented in a dartboard pattern into 148 pixels, each with 44.1 mm^2 area, that are read out separately.

The center dot is split into four quadrants, and around that are twelve rings of twelve pixels each. Between the bias ring and the outer ring of pixels is a guard ring, which ensures the pixels on the outer ring are surrounded by regions that are biased. A diagram of the wafer sectioning can be found in figure 2.4. Pogo pins (SS-30-J from Smiths Interconnect) connect each pixel directly to a charge-sensitive preamplifier in the high vacuum chamber through a vacuum feedthrough [48].

The signal from the preamplifiers is carried by coaxial cable to another vacuum feedthrough, which connects to optical sender boards outside the vacuum chamber. The optical sender boards have an adjustable gain, to adjust all the signals to similar amplitudes, and produce optical signals for high voltage isolation. The optical signal is read out by a data acquisition crate networked to a computer. This optical isolation is required to allow the detector electronics to ride on a high voltage, while the data acquisition crate is at ground.

2.3.1 Calibration

The detector system contains two calibration sources (shown in figure 2.5). One is a source tube in which radioactive gamma sources can be inserted with a thin wall at the end. The tube is normally withdrawn and rests entirely outside the flux tube, and it can be inserted into the chamber until the end of the tube is in the middle of the chamber. The gamma source is used to make frequent detector calibrations using an americium-241 source.

The second calibration source is photoelectrons from a UV-illuminated titanium disc. The disk is normally withdrawn to outside the flux tube, and can be inserted so it closely matches the design flux tube. The detector magnet can be altered so the disk either entirely obscures the detector, or is entirely contained within the active detector area. The disk is illuminated with a deep UV LED (UVTOP255 from Sensor Electronic Technology) resulting in electron production through the photoelectric effect. The disk is biased by an adjustable high voltage power supply, allowing generating electrons at any energy up to 20 kV — limited

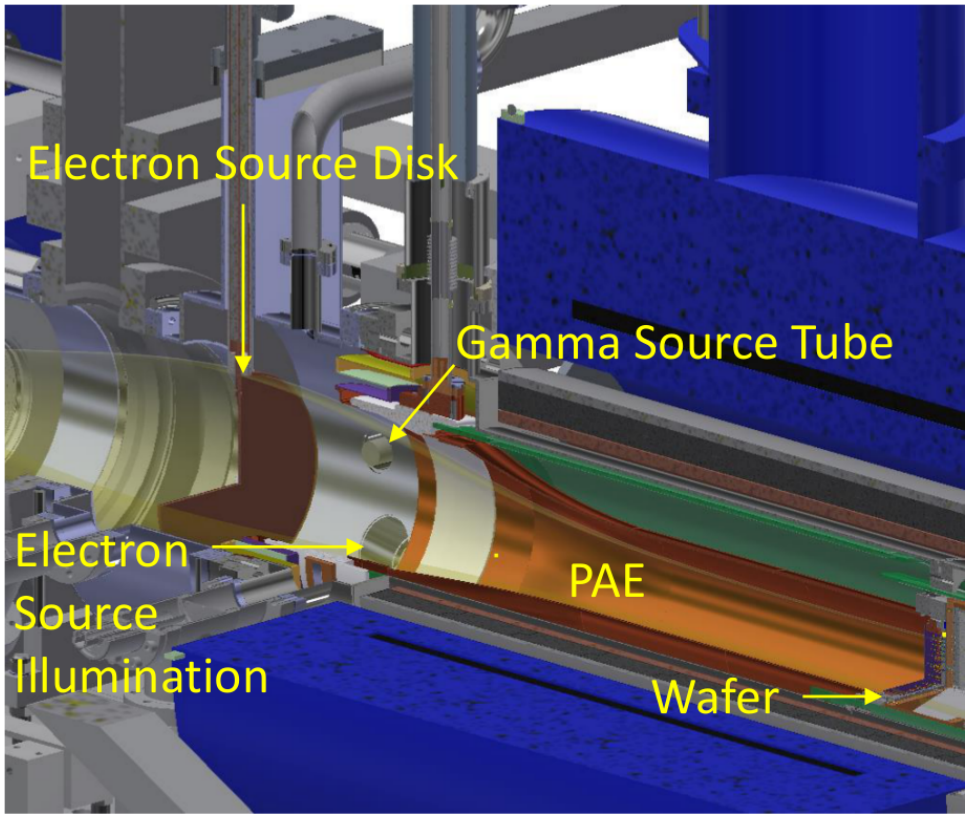

Figure 2.5: Detector calibration systems. PAE is post-acceleration electrode.

by the Kings 1764-1 and 1765-1 high voltage connectors from the bias power supply to the electron source current meter. Between the bias and the electron source is a current meter to measure the photoelectron current (see chapter 3.1) allowing for determining the absolute detection efficiency of the focal plane detector. The disk is also inserted and the current monitored prior to exposure of the wafer to the beamline, to ensure the wafer won't be damaged when exposed.

2.3.1.1 Electron Source Probe

The original electron source probe used a ceramic electric break, which was found to be slightly pizeoelectric and caused noise on the current meter that will be discussed in chapter 3.1.

A replacement probe was constructed that uses a glass electric break. The original disk was made of copper. The copper disk oxidized after a prolonged period of exposure to air and no longer produced photoelectrons when illuminated by the UVTOP 255. The copper disk was replaced with a titanium one, which still emits photoelectons even after prolonged exposure to air. Most of the length of tube supporting the disk is surrounded by a silica tube to prevent electron emission. The portion attaching to the disk that extends outside of the tube is coated in gold, so that the work function of the exposed support is above the energy of the photons from the UV LED. This ensures only the disk itself is emitting electrons. The source probe and meter boxes (shown in figure 2.7) consists of a triaxial electrode arrangement to shield the sensitive current meter from noise (effective circuit in figure 2.6).

- The outer box is grounded to the vacuum system.

- The outer tube of the probe is at the electron source bias voltage and connected to the inner box, but is isolated from the disk and meter by a filter.

- The inner rod is at the electron source bias voltage and electrically connected to the disk and electron source meter input.

- Between the outer tube and inner rod is an inner tube that is at electron source bias voltage, electrically connected to the meter box which is at the meter ground.

The parts are separated by Teflon spacers. The spacers at the top have o-rings to form a secondary vacuum boundary, limiting the amount of air that will enter the ultra-high vacuum chamber if the glass electric break fails. The inner seal of the spacer between the rod and inner tube has no o-ring and is made by the spacer body. On the top of the probe is a tension device to balance out atmospheric pressure when the system is under vacuum, to reduce load on the glass electric break. The tube of the tension device is non-conductive PVC to keep the disk electrically isolated from the support.

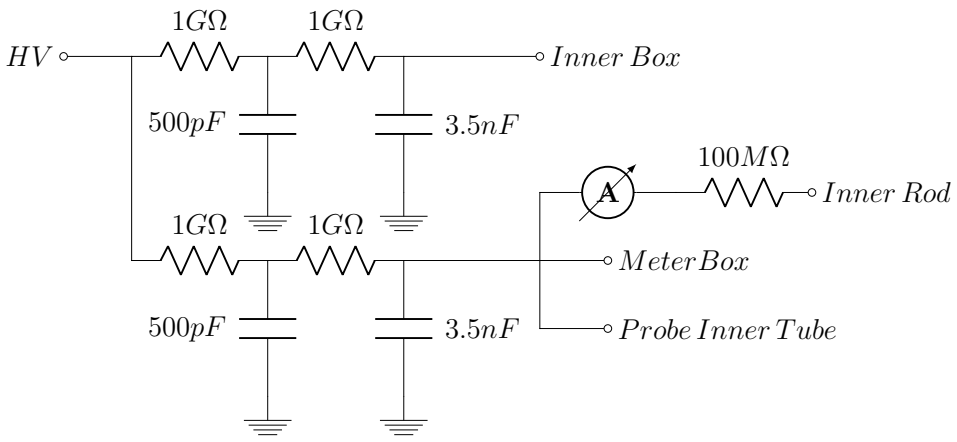

Figure 2.6: PULCINELLA bias filter electrical distribution.

2.3.1.2 Electron Source Illumination

UV illumination for the electron source disk comes in through a window located slightly downstream of the disk on the side of the vacuum chamber (see figure 2.9). This geometry results in an incidence angle of 77 degrees away from normal to the disk, measured from the center of the window to the center of the disk. The first illumination device, intended only for initial testing, was a UV LED placed on an adjustable plate attached to the view port. The angle of the plate was adjusted to point the UV LED at the disc, which resulted in a streak of high luminosity across the source with a much lower rate everywhere else. Greater uniformity was be attained by aiming the UV LED away from the disk and using scattered light. When the second illumination device was installed, which had lenses and prisms intended to provide a more uniform light distribution, the illumination still varied widely across the disc. Using the first device with a lens from the second to defocus the light provided a more uniform illumination profile.

A new device with sealed enclosure was developed, to provide a secondary vacuum boundary and limit the amount of air that would enter the vacuum chamber in the event the window fails (see figure 2.10). The third device has six individually adjustable UV LEDs. The UV

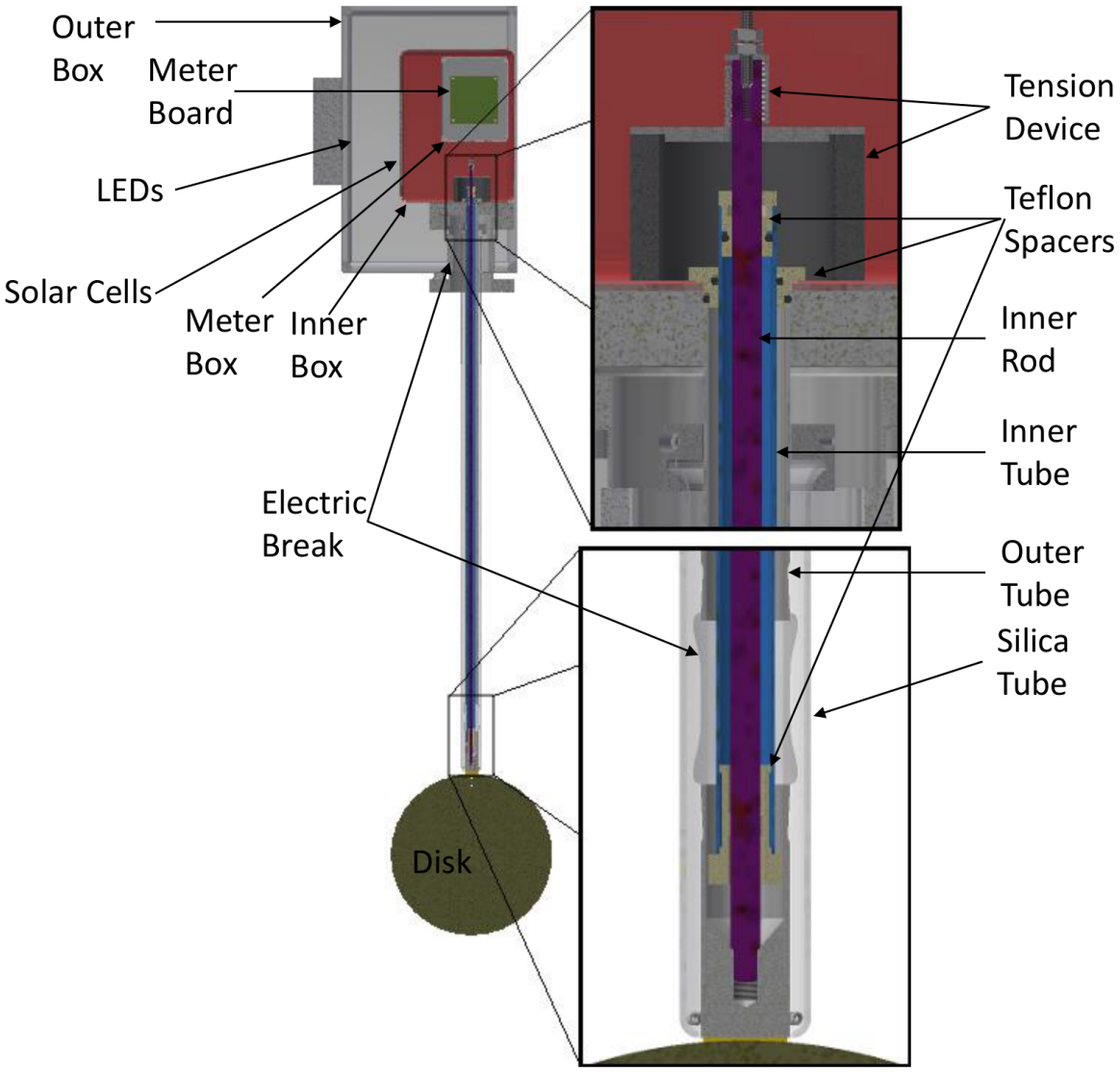

Figure 2.7: Electron source probe. The outer tube is in gray, the inner tube is in cyan, the center rod is in violet. The tan Teflon spacers include o-rings, shown in black, at the top to form a secondary vacuum boundary. The tension device tube is dark gray, the top plate is lighter gray. The meter board is green, which is housed in the gray meter box. The inner box is in red, and the outer box in gray.

LEDs are mounted in a cylinder with the axis of the UV LED rotated 15 degrees from the axis of the cylinder. This cylinder is housed in another cylinder, with the axis of the inner cylinder rotated 15 degrees from the axis of the outer cylinder. Rotating these two cylinders allows pointing the LED in any direction up to 30 degrees from the axis of the outer cylinder. The outer cylinder is housed in a pocket that is pointed 15 degrees from the axis of the illumination port, towards the disk. Each UV LED was driven by a voltage-to-current transducer with individually adjustable gains (see appendix B.1). A combination of UV LEDs combined at different intensities would provide a more uniform illumination. However, the illumination of a single UV LED with a lens to defocus the light was found to be sufficiently uniform (see figure 2.8).

2.3.1.3 Detector Linearity

In addition to the UV LEDs, the electron source illumination also contained a red LED. The design purpose was to pulse the red LED with short pulses of varying intensity, which would flood the FPD with roughly uniform illumination by reflecting light off the electron source disk. The combined energy deposited by the photons in a short pulse would appear as a single event to the FPD. Comparing the measured intensity from the optical feedback to energy measured for the events on the FPD would measure the linearity of the detector electronics. However, the light pulse had a measured rise time of $\sim$10 μs, making it unsuitable for a linearity measurement. Instead, the gamma source was used and the position of known peaks in the americium-241 spectrum were compared to the energy measured by the FPD, to establish the linearity as below 0.2% [49].

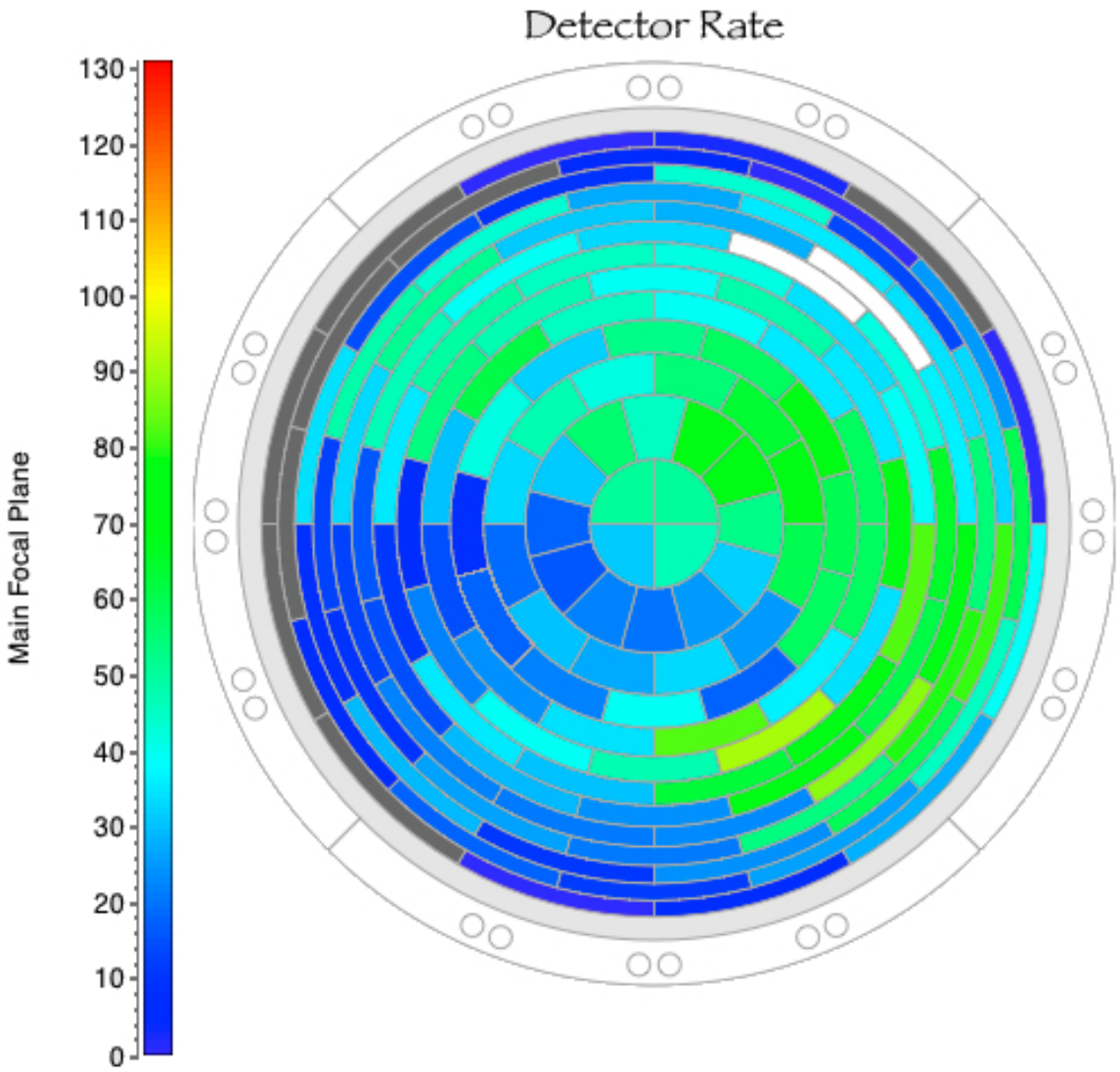

Figure 2.8: Electron source disk illumination profile

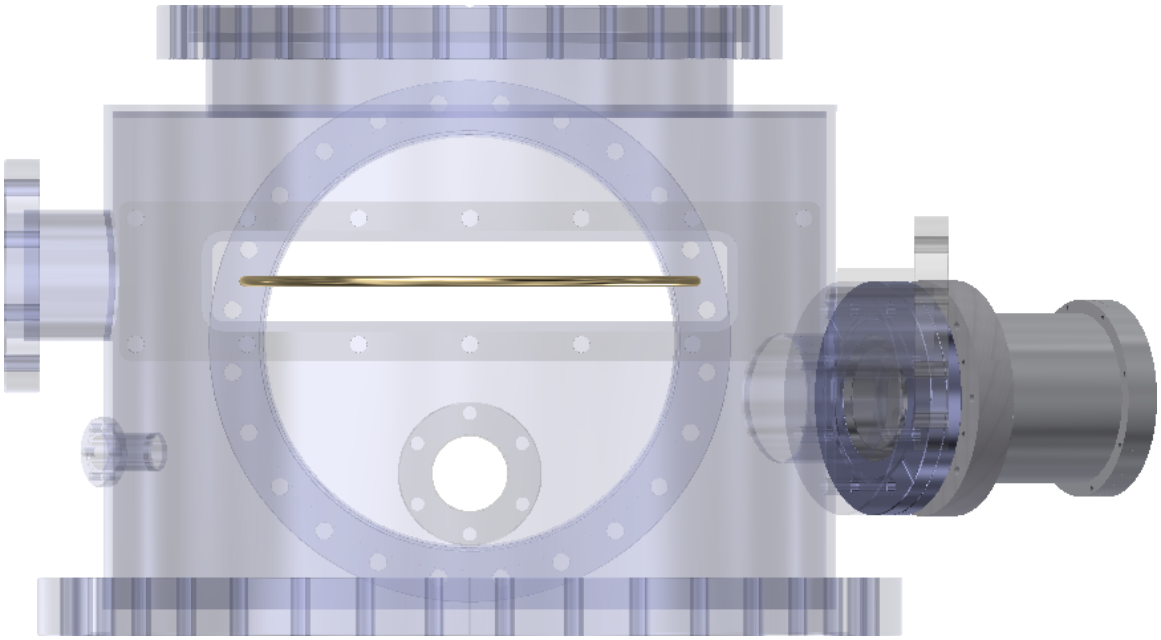

Figure 2.9: Orientation of illumination device mounted on view port with electron source disk, as seen looking from top of detector section ultra high vacuum chamber (shown semi transparent).

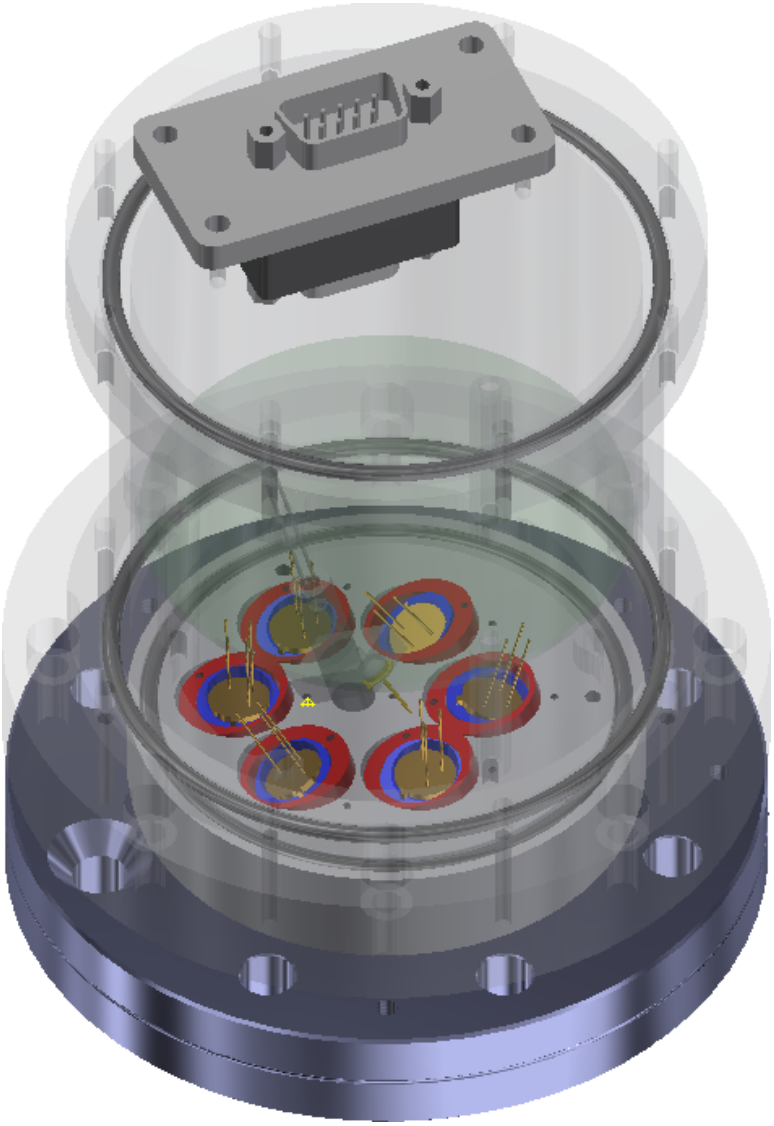

Figure 2.10: Electron source illumination device mounted on view port, with the: base, side, lid, PCB, and PCB standoffs semi-transparent. The UV LEDs are brass colored, the outer cylinders are in red, and the inner cylinders are in blue.

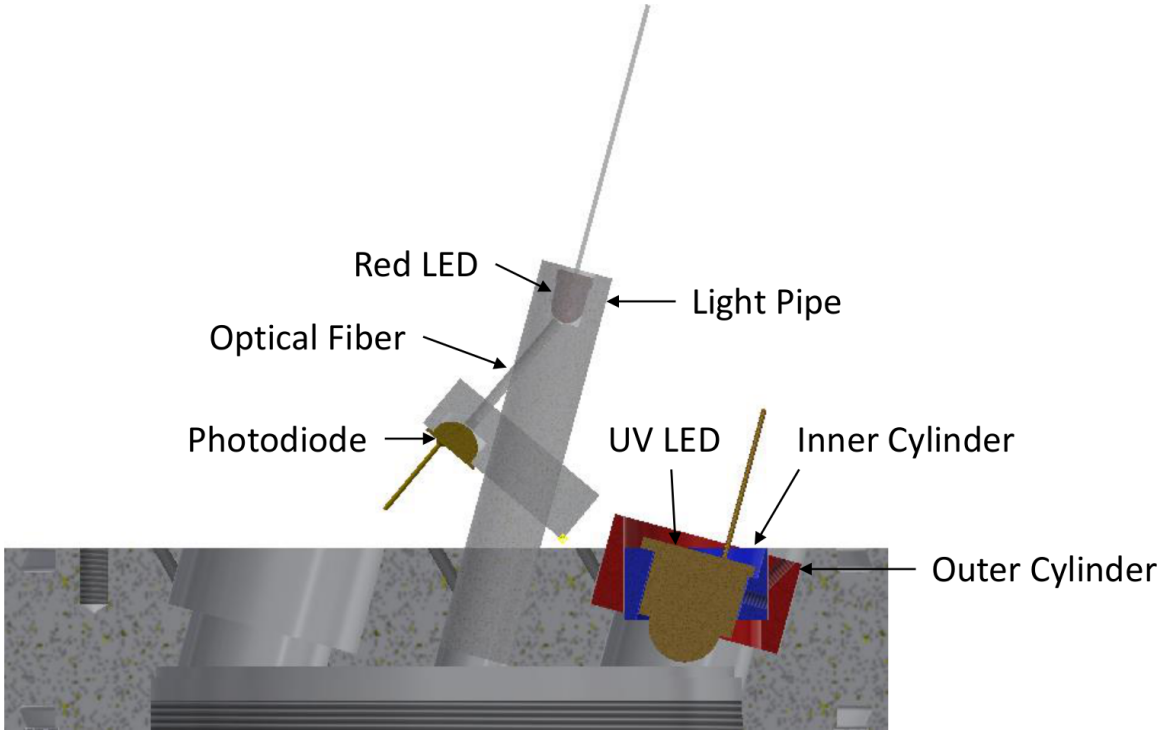

Figure 2.11: Cutaway view of a UV LED (brass colored) mounted in two nested cylinders (inner in blue and outer in red), in one of the six disk (gray) pockets in the electron source illumination device. To the left is the red LED (clear red) mounted in a light pipe along with the photodiode (brass colored) for the optical feedback. Threaded holes contain set screws to secure components in place. The optical fiber from the light pipe to the photodiode is also visible.

Chapter 3

ELECTRON SOURCE CURRENT METER (PULCINELLA)

3.1 PULCINELLA Overview

Between the electron source disk and the bias power supply is the Precision Ultra-Low Current Integrating Normalization Electrometer for Low-Level Analysis, or PULCINELLA [47]. PULCINELLA is a current meter that floats on the electron source bias voltage and measures the current on the electron source. Since the meter must float on a high voltage of up to 20 kV, its power and signal are optically isolated. Meter power is supplied by an array of LEDs illuminating an array of photovoltaic cells. The signal is sent from the meter through a fiber optic cable to a receiver board, which interfaces to a DAQ computer through an Ethernet connection.

The design purpose of PULCINELLA was to allow for determining the absolute detection efficiency of the focal-plane detector. However, the most frequent use has been to ensure no high currents or large discharges are present before exposing the detector to the main spectrometer. The electron source disk is inserted into the beam line, with the detector magnet field strength slightly higher than normal so the electron source disk completely obscures the detector, and used as a Faraday cup. If the current and discharges are within the range of PULCINELLA, then the detector will be safe from damage (see appendix A.1). When the meter is over-ranged it registers the maximum or minimum value.

PULCINELLA measured current using a DDC 114 Analog-to-Digital Converter (ADC) manufactured by Texas Instruments, which contains four pairs of charge-integrating ADCs. When one ADC in a pair is collecting charge, by discharging a 12 pF capacitor, the other is being read out and its capacitor recharged. This provides continuous current integration. Only one pair of ADCs is used, which is selected by jumper pins on the meter board.

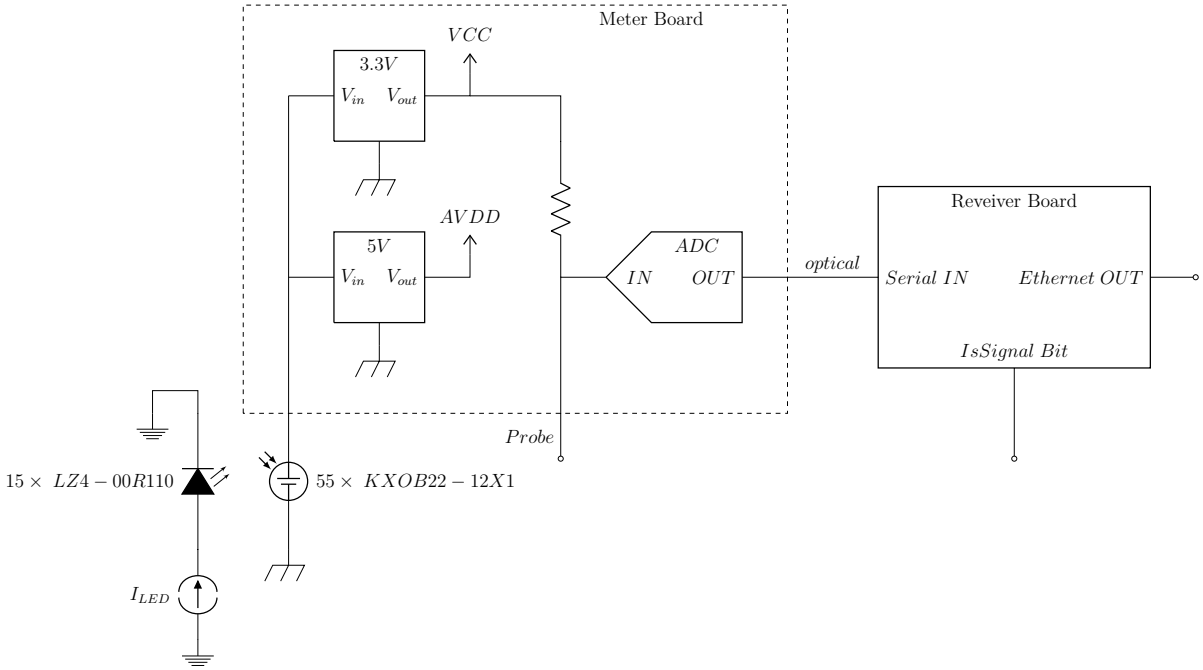

Figure 3.1: PULCINELLA block diagram

The integration time can be set to any multiple of 10 ms from 10 ms to 255 ms, also using jumper pins on the meter board. As the DDC 114 only had a small range for one polarity, an offset current was added to bring the zero-current reading to the middle of the ADC range. This zero adjustment was accomplished using a 3.3V regulator on the meter board and a large resistor. If the integration time is adjusted, the resistor producing the offset current needs to be exchanged to bring the zero-current reading back to the middle of the ADC range. The meter is very sensitive to even high resistance current paths around the meter, as the ADC input has an offset that can be as high as 2 mV.

The DDC 114 is controlled by an FPGA on the meter board. The FPGA adds to the 20-bit current measurements: an 8-bit event counter, a bit for which integrator in the pair made the measurement, and 2 bits specifying which pair of integrators were used. The FPGA drive an LED to communicate this information to a receiver board through a fiber optic cable. The communication is only one way, with the meter board sending and the receiver board

receiving. The receiver board adds one more bit from an input pin, intended to mark whether or not the UV LED in the electron source illumination system is on, bringing the total up to 32 bits. A WIZNet WIZ110SR Ethernet module on the receiver board connects the meter to a DAQ system. The DAQ used was a MAC running Object-oriented Real-time Control and Acquisition (ORCA) developed by the University of North Carolina, which is the DAQ system used by the KATRIN FPD and includes an object to insert the meter readings into FPD data runs.

PULCINELLA was initially tested as a standalone device. The current through a known resistance from a known voltage was measured and the meter attained an accuracy of better than 1 fA in one second of measurement time.

Despite the excellent performance as a standalone current meter, when PULCINELLA was installed on the electron source probe in a small test system the current meter was being over ranged by noise. The problem turned out to be the ceramic electric break used on the probe, which was slightly piezoelectric. This caused current fluctuations through the meter due to mechanical vibrations, mostly induced by the vacuum pump. This was visible on an oscilloscope attached to the probe as a voltage spike when the center rod was moved. When the probe was replaced by one using a glass electric break, the noise problems from the electric break went away, verifying that the ceramic electric break was indeed the noise source.

When the probe with meter was installed in the detector system and brought up to voltage, a new noise problem was introduced. The capacitance between the probe and the grounded vacuum chamber is about 17 pC. While the electron source disk gets closer to one side of the chamber, at the same time it gets further from the other side, resulting in a capacitance change that is a second-order effect. This small change in capacitance results in significant noise (see figure 3.4). The noise is proportional to the voltage on the probe, and the amplitude of oscillations. Oscillation amplitude depends on which vacuum pumps are running as well as the pulse tube cooler used to cool the detector electronics. With the probe biased at 18.6 kV, the amplitude of the noise is hundreds of times larger than the current the

detector system can handle (16 fA). Even with significant filtering, days-long measurement times are required to make FPD detection efficiency measurements.

3.1.1 LED Degradation

Power to PULCINELLA is provided by an array of LZ4-40R110 high power LEDs from LED Engin. These were initially used with a solar panel from a solar battery charger. The performance was checked after installation and the power to the meter board was more than sufficient. However, the meter would cease functioning properly some time after. If the meter lacks sufficient power it still functions, but the readings will be erroneously low. Before the addition of the zero adjusting offset current, the meter would tend to get stuck in the ADC zero current bin, providing a clear indication of improper function. With the adjustment to shift the zero to the middle of the ADC range, this indication of insufficient power was masked.

A sample of new LEDs was used to illuminate a new solar panel loaded by a spare meter board, with a used photodiode as an independent measure of light intensity. The LEDs were driven at 500 mA and 8.5 V, their specified limit was 1.2 A at 100 C. The temperature of the heat sink was usually around 60 C and never went above 64 C. The junction-to-case thermal resistance was specified to be 1.1 $^{\mathrm{C}}$/w, putting the junction temperature at a maximum of 68 C. The contact with the heat sink was made using Wakefield-Vette thermal silicon grease and produced a negligible temperature difference.

The light intensity was observed to drop to 39% of initial intensity over a weekend, and to 38% of initial intensity after another week. A new panel made from an array of KXOB22-12X1 photovoltaic cells was constructed and the performance of the new panel with the same LEDs was monitored for two months of continuous operation. After the initial burn-in period, a fit to the second month of data gives a decay time of 1,018 days. The new panel will provide sufficient power to the meter board even if the illumination drops to 10% of the initial value. As the LED array only needs to be powered when PULCINELLA is in use, which is infrequent, the new panel should provide sufficient power to PULCINELLA

for the life of the experiment.

3.2 Detector Absolute Calibration

The absolute detection efficiency of the focal-plane detector is measured by comparing the current measured by PULCINELLA to the event rate recorded on the focal-plane detector. The desired detection efficiency is for a fully working detector, thus issues that resulted in some pixels not functioning are corrected for. As the rate from photoelectrons is far above the background, all events above the detector threshold are recorded. A region-of-interest cut on tritium data results in the detection efficiency being slightly lower.

The rate for bad pixels is approximated as an average of the rate of neighboring good pixels. Events with more energy than should be deposited by a single electron are counted as double-occupancy events. The rate of higher-occupancy events is negligible and higher-occupancy events are counted as double occupancy.

Since the detection efficiency of high-energy electrons is of interest, the electron source probe requires a high bias for this measurement — the electron source disk was biased to -7.6 kV and the PAE to +11.0 kV. In order to ensure all electrons from the front of the electron source disk struck the FPD wafer, the detector magnetic field was raised to 4.68 T with the pinch magnet at 6 T. The electron source illumination was modulated on and off with a period of 60 seconds for noise filtering (see section 3.2.2). The electron source current and FPD hit rate were measured for 40 hours. The measured raw detection efficiency was 92.9%. This raw rate was adjusted by $3.79 \pm 0.43\%$ for emission from the back of the disk (see section 3.2.1) and 1.5% to account for crosstalk, to obtain a measured absolute detection efficiency of $95.1 \pm 1.8_{stat} \pm 1.5_{syst}\%$. In addition to the inaccuracy of the current from the back of the disk, the resistance and voltage used to calibrate the meter were each known to 1%, giving the combined systematic uncertainty. The statistical uncertainty was entirely from the current measurement. The efficiency is less than 100% because of events falling below threshold due to dead layer losses [49].

3.2.1 Correction for Emission from the Back of the Electron Source Disk

The stainless steel walls of the detector vacuum chamber don't reflect UV light well, but they do reflect enough to cause measurable photoelectron emissions from the back of the electron source disk. This results in some electron emissions that were not magnetically guided to the detector wafer that needed to be accounted for.

The magnetic field ratio of the detector magnet to the pinch magnet was run slightly higher than nominal, to ensure the entire disk was imaged on the wafer. The electron source was set to -1 kV bias, and the PAE was set to -2 kV. This caused all electrons emitted from the front of the disk to be reflected back to the disk so only emissions from the back were measured by PULCINELLA. The post acceleration voltage was then reduced to 0 V to measure the total emissions from the disk. The electron source illumination was set to a higher than typical intensity, as the rate on the focal-plane detector wasn't being used for this measurement there was no need to stay within its range. The electron source illumination was pulsed with a 60 s period to make photocurrent measurements at each PAE voltage setting.

The UV illumination was unstable, resulting in a measurement that wasn't a simple step function between the back-of-disk emissions and all emissions. As the form of this instability was unknown, the measured current was fit to a step function and a combination of sin and cosine functions, as well as a step function and polynomials. A fit for up to 40 sin and 40 cosine functions was used, and a fit for up to an 80th-degree polynomial. Examples are shown in figure 3.2. The data set included 443 data points for back-of-disk emissions only, and 443 for total emissions.

The mean for the polynomial fit was 3.80% for back-of-disk current, with a standard deviation of 0.35% for the set of fits. The sine and cosine fits gave a mean of 3.78% with a standard deviation of 0.37%. If the data points were treated as just a step function, ignoring any other behavior, and the spread in the points and number of points were the only uncertainty, the 1σ uncertainty should have been 0.24%. The functional form of the

current fluctuation was unknown, so the deviation of the result from the different function fits (see figure 3.3) was used as the function approximation uncertainty. The expected statistical uncertainty was combined with the function approximation uncertainty and the fraction of emissions from the back of the disk was determined to be $3.79 \pm 0.43\%$.

3.2.2 Filtering

The extremely large current fluctuations on the electron source are mostly around 7 Hz and 7.5 Hz. The estimated oscillation frequency of the probe was 6.2 Hz and 6.5 Hz. There are two modes with near the same frequency because the disk contributes two different moments of inertia, one for oscillations in the plane of the disk the other for the plane perpendicular to the face of the disk. The tension device wasn't included, which may explain why the noise spectrum shows a higher frequency than estimated.

The meter is only capable of sampling at a maximum rate of 100 Hz. To modulate the signal far away from the noise, the UV LED was modulated at a frequency of one cycle per minute. The modulation of the current was a square wave, but it was more effective to apply a sine wave filter to extract the current signal, as the square wave had significant harmonics that would extend up to the high noise band. This filtering scheme improved the measurement accuracy from 5 pA to 400 fA, normalized to one second measurement time, for -7.6 kV bias on the electron source and +11.0 kV on the PAE.

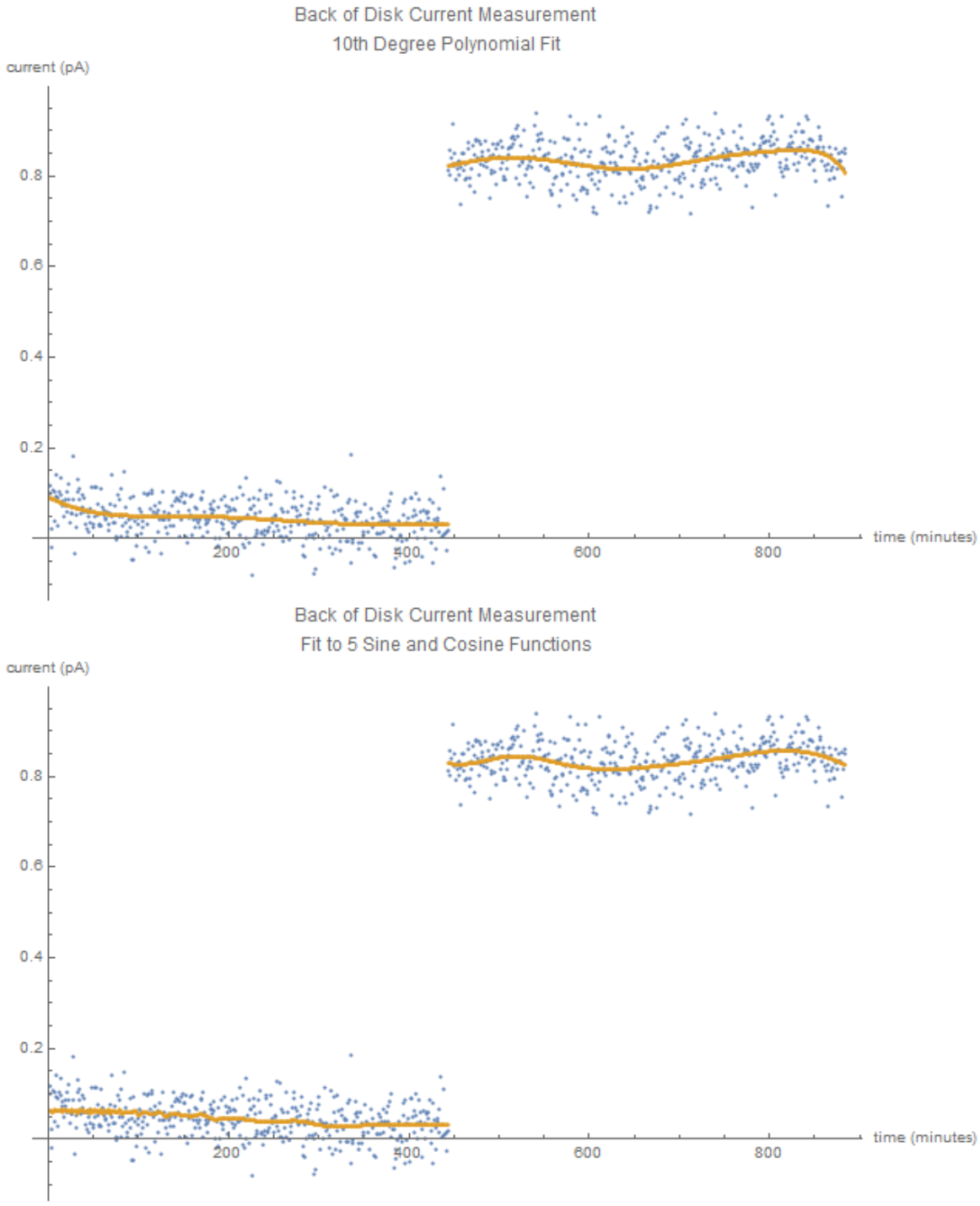

Figure 3.2: Sample function fits for determining electron emission from the back of the electron source disk.

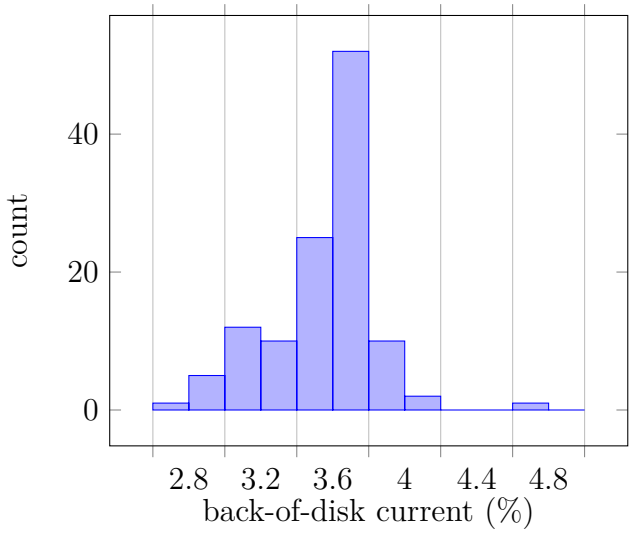

Figure 3.3: Back-of-disk current function fit values, 81 polynomial fits and 41 trig function fits.

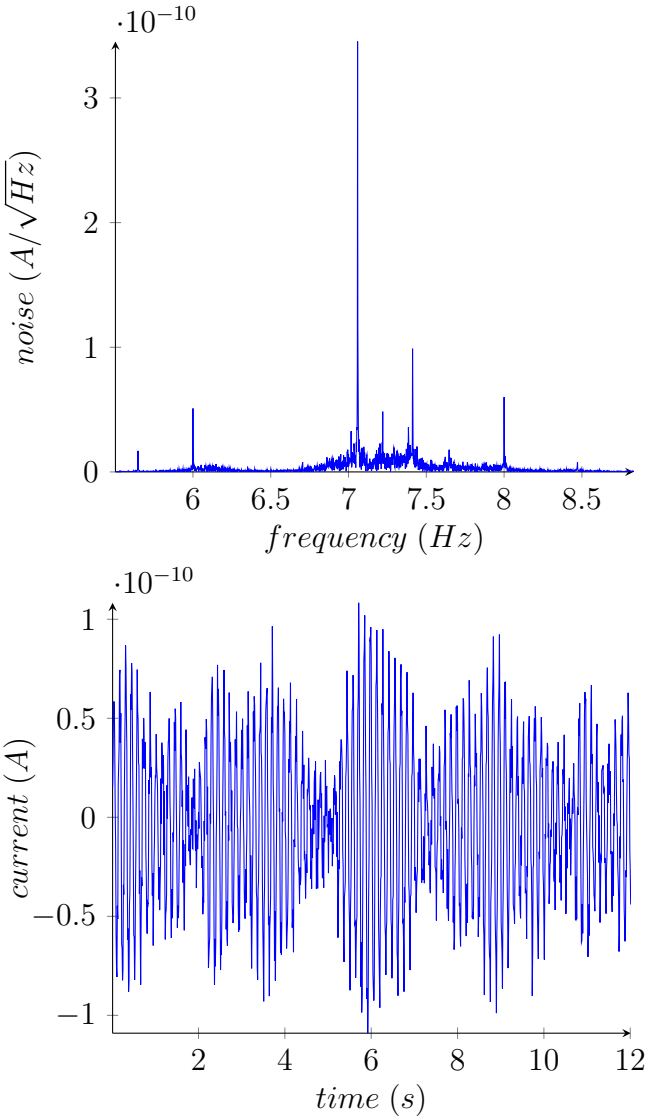

Figure 3.4: Current noise measured by PULCINELLA, for 20 kV bias, with cryopumps and pulse tube cooler on, at KIT.

Chapter 4

WAFER TESTING

4.1 Wafer Overview

The FPD wafer is mounted on the feedthrough flange (see figure 4.1), and electrical connections to the back of the wafer are made by 184 pogo pins: 148 pins for pixels, 12 for the guard ring, and 24 for bias. The wafer is mounted by resting it on the pogo pins with the flange laying flat. A Kapton insulator is placed between the wafer and the flange, as second Kapton insulator in placed on top of the wafer between the wafer and the copper ring. The copper ring is slipped snugly onto a holder, and then slowly pressed down until the wafer rests on the flange mating surface, compressing the pogo pins. Swivel hooks are rotated into position to secure the wafer in place, holes in the copper-ring holder are positioned above the swivel hooks to allow easier access.

After assembly, the electrical connection of each of the 184 pins needs to be checked. This was previously done by hand, carefully performing a check between each pixel pin and a bias pin to ensure it acted like a diode. Faults were frequently found, requiring the wafer to be remounted.

The time and effort involved in this process was significantly reduced by the construction of an automated wafer-testing device. Additionally, the resistance between pixels was not checked by hand and shorts had occurred due to a manufacturing defect as well as bent pogo pins. Many pogo pins made contact close to the edge of a pixel, and a small misalignment could cause two pins to connect to the same pixel. The automatic wafer tester detected these shorts as well. It also eliminated the risk of bending pins from making the connections to the pins by hand.

The FPD wafer tester was designed to test a wafer already mounted on a feedthrough

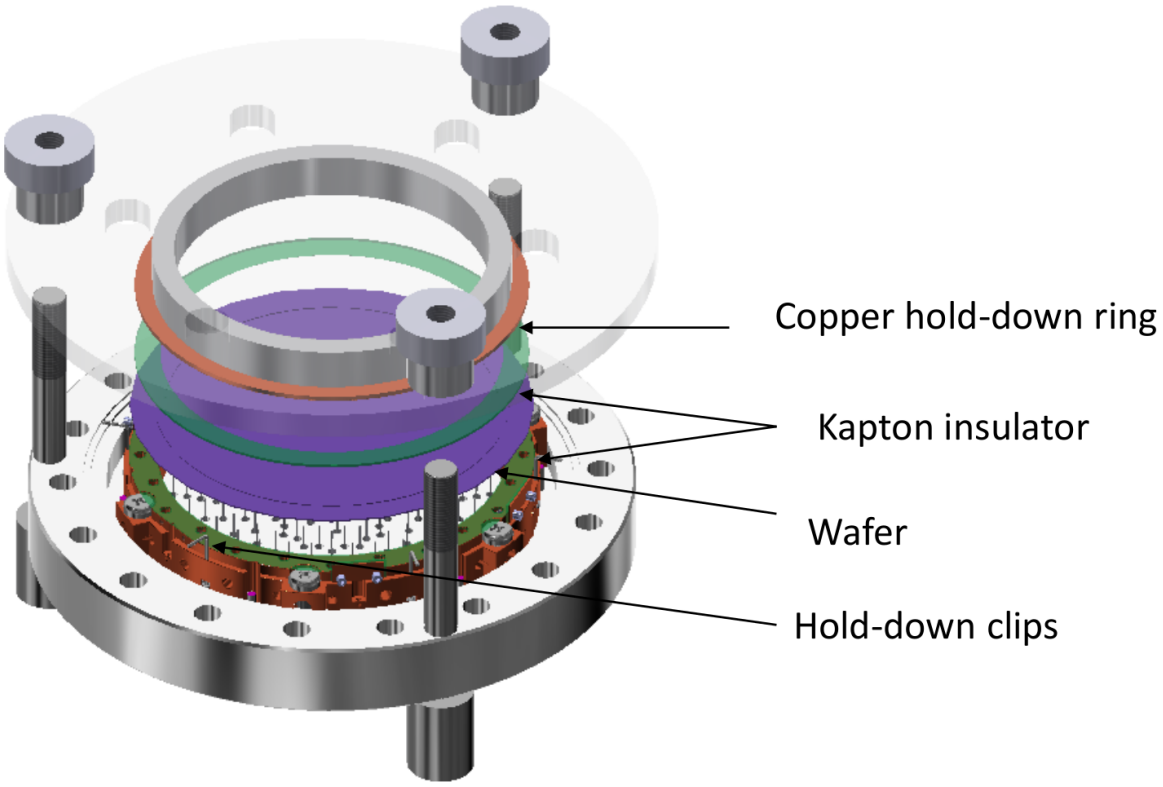

Figure 4.1: Wafer mounting assembly. The top most plate is made of aluminum, it is shown as transparent so the copper ring is visible.

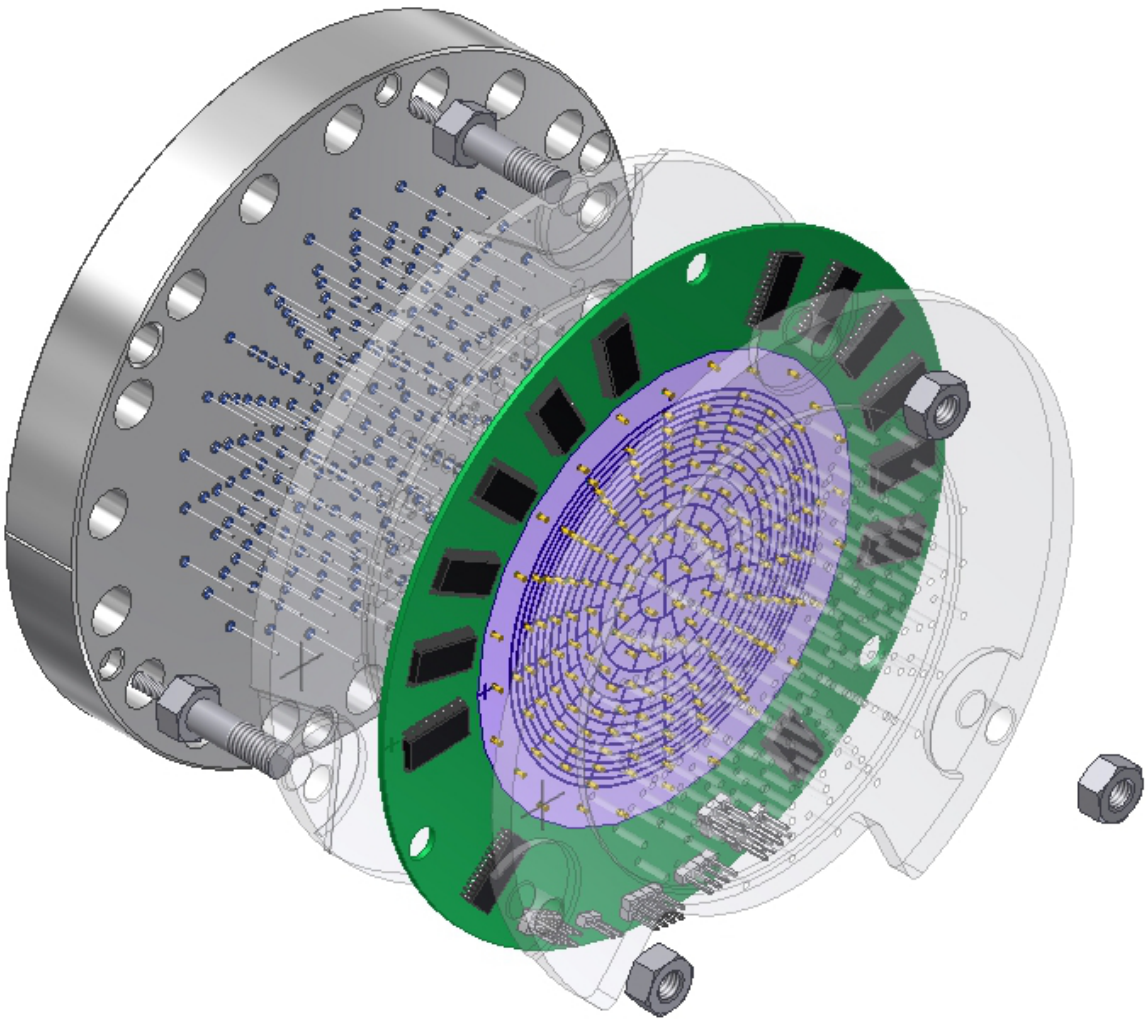

Figure 4.2: FPD wafer tester assembly drawing. The assembly is rotated such that the alignment marks are on the left.

flange. This is done by connecting the FPD wafer test board to the pins on the readout-electronics side of the feedthrough flange (see figure 4.2). The FPD wafer tester board consists of four sections: the standoffs, the pin alignment section, the PCB, and the top section.

The standoffs are three cylinders that attached to the feedthrough flange. Holes in the other sections accept the standoffs to ensure they are aligned with the pins during assembly. A thicker hexagonal portion spaces the pin alignment section from the high vacuum side of the feedthrough flange, and can be turned with a wrench to fasten the standoffs to the flange.

The pin alignment section is mounted with three holes that slide over the standoffs, and 184 holes that slide over the feedthrough flange pins. On the flange side of the holes, cone-shaped openings accept pins that are misaligned by as much as 2 mm and align them with the sockets in the PCB section. A cross-shaped alignment mark near the edge of the pin alignment section aligns with a notch in the side of the flange.

The PCB section has three holes that fit over the standoffs, and 184 sockets which connect to the pins on the feedthrough flange. A cross-shaped alignment mark near the edge of the PCB, as well as a second mark near the edge of the bias ring section of the wafer mock-up on the PCB, align with the notch on the flange.

The top section has three holes to slide over the standoffs, and 184 holes for the feedthrough pins and PCB sockets. A cross-shaped alignment mark near the edge of the top section aligns with the notch in the flange.

To attach the wafer tester to the flange, the flange is laid wafer-side down in a flange holder and the standoffs are installed. Then the pin alignment section, PCB section, and top section are loosely installed so they just rest on the pins, but the pins haven't yet pressed into the sockets. The nuts above the top section are installed and tightened until they meet resistance. The nuts are then tightened a little each time while rotating through the nuts to evenly insert the pins into the sockets.

When testing is complete the FPD wafer tester is removed by first removing the nuts,

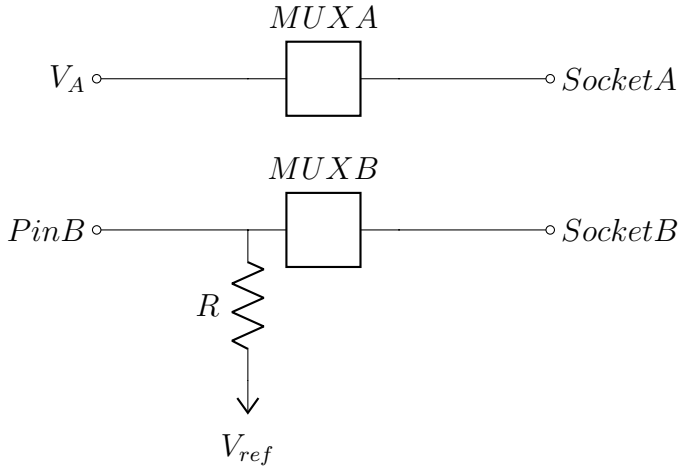

Figure 4.3: FPD wafer tester measurement circuit.

then evenly pushing the PCB section off the feedthrough flange pins by rotating through the standoffs and raising each a little each time.

The sockets make electrical connection to the feedthrough flange pins, and large pads around the sockets allowing easy testing of the FPD wafer connections. The pads are labeled for easy socket identification and form a mock-up of the FPD wafer. The bias ring and guard ring are further divided to allow one pad for each socket. On the FPD wafer, the bias ring and guard ring each make one continuous electrically connected zone. Aside from the segmentation of the bias ring and guard ring the pads mimic the FPD wafer.

The sockets are connected to test pins through multiplexers, allowing connecting to any socket automatically by changing the multiplexer address. 16 channel multiplexers are used, requiring 12 multiplexers to connect to the 184 sockets, and a 13th multiplexer to select which of the multiplexers connected to the sockets is enabled. The remaining 8 multiplexer pins are connected to test points on the PCB that were used for testing and calibration.

Two sets of multiplexers, referred to as A and B, are used to allow two connections to each socket. Each set of socket connection multiplexers is addressed by eight address pins. Multiplexer set A applies a known test voltage (V_A) to one socket (Socket A). Multiplexer

set B applies a known voltage (V_{ref}) through a known resistance (R) to another socket ($SocketB$) and connects the socket to the controlled ADC for measuring voltage ($PinB$). From this information, the resistance and voltage between any two pins can be measured.

The resistance from multiplexer set B and the reference voltage for pin B is determined by another multiplexer to allow changing the current through the pins.

The wafer tester is controlled by an Arduino microcontroller board. It connects to a computer through a USB connection, which provides communication and power for the wafer tester.

The controller was programmed to perform the following tests:

- Test bias ring connections are shorted. It also establishes a good bias connection to use for other tests.
- Test guard ring connections are shorted. It also establishes a good guard ring connection for other tests.
- Check for shorts between adjacent pixels, as well as the outer ring of pixels to the guard ring and the guard ring to the bias ring.
- Forward bias diode check from pixel to bias ring.
- Reverse bias diode check from bias ring to pixel.

As the FPD wafer is a photodiode, it is necessary to minimize background light. Turning off room lighting and covering it with a black cloth was usually sufficient. Problems due to light would usually affect the outer pixels the most, making it easily identifiable.

4.1.0.1 FPD Wafer Tester Results

Prior to installing a wafer for the second commissioning stage of the KATRIN spectrometer and detection sections, the FPD wafer tester was used to test all new wafers as well as the wafer from the previous commissioning stage for manufacturing defects. A known short between adjacent pixels was detected on the wafer used during the previous commissioning stage. It was a wafer from the second batch and the short was due to a defect in one of the masks used during manufacturing. An unexpected short between adjacent pixels in a wafer

from the third batch was also detected, which was was verified by testing the wafer directly with a multimeter and visual inspection under a microscope. No further shorts were detected on the remaining four wafers from the third batch. A wafer was selected and mounted, and a new short was detected. This short was caused by a pogo pin misalignment, causing the pin to contact two adjacent pixels. The pin was straightened and the wafer retested, twice as the fault remained after the first adjustment, then left installed on the flange for use during the KATRIN commissioning stage — with 100% working pixels for the first time.

4.2 KATRIN Focal-Plane Detector Performance Degradation

The detector wafer is a single silicon wafer pin diode segmented into 148 pixels. It is 503 μm thick and segmented in a dartboard pattern with 13 rings of pixels of 44.1 mm^2 area and 12 pixels in each ring, except for the center which has four pixels. The outer ring of pixels are surrounded by a 2 mm-wide guard ring held at the same potential as the pixels (see figure 2.4). Outside the guard ring extending to the edge of the wafer is the bias ring, which has a titanium nitride (TiN) coating that wraps around the edges of the wafer to apply bias to the face of the wafer. The intrinsic material is lightly n-doped silicon, the pixels and guard ring readout side are p-doped, and the entrance face is heavily n++ doped and used to apply bias to the pixels. On the readout side, the pixels, guard ring, and bias ring are all TiN coated to conduct across the wafer surface and connect to the pogo pins. TiN was chosen because it is non-oxidizing [48].

When a wafer from the third batch of KATRIN focal-plane detector silicon wafers was installed, replacing a wafer from the second batch, the detector noise was noticed to have increased from 1.5 keV FWHM to 2 keV FWHM. This adversely affected the detector system as it determines the width of the acceptance window required by the detector, and a wider acceptance window results in increased background rate.

The noise had a radial dependence, with the higher noise being found towards the perimeter of the detector. It was suspected this might be due to the radial dependence on pixel shape (see figure 4.5). From a distributed capacitance and interpixel resistance model of the

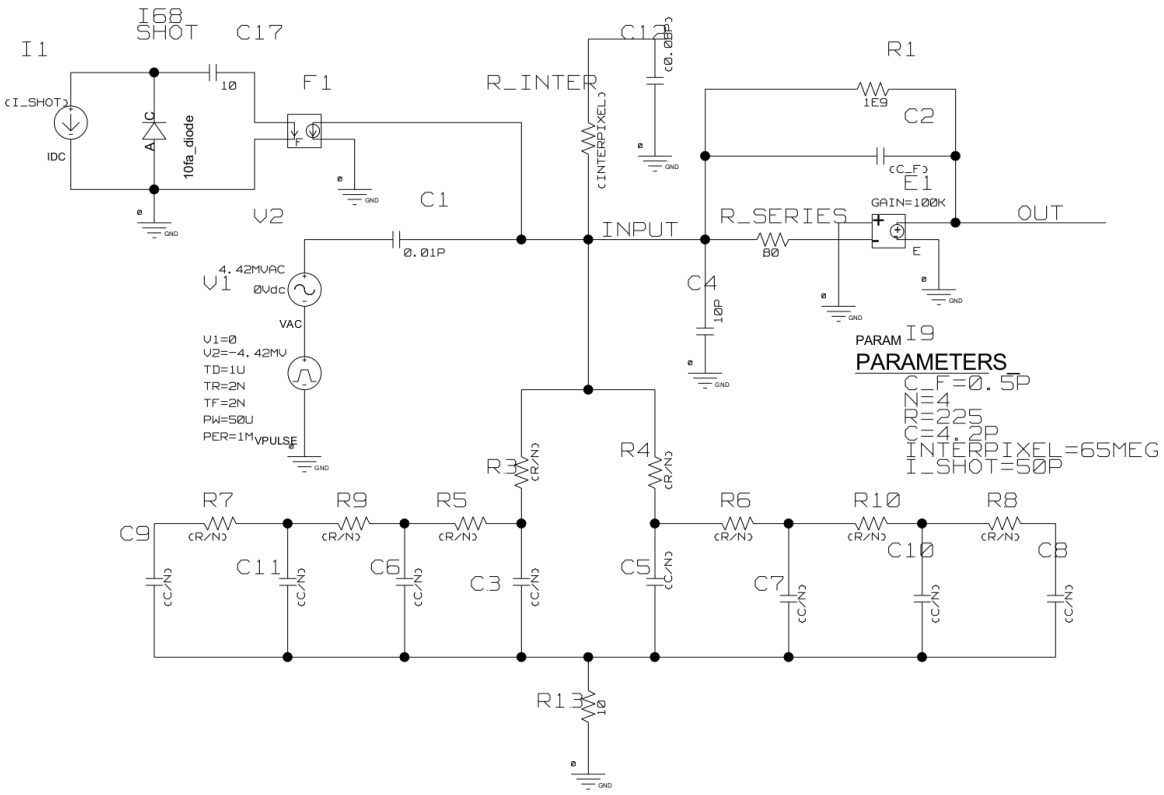

Figure 4.4: FPD wafer circuit model for two pixels, modeled as a distributed capacitance and resistance to simulate the pixel readout conducting across the TiN coating to the readout pin.

FPD wafer (see figure 4.4), it was determined if the sheet resistance of the readout side of the pixels were over 100 $\Omega/\square$, or the interpixel resistance were under 1 GΩ, it could explain the noise and radial dependence. A wafer from the third batch was compared to a wafer from the second batch to check if a possible source of the increased noise could be determined.

4.2.1 Interpixel Resistance

The outer pixels have a larger perimeter, so it is expected they would have lower resistance between pixels. This could result in the radial dependence observed in the noise. From the model of the detector wafer it was determined that an interpixel resistance under 1 GΩ

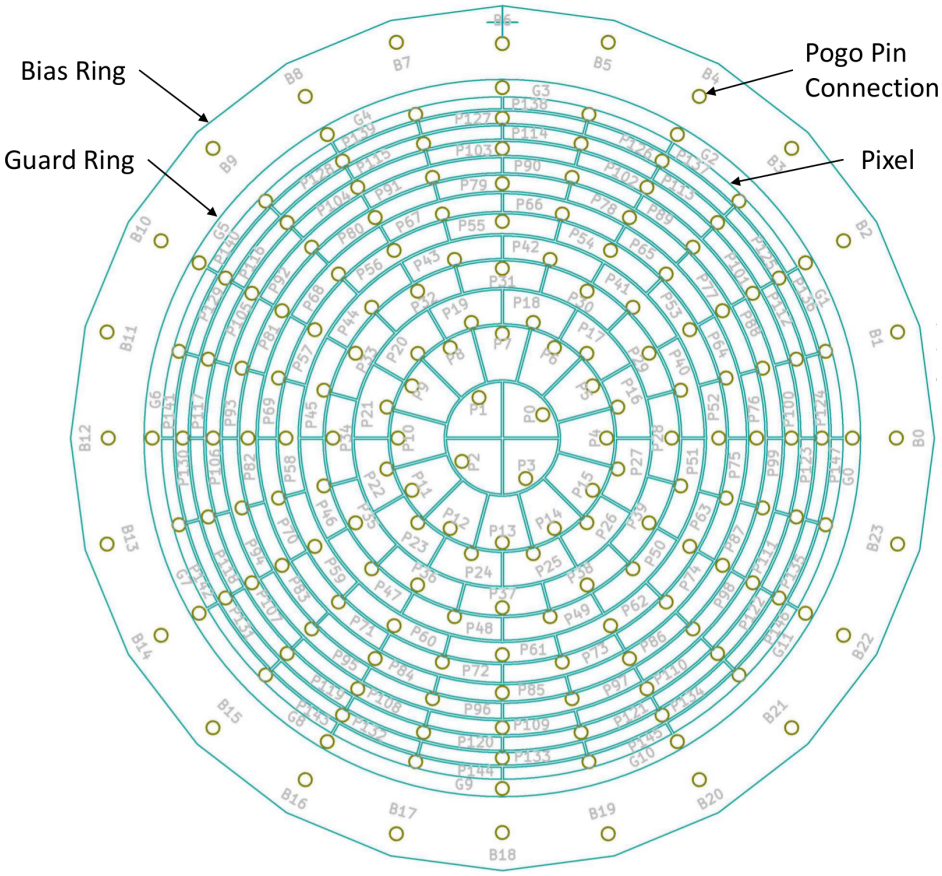

Figure 4.5: FPD wafer pin layout. The pins with labels starting with a P are pixels, with a B are on the bias ring, and with a G are on the guard ring.

could result in sufficient noise to explain the current noise in the detector. The interpixel resistance of a wafer from the third batch was measured and the resistance between pixels was >100 GΩ, thus eliminating interpixel resistance as a possible explanation for the increased noise.

4.2.1.1 Setup

To make electrical connections to test a wafer, the wafer was mounted on a feedthrough flange and a circuit board was connected to the pins on the feedthrough flange. The mounting of

the test board was identical to that previously used to mount the automated wafer tester (see section 4.1).

The test board contains 24 eight-pin connectors. Each connector has one or two connections to the common on the test board, and connects to all the pixel readout pins in a line from the center to the outside of the wafer, except for the center pixels. As the pixels are staggered between rows all the pixels with connections in such a line are not adjacent to each other, except for the center four pixels. As the center pixels' readout pins are in line with an adjacent pixel, the center pixels were shifted to the next group clockwise around the detector. This layout is shown in figure 4.6.

To test a pixel, a connector is attached to one of the 24 connectors on the test board, allowing for connection to six pixels (seven if it includes a center pixel), and four connectors with all the pins shorted together are attached to the adjacent and next adjacent connectors (as well as the other three center pixels if a center pixel is included). This ensures that all the pixels adjacent to the one being tested are shorted to the test board common. The guard ring is also connected to the test board common. The measurement is then made between the pixel under test and all surrounding pixels, and the guard ring, so the resistance measured is that of the entire pixel perimeter.

The current between pixels was measured by a picoammeter connected in series with 0-30 V power supply, allowing measurement of the current to voltage curve between pixels (see figure 4.7). A 0-200 V power supply applied a fixed bias the test pixel and the bias ring. An external 100 GΩ resistor was placed between the test pixel connection and the test board common to verify proper operation of the test circuit.

The flange with mounted wafer and test circuit were placed in a small refrigerator, to allow cooling the wafer and act as a dark box. A small hole was drilled in the side of the refrigerator to allow a nitrogen purge to prevent condensation. Light leaking into the refrigerator resulted in a few tenths of a pA difference between the room lights being on or off, and the setup had to be covered in dark cloth. Temperature was monitored by a Resistance Temperature Detector (RTD) attached to the feedthrough flange.

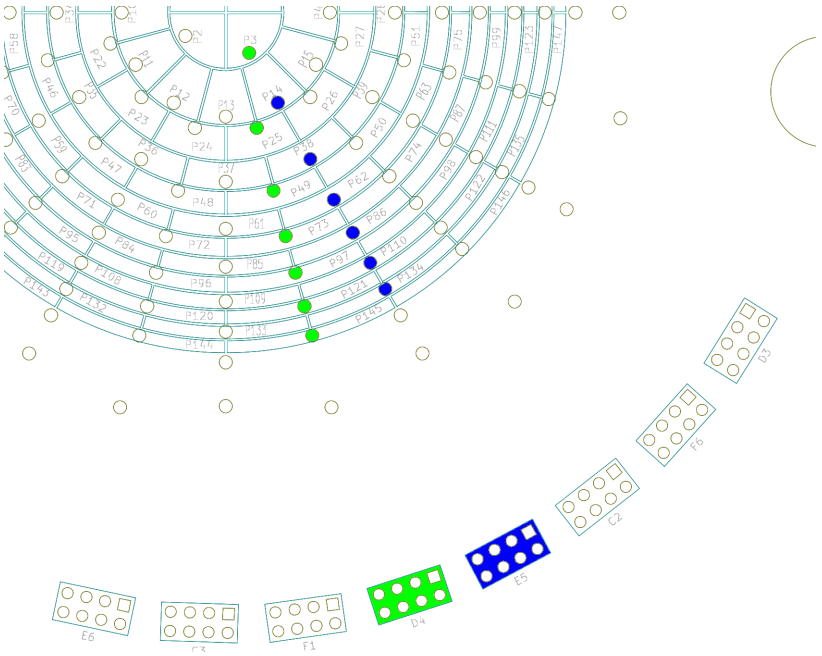

Figure 4.6: FPD wafer interpixel resistance test board. Pins in a line radially from the center of the wafer connect to the same preamplifier when installed in detector system. Except for the center pixels, pins in a line were grouped together in a connector allowing them to be shorted to ground in a group. This would group the center pixels with an adjacent pixel, preventing testing the resistance between center pixels and adjacent pixels. To prevent this, the center pixels were shifted one group clockwise around the wafer, from the blue group to the green group for the example.

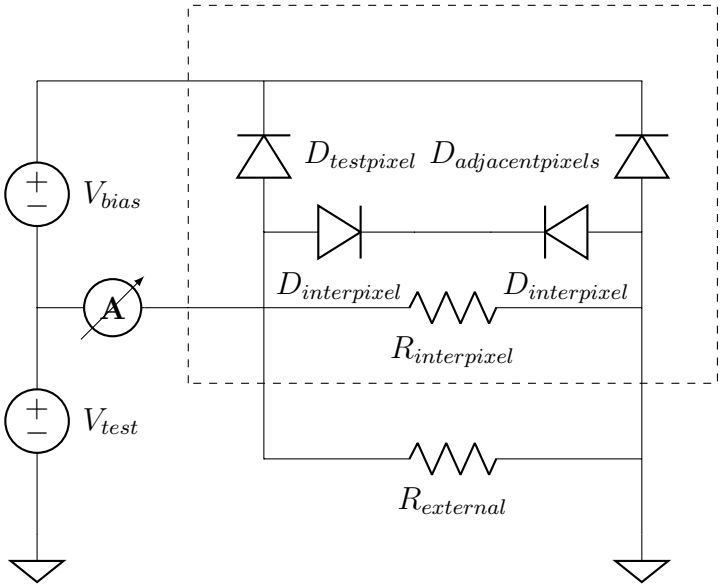

Figure 4.7: FPD wafer interpixel resistance measurement circuit. The section in the dashed lines is an equivalent circuit for the FPD wafer pixel under test and adjacent pixels.

The bias between the test pixel and the bias ring was held fixed, so that the leakage current of the test pixel was constant, and the voltage between the test pixel and adjacent pixels was adjusted while measuring the current. The measured current consisted of three contributions: the constant leakage current, the interpixel diode junction current, which was modeled using the Shockley diode equation, and an ohmic component representing the interpixel resistance and the 100 GΩ resistor if installed. The leakage current for the adjacent pixels would flow through the low impedance test voltage, but will not through the high impedance interpixel junction to the picoammeter.

Starting with the Shockley diode equation [50, 51, p. 94] and solving for the voltage on the diode:

$$I = I_s(e^{V_d/(nV_T)} - 1) \tag{4.1}$$

$$V_d(I) = nV_T \log\left(\frac{I_S + I}{I_S}\right) \tag{4.2}$$

and then solve the voltage across two back-to-back diodes for the current:

$$V = V_1 + V_2 = V_{d(1)}(I) - V_{d(2)}(-I) \tag{4.3}$$

$$I = I_s \tanh\left(\frac{V}{2nV_T}\right) \tag{4.4}$$

Adding in the leakage current and the ohmic shunt current, the measured current is described by the equation:

$$I = I_L + I_s \tanh\left(\frac{V}{2nV_T}\right) + V/R \tag{4.5}$$

Where V is the applied voltage between the test pixel and its neighbors, I_L is the pixel leakage current, R is the interpixel resistance which may include the 100 GΩ resistor in parallel if installed, I_S is the saturation current for the interpixel diode junction, and n is an ideality factor correction which was expected to fall between 1 and 2 [51, p. 98]. $V_T = \frac{e}{k_B T}$ is the thermal voltage where e is electron charge, k_B is the Boltzmann constant, and T is temperature. V_T should be around 26 mV at 300 K.

The measured current vs. applied voltage was fit to find R. If the 100 GΩ resistor was installed, the resistance in parallel with 100 GΩ necessary to result in the measured resistance was calculated.

4.2.1.2 Results

Only wafer 115876 was ever tested as the resistance measured was far above that which would explain the increase in noise, so no further testing was warranted. Wafer 115876 is a previously damaged wafer from the the third batch of wafers, the same batch that was installed when the increase in noise was noticed. It had been chipped on one edge, removing a section deep enough to penetrate the bias ring and halfway into the guard ring, but not

far enough to reach any pixels (see figure 4.8). It is unlikely a damaged wafer will ever be installed in the detector, which made it a good candidate for testing.

Pixel 121 was initially tested at different bias voltages without using an external shunt resistor (see figure 4.5 for pin layout). However, when three data sets came back with resistance all over 100 GΩ the setup was shifted to pixel 145, an outer ring pixel which should have the lowest interpixel resistance. A 100 GΩ resistor was added to verify that the test setup was working properly.

The interpixel diode junction current was so small compared to the noise in the measurements that the fit function including the interpixel diode junction current usually resulted in a value for I_S that was consistent with zero. Thus a simple linear fit produced similar results for measurement of R.

Results of all data sets are included in table 4.1, even those taken while the detector was cooling down or warming up and when light leaks caused photo current in excess of the signal. Better data runs could have been taken by reducing light leaks. But, as the results indicated the resistance was far too high to explain the detector noise, further testing was unnecessary.

4.2.2 Sheet Resistance

A spare PCB for the automated wafer tester (see figure 4.2) was used to make connections to test sheet resistance. The test board only provided connections to pins on the feedthrough flange, it did not connect any of the pins together on the board. Two resistances are of interest: the resistance between a pixel and the readout pin, and the resistance between a pixel and the bias pin.

On the readout side each pixel only has a single pin, so its resistance cannot be measured. However, the guard ring is of similar construction to the pixels and has 12 pins, so it was measured and the pixels were assumed to have the same sheet resistance.

The bias has 24 pins, but it conducts across a TiN coated lightly doped section and an uncoated n++ doped silicon section with different resistances. Measurements were made

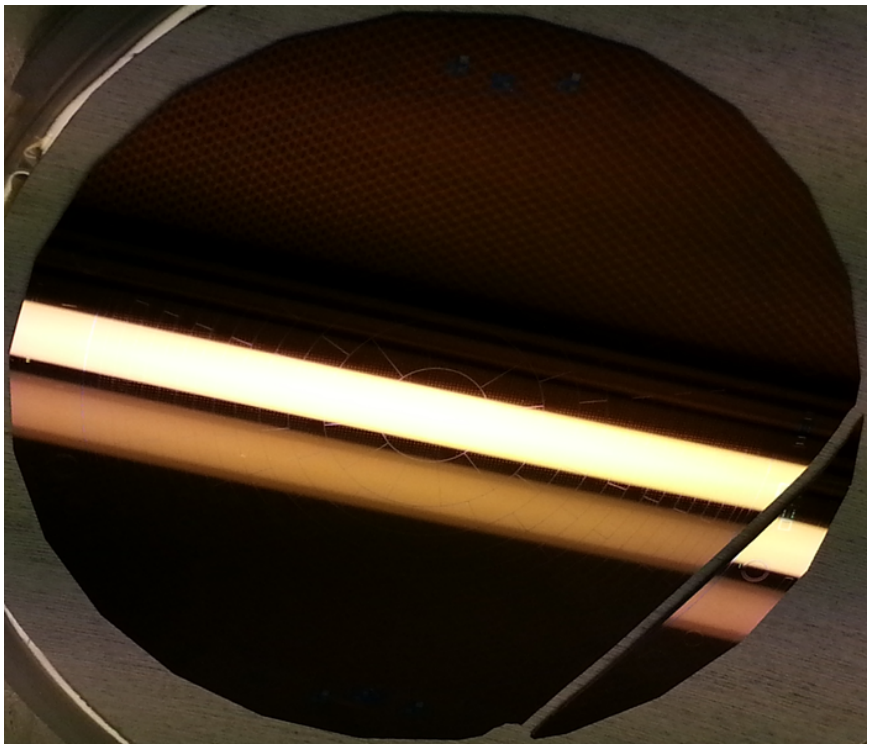

Figure 4.8: FPD wafer 1115876. The chip on the side cuts through the bias ring about halfway into the guard ring, leaving five bias pins and one guard ring pin unconnected. The semicircle region missing on the bottom of the photo is where the bolt head that started the crack was positioned. The readout side of the wafer is shown, and the segmentation pattern can be faintly seen on some of the wafer. The reflection in the wafer is the inside of a laminar flow hood, the white streaks are fluorescent bulbs.

Pixel	$R\,(\mathrm{G}\Omega)$	$-1\,\sigma$	$+1\,\sigma$	$I_L(\mathrm{pA})$	$T\,(\mathrm{C})$	$V_{bias}\,(\mathrm{V})$	notes
121	5600	1700	∞	52	-4.6	10	starting from 1V stepping to 0V, cooling down
121	510	450	580	55	-5.2	20	0V to 1V, cooling down
121	510	420	650	53	-5.8	30	1V to 0V, cooling down
145	770	620	1010	46	-6.4	30	1V to 0V to 2V, cooling down
145	9900	1800	∞	31	<-13.8	30	0V to 3V, T stable
145	1700	1100	4200	34	<-13.8	60	0V to 3V, T stable
145	7700	2400	∞	38	<-13.8	100	0V to 2V, T stable
145	1210	1070	1390	37	<-13.8	100	0V to 3V, T stable
3R	11.7	10.1	14.1	32	1.5	0	0V to 1.4V, warming up, frosted
R	95.9	94.5	97.3	0.3*	7.5	0	0V to 1.4V, T stable
145R	128	116	143	68	21.8	100	0V to 2V, T stable
145R	131	119	146	3.7	-10.8	100	0V to 2V, T stable

Table 4.1: FPD interpixel resistance measurements. The wafer was not connected during the test marked *, so I_L should be 0. The 0.3 pA offset in the fit was probably due to offsets on the voltmeter and picoammeter. -13.8 C was the lower limit of the RTD readout. What was measured was current, which is inversely proportional to resistance, so error limits on the measurement that cross zero can result in an error limit on resistance of infinity. A loss of nitrogen flow resulted in the wafer being frosted. After the wafer was purged, the resistance never returned to previous values, yet it was still too low to cause the observed noise.

under a laminar flow hood with the lights on. All pins not used for testing were left floating.

4.2.2.1 Guard Ring

For the guard ring, sheet resistance was measured using a four-point method. By applying a current through two pins, and measuring the voltage on two other pins, the voltage drop due to current through the pin contacts was eliminated. The conversion from measured voltage and applied current to sheet resistance was determined by comparison to a model using Comsol version 5.2. Assuming the guard ring has uniform sheet resistance, for a current applied on pins on opposite sides of the guard ring and voltage measured on pins adjacent to the current terminals, the conversion factor is 44.3 squares (1 A of current and 1 $\Omega/\square$ sheet resistance would result in measuring 44.3 V between the measurement pins).

As a second method of determining sheet resistance and determining the pin contact resistance, the resistance between multiple pin combinations was also measured. For a measurement between pin A and pin B the resistance is:

$$R_A + R_B + R_G \left(((A - B) \ mod 12)^{-1} + ((B - A) \ mod 12)^{-1}) \right)^{-1} \tag{4.6}$$

where R_A is the resistance due to pin A, R_B is the resistance due to pin B, R_G is the resistance of a 30-degree arc on the guard ring, and A and B are pin numbers around the guard ring numbered consecutively. Measuring a sufficient number of pin combinations allowed determining the resistance of a 30-degree arc on the guard ring, as well as the resistance due to each of the pins used. The resistance of a 30-degree arc around the guard ring was converted into a sheet resistance by determining the arc to be 12.04 squares from a Comsol model.

4.2.2.2 Bias Ring and Uncoated Face

The bias ring is more difficult, as the TiN coating covers the downstream side and edges of the wafer, but not the upstream side. Thus the model must be broken up into two sections. The downstream side and edges have one sheet resistance, and the upstream face has another.

The relative resistance between the two regions was determined from the voltage distributions around the bias ring. If the upstream face of the wafer conducts very little compared to the TiN coated portions, then the voltage measurements on pins between the terminals will be evenly distributed. But, if the upstream face conducts sufficiently well, the voltage difference between adjacent pins will be greater closer to the terminals than midway between terminals. The voltage distribution around the ring was modeled in Comsol for many ratios of sheet resistance between the two regions, with current applied to opposite pins on the bias ring and voltages measured on the remaining pins. An interpolating function was fit to the Comsol results, generating smooth functions to fit the measured voltage distribution and allow determining the ratio of the sheet resistance of the two regions.

While the relative voltage distribution gives the ratio of the two surface conductivities, the actual voltage differences is directly proportional to the sheet resistance. However, the conversion from voltage and current to sheet resistance depends on the ratio of the two surface conductivities. The conversion to attain the sheet resistance of the TiN coated region was determined from the same Comsol models and fit with another interpolating function, and the ratio gave the sheet resistance of the uncoated region.

4.2.2.3 Sheet Resistance Results

Two wafers were used for testing. Wafer 1115876 is another wafer from the third batch, the same batch as the wafer installed when the increase in noise was found, which had a chip taken out of it that extends through the bias ring and partway into the guard ring. This required a different model than that of the undamaged wafers. Wafer 76040 was tested for comparison, which is a wafer from the second batch, which is the same batch as the wafer installed before the noise degradation was observed. It was an undamaged wafer and used the standard wafer models.

Wafer 76040 Guard Ring

The four-point measurement of wafer 76040's guard ring measured 2.09 V with an applied current of 0.97 mA. From the Comsol model the conversion factor was 44.3 for a sheet resistance of 48.7 $^{\Omega}/_{\square}$.

Resistance was measured between six pins, resulting in 15 measurements to determine seven unknowns. Using a least-squares fit, the sheet resistance measured 63.5 $^{\Omega}/_{\square}$ and pin contact resistance contributions measured $G0 = 259\,\Omega$, $G1 = 286\,\Omega$, $G_5 = 295\,\Omega$, $G_6 = 290\,\Omega$, $G_7 = 427\,\Omega$, and $G_{11} = 287\,\Omega$. The large disagreement between the two methods indicates the uniform sheet resistance model is likely inaccurate.

For a pin contact with a sheet of conductor, where the contact region has a radius much larger than the thickness of the conductor, the contribution of the contact has a logarithmic dependence on the radius of the contact region:

$$R\left(r_c \gg t\right) = \int_{r_c}^{r_f} \frac{\sigma}{t}\frac{1}{2\pi r}dr = \frac{\sigma}{t}\frac{1}{2\pi}\ln\frac{r_f}{r_c} \tag{4.7}$$

where σ is resistivity of the conductor, t is the thickness of the conductor, r_c is the radius of the contact region, and r_f is an outer radius where the sheet no longer extends in all directions. For a measurement on the guard ring, r_f should be on the order of 1 mm. The contribution for 0.127 mm diameter pins on a 0.1-mm-thick coating was modeled in Comsol, 0.328 squares would have been expected from equation 4.7 and 0.429 squares was the model result.

For a pin contact where the contact region has a radius much smaller than the thickness of the conductor, there will be an additional resistance with a 1/r dependence from the contact region through the thickness of the conductor:

$$R\left(r_c \ll t\right) = \int_{r_c}^{r_i} \sigma\frac{1}{2\pi r^2}dr = \sigma\frac{1}{2\pi}\left(\frac{1}{r_c} - \frac{1}{r_i}\right) \tag{4.8}$$

where r_i will be on the order of the thickness of the conductor.

Measuring a minimum pogo-pin contribution of 4 squares ($\frac{\sigma}{t}$) indicates the effective

pin contact radius is on the order of the thickness of the conductor. Since such a large contribution is unlikely to come from the logarithmic dependence of a circular geometry, and more likely to come from the 1/r dependence of spherical geometry. The pogo pins have round tips, with a radius of 370 μm. From equation 4.7 the contact region had an effective radius around 17 μm, which would be expected if the pin only penetrated 0.4 μm into the surface without deforming. The second batch of wafers, to which wafer 76040 belongs, had no discoloring visible on the wafer, while wafers from the third batch had a gold hue. This also suggest the TiN coating on the third batch wafers is likely much thicker than the second batch wafers.

Wafer 76040 Bias Ring and Face

Wafer 76040 was a poor fit to the model. The voltage difference between pins close to one current terminal were significantly different than those close to the other terminal. The voltage between a pin adjacent to a terminal and the next adjacent pin should have been the same for the four pairs of such pins, by symmetry. But measured values were 57.6 mV, 52.2 mV, and 29.7 mV. Only three values were obtained as five pins were not connected. This was yet another indication that the conductivity across the TiN coating was significantly non-uniform. For function fitting the voltage on pins that should have been the same by symmetry was averaged.

Wafer 76040 was measured to have a conductivity ratio of the uncoated region to the TiN coated region of $45\pm^{32}_{8}$. The measured maximum voltage difference across measurement pins was 123.5 mV with an applied current of 0.977 mA. The conversion factor from the model is $0.080\pm^{0.006}_{0.013}$ squares.

Sheet resistance of TiN coated region $1580 \pm^{300}_{110}$ $\Omega/\square$.

Sheet resistance of uncoated region $35 \pm^{4}_{11}$ $\Omega/\square$.

The uncertainties are only the statistical fit uncertainties. As the uniform sheet resistance model only approximated the actual wafer, the actual error may be larger by an unknown amount. From the disagreement of the two guard ring resistance measurements, a factor of

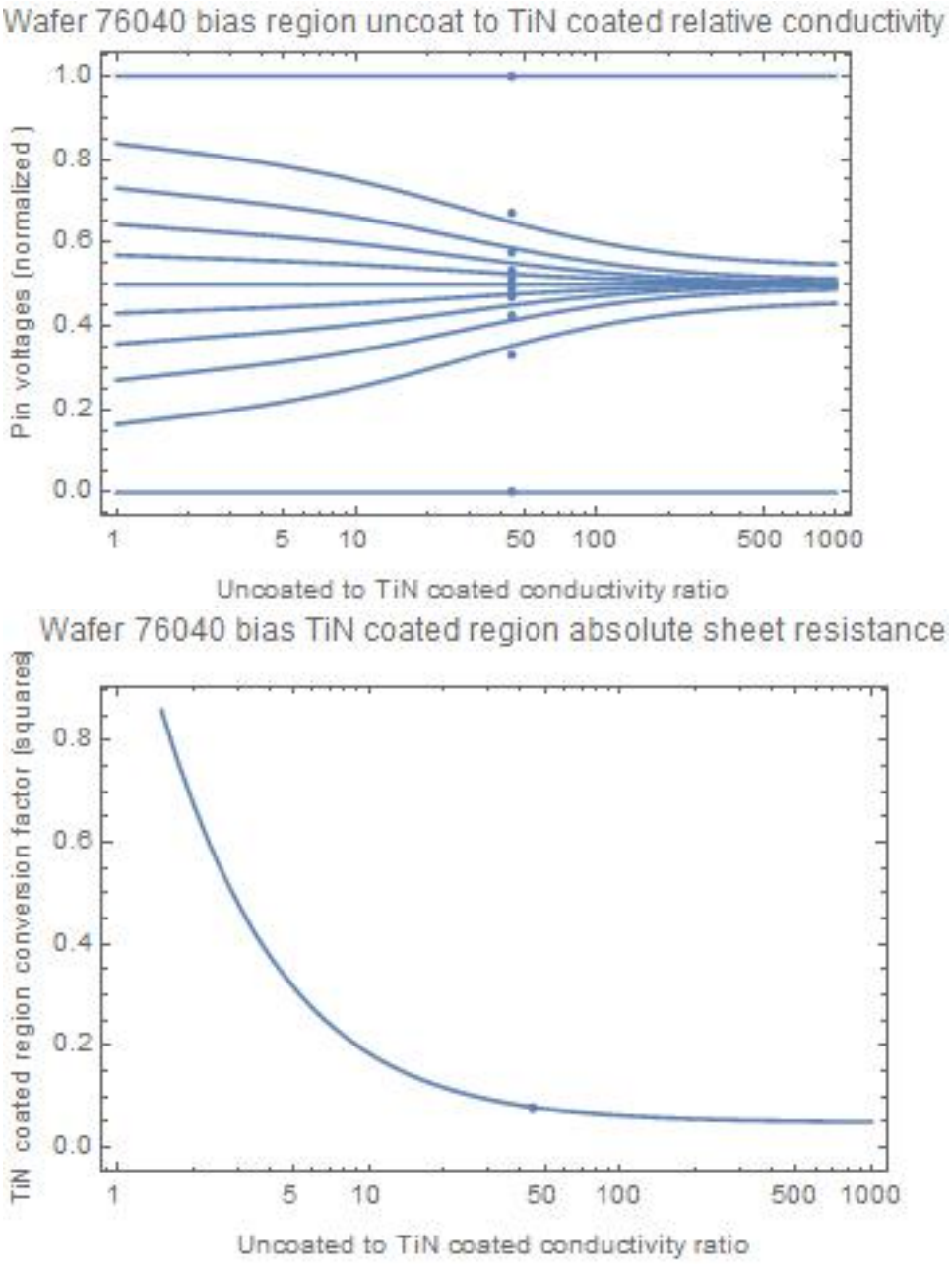

Figure 4.9: Top: wafer 76040 voltage distribution curves and best fit values for uncoated to TiN-coated surface conductivity ratio. Bottom: conversion from measured voltage and applied current to TiN-coated surface sheet resistance.

1.3 is reasonable.

Wafer 115876 Guard Ring

Wafer 115876 is the wafer from the same batch as the installed wafer. But, it has a chip extending part way through the guard ring. Current was applied through opposite pins of the guard ring and it was ensured that the chip was not between a current terminal and an adjacent measurement pin. The four-point measurement method measured 39.9 mV on the pins with an applied current of 0.97 mA. From the wafer 115876 Comsol model, the conversion factor was 52 for a sheet resistance of 0.79 Ω/□.

Measuring the resistance between pins for four pins on the guard ring resulted in six measurements, the minimum number to determine the resistance of the four pins, the sheet resistance of the guard ring, and the additional resistance due to the chip. The sheet resistance measured 1.6 Ω/□ (19.28 Ω per 30 degree arc of 12.04 squares), the chip added 16.5Ω, and the resistance due to the pogo-pin contacts was $G_0 = 10.1\,\Omega$, $G_1 = 1.52\,\Omega$, $G_6 = 2.92\,\Omega$, and $G_7 = 33\,\Omega$. The two measurements differed by a factor of 2, when the test equipment used should have been accurate to 1%, indicating the uniform model used was likely inaccurate. However, as it would take a sheet resistance of over 100 Ω/□ to explain the noise, this was sufficient.

Wafer 115876 Bias Ring and Face

Instead of applying current through opposite sides of the bias ring, current was applied through pins two away from either side of the chip. The pins adjacent to the chip were used for the conversion from applied current and measured voltage to the sheet resistance of the TiN coated region. The wafer was measured to have a conductivity ratio of the uncoated region to the TiN coated region of $0.142\pm^{0.009}_{0.008}$. The voltage difference across measurement pins was 28.5 mV with an applied current of 0.97 mA. The conversion factor from the model is 7.32 ± 0.25 squares.

Sheet resistance of TiN coated region $4.01 \pm^{0.14}_{0.13}$ Ω/□.

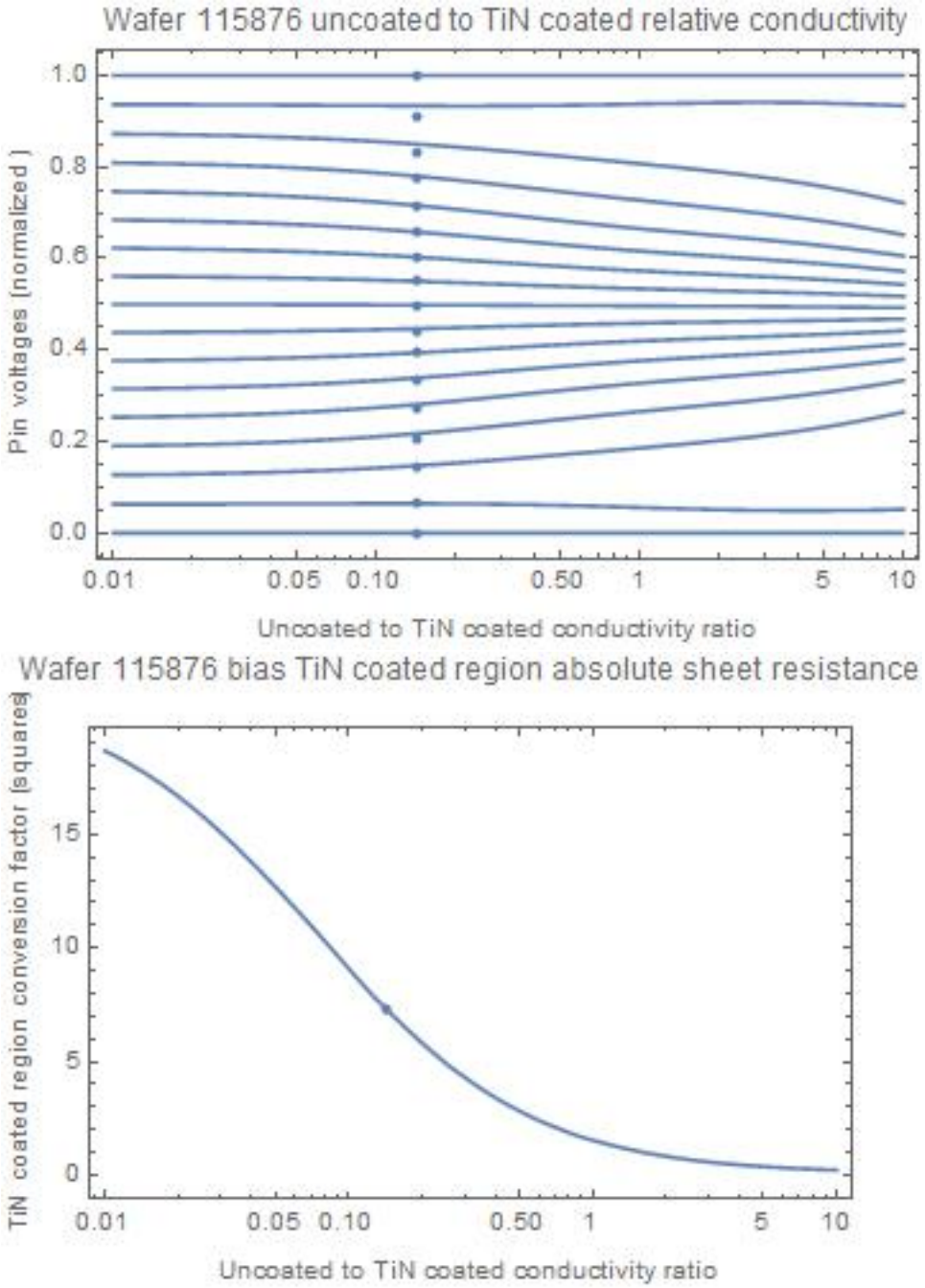

Figure 4.10: Top: wafer 115876 voltage distribution curves and best fit values for uncoated to TiN-coated surface conductivity ratio. Bottom: conversion from measured voltage and applied current to TiN-coated surface sheet resistance.

Sheet resistance of uncoated region $28.2 \pm^{0.63}_{0.68}\ \Omega/\square$.

As for the older wafer, the uncertainties are only the statistical fit uncertainties. From the disagreement of the two guard ring resistance measurements, a factor of two is reasonable. However, the sheet resistances were better than those of the older wafer and far too low to account for the increased noise.

4.2.3 Forward Bias Resistance

The resistance of the pixels was measured by applying a forward bias to the diode through all bias pins to a pixel readout pin, and measuring the voltage vs. current curve. This measurement was fit to a model of an ideal diode in series with a resistor. Using the Shockley diode equation 4.1, and Ohm's law:

$$I = \frac{V}{R} \tag{4.9}$$

The applied voltage $V = V_d + V_R$ is used to substitute into the Shockley diode equation (equation 4.1):

$$I = I_s \left(e^{V - I\,R/nV_T} - 1 \right) \tag{4.10}$$

Using the main branch of the Lambert W function, $W_0(z)$ is the solution for w in $z = we^w$ with the constraint that $w \geq -1$.

$$I + I_S = I_S e^{V/nV_T} e^{-I\,R/nV_T} e^{I_S\,R/nV_T - I_S\,R/nV_T} \tag{4.11}$$

$$\frac{R}{nV_T} I_S e^{V/nV_T} e^{I_S\,R/nV_T} = \frac{R}{nV_T} \left(I + I_S \right) e^{I\,R/nV_T} e^{I_S\,R/nV_T} \tag{4.12}$$

$$I = \frac{nV_T}{R} W_0 \left(\exp\left(\frac{I_S R + V}{nV_T} \right) \frac{I_S R}{nV_T} \right) - I_S \tag{4.13}$$

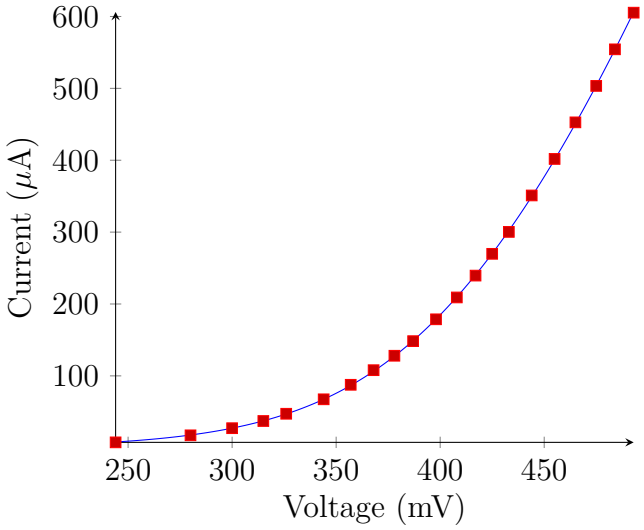

Figure 4.11: Diode and series resistor current vs. voltage example fit, for pixel 123 on wafer 115876. $I_s = 3.4$ nA, $nV_T = 44$ mV, $R = 96\ \Omega$.

where I_S is the reverse bias saturation current, n is the ideality factor which should fall between 1 and 2, and V_T the thermal voltage which should be around 26 mV at room temperature. An example fit is shown in figure 4.11.

The forward bias resistances of four pixels on wafer 76040 were measured with a mean resistance of $437 \pm 19\,\Omega$. The forward bias resistances of ten pixels on wafer 115876 were measured, with a mean resistance of $131 \pm 87\,\Omega$. The large variation in pin contact resistance, as well as the large pixel position dependence due to the chip through the bias ring, makes the measurement for wafer 115876 vary drastically. However, it was still significantly better than the wafer from the previous batch and lower than the model resistance that would explain the noise, indicating the series resistance was most likely not a problem.

Wafer 76040:

Pixel	I_S (nA)	nV_T (mV)	R_S (Ω)
3	231 ± 85	61.4 ± 3.8	445 ± 15
49	100 ± 33	52.0 ± 2.6	420 ± 10
97	38.5 ± 6.6	43.8 ± 1.0	417 ± 4
145	35.3 ± 5.4	42.6 ± 0.9	465 ± 4

Wafer 115876:

Pixel	I_S (nA)	nV_T (mV)	R_S (Ω)
145	16.3 ± 1.7	40.03 ± 0.59	99.5 ± 10.9
97	14.7 ± 1.1	40.07 ± 0.44	106.6 ± 9.1
49	11.2 ± 1.2	39.30 ± 0.65	185.3 ± 27.0
3	24.0 ± 0.9	45.18 ± 0.21	71.5 ± 1.0
147	38.7 ± 2.2	44.66 ± 0.30	24.5 ± 0.5
99	68.4 ± 18.9	49.50 ± 1.89	214.5 ± 6.5
51	34.5 ± 2.8	45.82 ± 0.47	38.6 ± 1.5
27	29.7 ± 1.8	45.72 ± 0.35	142.7 ± 1.2
75	123.2 ± 29.9	55.46 ± 2.04	327.8 ± 7.7
123	33.7 ± 2.3	44.40 ± 0.38	95.6 ± 1.3

4.2.4 Wafer Testing Conclusions

From all measurements performed, no apparent explanation emerged for the increase in noise on the third batch of FPD wafers. The newer wafer was better than the wafer from the previous batch for every compared parameter. It is likely the resistance across the wafers is significantly nonuniform, which caused significant error when uniform models were used to determine parameters. Variations in the sheet resistance could be detected using a small, four-point probe to make many measurements across the wafer, instead of making measurements using pin contacts of a mounted wafer. However, such testing is unwarranted

as it would not explain the overall reduced detector resolution.

The third batch wafer measured a significantly lower resistance for the TiN coated region than the n++ doped region, while the second batch wafer measured a significantly higher resistance for the TiN coated region. This suggests that the TiN coating was too thin in the second batch of wafers to contribute significant conductivity, and the measured resistance was comparing the heavily doped n++ region to the lightly doped p region beneath the TiN coating.

It was later found the noise kept increasing, even with the same wafer installed. Furthermore, it was noticed the noise increased after the detector system had been opened. This also indicates that manufacturing differences between the second and third batch of wafers are unlikely to be the cause of the increased noise.

Chapter 5

MAC-E TIME-OF-FLIGHT

5.1 Time-of-Flight Overview

The normal operation mode for KATRIN is to adjust the retarding potential of the main spectrometer to perform the beta energy spectrum measurement. Each point gives a measurement of the total rate above that retarding potential, and the spectrum is mapped out by making measurements at many retarding potentials. An alternative method is to measure the transit time through the spectrometer.

The low magnetic field, high retarding potential, already required for the normal MAC-E filtering technique is the same as required for a time-of-flight measurement of the energy spectrum. The retarding potential can be set close to the energy spectrum endpoint, so that the electrons are moving very slowly through the high potential region compared to the rest of their path, making the transit time in all but the high potential region negligible. The time-of-flight then gives a measure of the momentum of the electron parallel to the magnetic field, the same parameter that is being filtered on by the normal MAC-E mode, with a resolution determined by the ratio of the magnetic field in the high electric potential region to the maximum magnetic field (see equation 2.3).

This results in a measurement of the electron energy with nearly the same resolution as the normal MAC-E filter technique. However, whereas the normal method only measures the rate above the retarding potential, time-of-flight mode measures the energy of each electron that makes it through the retarding potential. This can be used to reject background, since when an electron is detected after the main spectrometer the time-of-flight gives a region in time to look for the electron entering the main spectrometer. Time-of-flight mode also measures the region near the endpoint all at once instead of point-by-point. This gives a

substantial reduction in the run time required to make a spectrum measurement. For three years of measurement time a time-of-flight mode could result in a statistical error around 0.004 $^{eV^2}/_{c^4}$, compared to 0.018 $^{eV^2}/_{c^4}$ for the standard mode [52].

5.2 Calculating Time-of-Flight Spectrum

To determine the neutrino mass from time-of-flight spectra, the time-of-flight spectrum needs to be expressed in terms of fit parameters. The spectrum is a sum of spectra with different final-state energies, the square of the neutrino mass, an unknown background rate, the relative signal amplitude, and the endpoint energy as fit parameters. The spectrum for a given electric and magnetic field, with unknown neutrino mass, without background and to a single endpoint energy is what is calculated here.

Assuming no energy is lost, only reduced and then recovered by the retarding potential, the electron speed parallel to the magnetic field is given by [52]:

$$v_{\shortparallel}\left(B,U\right)=\frac{\sqrt{p_{\shortparallel}^{2}\left(B,U\right)c^{2}}c}{E+mc^{2}-qU} \tag{5.1}$$

The electron momentum parallel to the magnetic field is:

$$p_{\shortparallel}^{2}\left(B,U\right)c^{2}=\left(E+2mc^{2}\right)\left(1-\sin^{2}\theta\frac{B}{B_{s}}\right)+e^{2}U^{2}-2eU\left(E+m_{e}c^{2}\right) \tag{5.2}$$

Where B is the magnetic field, B_s is the magnetic field in the source, U is the retarding potential, θ is the pitch angle in the source, E is the initial kinetic energy in the source, γ is the relativistic gamma factor in the source, e is the electron charge, m is the electron mass, and c is the speed of light. The time of flight is found by integrating the reciprocal of this speed over the path through the spectrometer.

$$\tau\left(E,\theta\right)=\int\frac{ds}{v_{\shortparallel}\left(B\left(s\right),U\left(s\right)\right)} \tag{5.3}$$

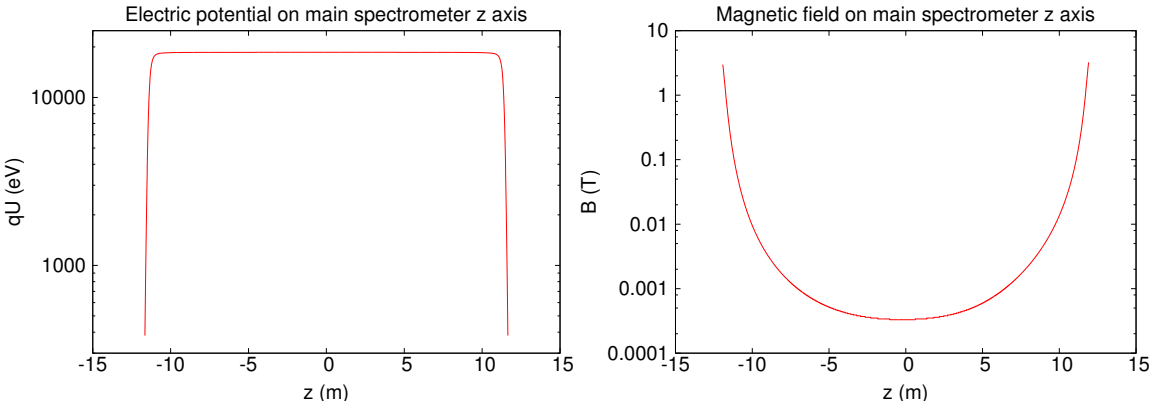

Figure 5.1: Electric potential and magnetic field along axis of KATRIN main spectrometer. Reprinted from Steinbrink et al. [52]

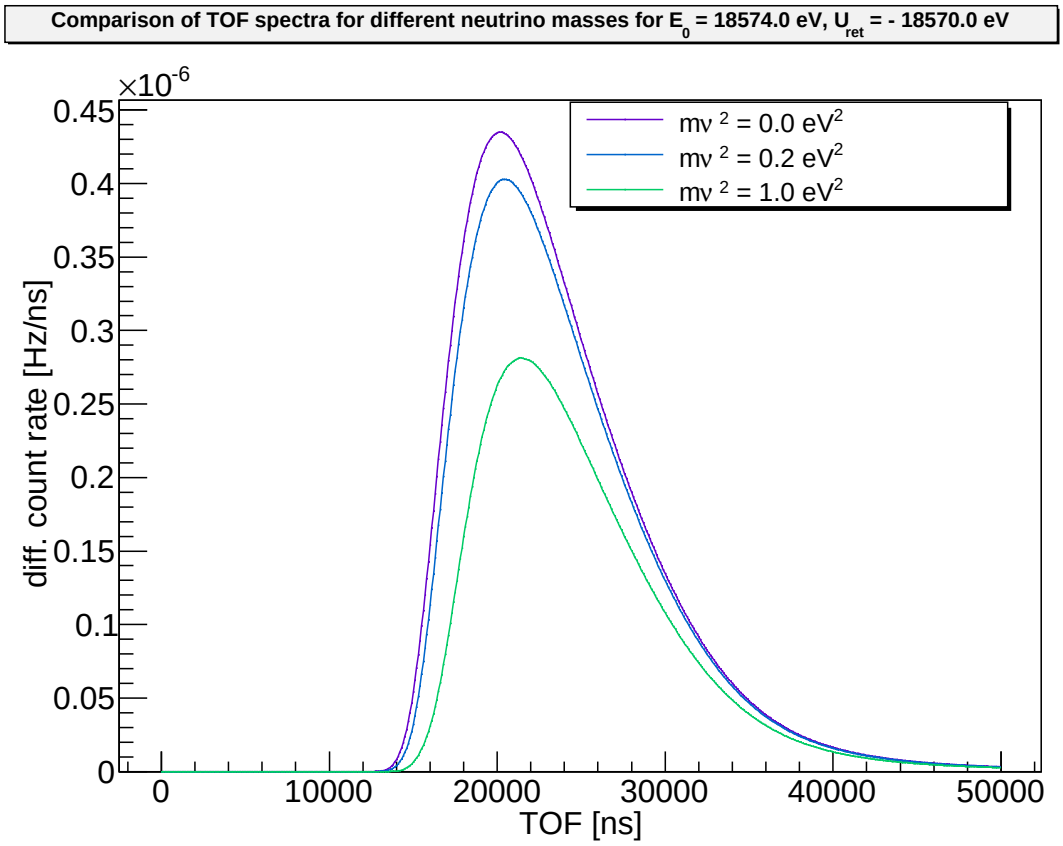

Figure 5.2: Time-of-flight spectra for different neutrino masses with a retarding potential 1V below the end point energy. Reprinted from Steinbrink et al. [52]

5.3 Electron Tagger

In order to implement a time-of-flight mode, the electron transit through the spectrometer must be known, requiring a time stamp before and after the spectrometer. The detector already provides a time stamp after the spectrometer with around 100 ns time resolution, thus only the addition of an electron detector before the spectrometer is required. On the downstream end the electron may be absorbed, and methods to detect the absorption are well-known. However, on the upstream end the electron needs to be minimally disturbed, or at least the effect on the electron needs to be well-known, as any uncertainty in the change to the electron will contribute an uncertainty in the starting energy of the electron. This makes the upstream detection of the electron much more difficult, as it requires a passive electron detector. This passive electron detector is hereafter referred to as an electron tagger.

Chapter 6

ELECTRON TAGGER

6.1 Electron Tagger Methods Considered

To produce a sufficiently accurate time-of-flight spectrum the timing resolution needs to be on the order of 1 μs. The electron tagger needs to be before the main spectrometer to allow measuring the time-of-flight through the main spectrometer, and also after the pre-spectrometer for noise reasons discussed in chapter 7.1.

Between the pre-spectrometer and main spectrometer is a 4.5 T magnet, where the beam line comes to its narrowest diameter of 10 cm. Inside the bore of this magnet is a valve with room to place an electron tagger. The available space is 15 cm long and 20 cm in diameter, allowing 2.5 ns to detect a passing electron traveling at around a fifth the speed of light. The valve could be removed, lengthening the distance available. The length of the magnet winding is 32 cm [40, p. 133], so an observation time much longer than 5 ns is not possible without changing the beam line.

The passing of a single electron has been accomplished for small circuits, such as detection the movement of single electrons between quantum dots [53]. But for use in KATRIN the tagger would need an aperture with at least a 10 cm diameter. While this seems theoretically possible, and many methods were considered for the construction of an electron tagger, no method was found that would provide a working detector. Prototypes for two different resonant structure detectors were constructed. However, no signal from the passing of single electrons was detected.

Methods considered included:

- Detecting cyclotron radiation.
- Detecting induced charge.
- Detecting energy change in resonator.
- Detect image current with SQUID.

6.1.1 Cyclotron Radiation

The power radiated by the electron due to motion in the magnetic field is given by the Larmor formula [54, p. 666]:

$$P = \frac{e^2}{6\pi\epsilon_0 m^2 c^3} \frac{dp_\mu}{d\tau} \frac{dp^\mu}{d\tau} \tag{6.1}$$

where e is the electron charge, m is the electron mass, c is the speed of light, ϵ_0 is the vacuum permittivity, p is the electron four-momentum, and τ is proper time. The electron gyration frequency is given by:

$$\omega = \frac{eB}{\gamma m} \tag{6.2}$$

where γ is the Lorentz factor and B is the magnetic field. For the 4.5 T field between the KATRIN pre-spectrometer and main spectrometer, at the maximum pitch angle of 51 degrees for momentum, this averages out to only 12 fW emitted at 122 GHz. For a reasonable observation length, the observation time will be on the order of 10 ns. Even if all the cyclotron radiation could be collected, the detector would need to be cooled to 9 K before the signal was equal to thermal fluctuations.

A major problem for the cyclotron radiation scheme is the bandwidth. As the observation time is on the order of 10 ns, the bandwidth will need to be on the order of 10^8 radians/second. Assuming the radiation is detected by an antenna array that is only 10 cm in diameter (the

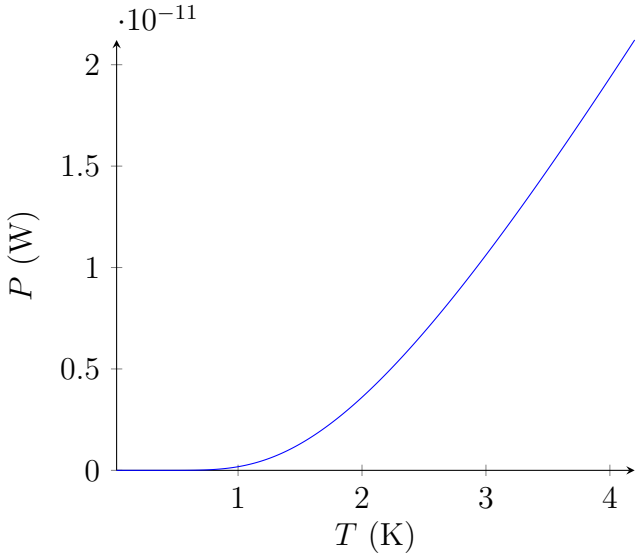

Figure 6.1: Expected blackbody background for a 16 MHz FWHM band centered at 122 GHz, for a sphere of radius 5 cm.

diameter of the beamline) and the antenna response is a Lorentzian with a full width at half maximum of 16 MHz, the antenna would need to see a temperature of 0.7 K before the power from blackbody radiation would be the same as signal power. As the detector region requires a 10 cm-diameter opening on both ends this seems a very difficult temperature to achieve. The background also can't be considered relatively constant. At 12 fW the electron produces on the order of a single 122 GHz photon in 10 ns, as does the background radiation at 0.7 K. The noise could be reduced by a factor of two using antennae only sensitive to one direction of circularly polarized light. Since the peak of the blackbody radiation curve is moving closer to the gyration frequency, the background would need to be cut by a factor of 10^3 before reaching a signal-to-noise ratio of one for 4 K.

6.1.2 Image Charge

A pickup could be used to pass the image charge through a load circuit. The prospect of detecting this charge with a single electron transistor (SET) was explored, as such devices

have been reported to have the required sensitivity of one electron in 10 ns [55]. However, the devices require a very low capacitance on the island to operate. In order to function the device must form a Coulomb blockade, which required the thermal energy to be much less than the charging energy on the island.

$$k_b T \ll \frac{e^2}{2C} \tag{6.3}$$

where k_b is Boltzmann's constant and e is the electron charge. At a temperature (T) of 4 K, this requires a capacitance (C) under 0.2 fF. While useful for small circuits, like detecting the current flowing between quantum dots [53], attaching a large probe suitable for detecting an electron 5 cm away will result in a far larger capacitance than that of the SET island. The charge is split between the SET and the probe, with the effective charge on each given by their fraction of the total capacitance. Since the SET has a capacitance much smaller than the probe, almost no charge is present on the SET. A charge transformer can couple a high capacitance probe to a low capacitance electrometer [56]. A charge transformer uses an array of capacitors and switches to connect the capacitors to the high capacitance probe in parallel, so the capacitors will have a high total capacitance. The switches then rearrange the capacitors to be in series with the low capacitance electrometer, so the capacitors will have a low total capacitance (see figure 6.2).

For n capacitors with capacitance C_t, coupled to a probe with capacitance C_p and a detector with capacitance C_d, the charge transferred to each capacitor of the charge transformer for an initial charge on the probe of Q is:

$$Q_t = Q\frac{C_t}{C_p + nC_t} \tag{6.4}$$

When the capacitors are rearranged in series with the detector, the charge transferred to the detector is:

$$Q_d = Q_t\frac{C_d}{C_d + \frac{C_t}{n}}$$

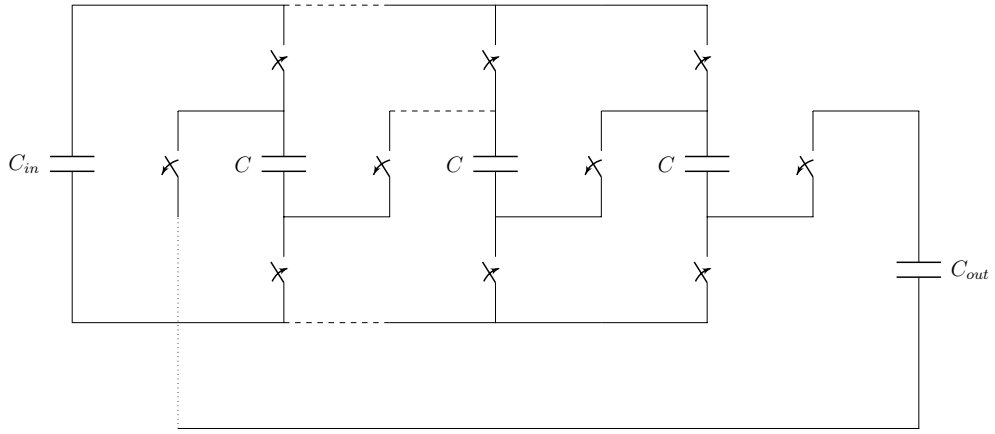

Figure 6.2: Charge transformer. Arrows show position of switches when the charge transformer is connected to the high capacitance input. Switches toggle for connection to the low capacitance output.

This takes its maximum value of $Q/4n$ when $n = \sqrt{C_p/C_d}$ and $C_t = \sqrt{C_p C_d}$. This charge splitting is unlikely to transfer any charge when the charge in question is a single electron. Furthermore, the stray capacitance of the switches is expected to be problematic. For a probe with 10 pF capacitance coupled to an SET with 1 fF capacitance, it would take 100 capacitors with 100 fF each to maximize the charge transfer. The switches would each need to be under 10 aF of stray capacitance, otherwise they would present a significant stray capacitance [57].

6.1.3 Current Induced by Magnetic Field

The passing electron produces a time-varying magnetic field, which in principle could be used to drive a load. While the electron does have an intrinsic magnetic moment, it is much smaller than that due to the gyration of the electron in the magnetic field. Treating the electron gyration as a current loop to find the magnetic moment, the magnetic moment is:

$$M = I\,A \tag{6.5}$$

where I is the current on the loop and A is the area enclosed by the loop. The gyration frequency is given by equation 6.2. The gyration radius is given by:

$$r = \frac{\gamma mc\beta \sin\theta}{eB} \tag{6.6}$$

where θ is the electron pitch angle with the magnetic field, B is the magnetic field strength, β is the electron speed divided by the speed of light (c), γ is the Lorentz factor, and m is the electron mass. Which leads to a magnetic moment of:

$$M = \frac{e\omega}{2\pi}\pi r^2 = \frac{\gamma mc^2\beta^2 \sin^2\theta}{2B} \tag{6.7}$$

The electrons of interest are those near the tritium beta decay endpoint with a pitch angle small enough to make it through the pinch magnet as determined by equation 2.2. This leads to an average magnetic moment of $2.55 \cdot 10^{-15}\text{A}\cdot\text{m}^2$. The pickup could be multiple loops of wire which could have individual current sensors, but the total current would still be the same as a single conductor. Assuming the pickup is a single loop of superconductor, the maximum current induced will be less than that which is necessary to generate a magnetic moment in the pickup which cancels that of the electron. Using formula 6.5 for the pickup with the beam line radius of 5 cm the current comes out to $3.25 \cdot 10^{-13}$A. The current in the loop will appear as a pulse, with an amplitude limited by this value, and the pulse will be present for a most 10 ns, which means the total charge collected will be limited to around 0.02 e. The change in charge on a grounded probe that represents the image charge of the passing electron should be a significantly higher fraction of an electron charge, which makes this method unattractive.

Another approach is to consider the total flux through a 5-cm radius superconductor loop forming a very large SQUID, assuming the electron is traveling along the axis of the loop. The total flux through the plane of the loop, extending to infinity, is zero. Even when the electron is crossing the loop this is true, as the flux inside the path of the electron cancels with the flux outside. So the flux through the loop can be easily found by integrating the

field from a dipole out to infinity. This takes a maximum when the electron is in the center of the loop:

$$\Phi_{max} = \int_{r_{min}}^{\infty} M \frac{\mu_0}{4\pi} 2\pi r \, dr = M \frac{\mu_0}{2\, r_{min}} \tag{6.8}$$

where μ_0 is the permeability of free space. Which is $3.2 \cdot 10^{-20}$ Wb or about 150 $\mu\Phi_0$ where Φ_0 is the micro magnetic flux quanta. In a 10 ns window it would require a sensitivity of $1.5\,{}^{\mathrm{n}\Phi_0}/\sqrt{\mathrm{Hz}}$ to detect. A level beyond the sensitivity of even a small SQUID.

6.1.4 Image Current

The passing electron induces an image charge in a pickup. An inductor coupled to a SQUID could be used to generate a change in flux seen by the SQUID.

Change in current on an inductor is:

$$\frac{di}{dt} = \frac{V}{L} \tag{6.9}$$

where V is the applied voltage and L is the inductance. Assuming the inductor has enough inductance that the voltage across the SQUID is always that of the electron to the probe, this gives a voltage on the inductor on the order of:

$$V = \frac{e}{4\pi\epsilon_0 r} \tag{6.10}$$

where e is the electron charge, ϵ_0 is the permittivity of free space, and r is the distance form the electron to the probe. The flux through the inductor is:

$$\Phi = \frac{iL}{N} \tag{6.11}$$

$$\frac{d\Phi}{dt} = \frac{L}{N}\frac{di}{dt} = \frac{V}{N} \tag{6.12}$$

where i is the current and N is the number of turns. Due to available space for the pickup, r will be about 5 cm and the voltage will exist for a time of about 10 ns. For a

single-loop inductor, this gives a flux change of about 0.14 Φ_0 where Φ_0 is the magnetic flux quanta. For 10 ns this requires a sensitivity of about 4.4 $\mu\Phi_0/\sqrt{\text{Hz}}$, within the range of a typical SQUID.

A major issue arises using single loop for the required inductance. As the inductance forms an oscillator with the parallel capacitance, the actual response is a resonance which is derived in section 6.2.5. In order for the full voltage to be applied to the inductor, the transit time across the loop needs to be shorter than the loop oscillation period: $\sqrt{LC}$ needs to be much larger than 10 ns. The probe capacitance (C) is about 3 pF, which requires an inductance of more than 33 μH. For a single loop inductor, this would require a loop much larger than 5 m diameter, which isn't feasible to couple to a SQUID. Using a multi-turn inductor couples better to a SQUID, but for the same inductance the flux is reduced by the number of turns. Another inductor in series with a smaller inductor could couple to the SQUID, but, most of the voltage would be across the other inductor.

A longer probe would increase the capacitance, and keep the electron in the probe region longer, thus reducing the frequency. Equation 6.10 assumes an ideal pickup and would no longer be suitable approximation, $V = \frac{e}{C}$ should be used instead. As $L = 1/C\omega^2$, and C is proportional to the length of the pickup, the size of the inductor will increase proportional to the pickup length. Since $V \sim 1/C$ the signal voltage will also decrease. A better option is likely taking advantage of the resonance response.

6.2 Energy Exchanged with Resonator

By passing the electron through some sort of resonant structure, an arbitrary amount of energy can be exchanged with the electron by driving the resonator to some high excitation. The energy exchanged is calculated by integrating the electric field over the electron path.

$$\Delta W = e \int E_z dz \tag{6.13}$$

where e is the electron charge, and E_z is the electric field along the electron path. The stored energy is calculated by integrating the square of the electric field and magnetic field

strength over the volume. This simplifies at a time when the electric field is at a maximum, and the magnetic field is zero:

$$W = \frac{\epsilon_0}{2} \iiint |E|^2 \, dV \tag{6.14}$$

$$\Delta W = \epsilon_0 \iiint \triangle E \cdot E \, dV \tag{6.15}$$

where ϵ_0 is the permittivity of free space. All the electric fields have a functional form that are only related by a single constant, for any given mode and cavity dimensions. The formulas for a right cylindrical cavity are given in section 6.37 but the relation holds for any resonant structure. If each field function is multiplied by E_0 and it is assumed this is the only thing that changes when the stored energy changes, the change in E_0 can be calculated, which doesn't depend on cavity excitation.

$$\Delta E_0 = \frac{e \int E_z dz}{\epsilon_0 \iiint |E|^2 \, dV} \tag{6.16}$$

This fact is used in section 6.2.3 to determine an effective cavity capacitance for modes of right cylinder cavities, where the maximum change in voltage from a passing electron is $\Delta V = {}^{e}/_{C}$. The amplitude of any signal coupled out of the cavity will be proportional to the electric field, so equation 6.16 is useful for determining an effective signal amplitude.

No method was ever found that took advantage of the possibility of a large change in stored energy, only the change in field. This apparent limit is discussed further in section 6.2.4. However, a resonant structure still has significant advantage in that the effect from the passing electron persists for a time determined by the resonator frequency and quality, which can easily be far longer than the time over which the electron is present near the probe. This allows for a reduction in the signal bandwidth.

6.2.1 Cylindrical Cavity TM_{010}

The first resonator considered was a right cylindrical cavity with the TM_{010} mode excited, with the electron passing through the cavity along the cylindrical axis where the electric field is maximum. The maximum energy exchange occurs when the electron travels much faster though the cavity than the field changes:

$$\triangle W \approx eV \tag{6.17}$$

where e is the electron charge and V is the cavity voltage:

$$V = E_0 d \tag{6.18}$$

where d is the cavity length and E_0 is the maximum electric field along the cylinder axis.

The cavity capacitance is given by:

$$C = \frac{\epsilon_0 a^2 \pi}{d} J_1 \left(j_{01}\right)^2 \tag{6.19}$$

where d is the length, J_1 is the first Bessel function of the first kind, and j_{01} is the first zero of the zeroth Bessel function. This is derived in section 6.2.3

This gives a resonant angular frequency of:

$$\omega = \sqrt{\frac{1}{LC}} = ck \tag{6.20}$$

where c is the speed of light and k is the wave number. From equations 6.19 and 6.20, the inductance[1] is:

[1]In Principles of Microwave Circuits [58], equations 6.19 and 6.21 differ by a factor of $\left(\pi J_1 \left(j_{01}\right) j_{01}^2\right)^2$. The resonant frequency of the cavity comes out the same, since the capacitance is multiplied by this factor and the inductance is divided by it. However, if used with the formula 6.23 for the energy stored on a charged capacitor, the voltage on a capacitor that would give the stored energy does not correspond with a change in energy with an electron of eV. Thus resulting in the factor applied to the capacitance and inductance compared to the frequently used formula, to force equation 6.17 to be accurate.

$$L = \frac{\mu_0 d}{\pi \left(J_1\left(j_{01}\right) j_{01}\right)^2} \tag{6.21}$$

The radius is:

$$a = \frac{j_{01}}{k} \tag{6.22}$$

While the length can be any value without affecting the frequency, it is favorable to have a small capacitance to produce a larger voltage change, and therefore a long length. The stored energy is:

$$W = \frac{1}{2} C V^2 \tag{6.23}$$

$$\Delta W = C V \, \Delta V \approx eV \tag{6.24}$$

$$\Delta V \approx e/C \tag{6.25}$$

For the region between the KATRIN pre-spectrometer and main spectrometer the magnetic field strength is 4.5T, while at the pinch magnet before the detector section the magnetic field strength is 6T. This limits the pitch angle of electrons that make it to the detector to 60 degrees through the tagger. For an endpoint electron with kinetic energy of 18.6 keV, this gives an average speed through the tagger of 0.2 c. It is reasonable to set the cavity length such that the electron traverses it in one half period:

$$d = \frac{0.2\, c}{2\, f} \tag{6.26}$$

where f is the cavity frequency and c is the speed of light. Averaging the integral of the electric field over the length of the cavity, with phase along the cavity given by the arrival phase ϕ and traversing the cavity in one half period, the square of the expected energy exchange is:

$$\left\langle \triangle W^2 \right\rangle = e^2 E_0^2 \frac{1}{2\pi} \int_0^{2\pi} \left(\int_0^d \cos\left(\pi d + \phi\right) \right)^2 d\phi = e^2 E_0^2 d^2 \frac{4\pi^2 - \sin\left(4\pi^2\right)}{2\pi^4} = 0.2\, e^2 V^2 \tag{6.27}$$

For test of concept, a detection apparatus was built using an the electron gun at CENPA, which can produce electrons in a range around 18.6 keV. Picking a frequency sets the cavity dimensions, which must fit inside the electron gun. For initial testing a frequency of 1660 MHz was chosen. This resulted in a half period length at 0.2 c of 18 mm and a cavity radius of 69mm, which can easily fit inside the electron gun for testing. Equipment was also commercially available at this frequency. From equation 6.19, this put the cavity capacitance at 2.0 pF.

The detection scheme was to excite the cavity with an oscillator, inductively coupled to the cavity by a loop located on the side of the cavity (see figure 6.3). The electron beam traveled through 3 mm-diameter holes in the center of the cavity, and the stored energy is measured by a pickup inductively coupled to the cavity in the same manner as the oscillator. The loops could be rotated to adjust coupling. The input was rotated to couple very weakly, so it wouldn't load the cavity significantly, and the output was rotated to attain a loaded quality factor around 1660. The signal would appear as a damped ringing with a 160 ns decay time in the 1660 MHz carrier. The signal was amplified and sent to a mixer that was driven by the same oscillator, then filtered so only the pulse from the ringing remained. The signal was further amplified, and sent to an oscilloscope. A silicon detector was placed after the cavity, to allow comparing the signal from the cavity to a separate electron detector.

Commercially available low-noise, but not cryogenic, components were selected. Due to the electron passing through the cavity in half a period, at 100 mV an RMS of 44 meV is expected to be transferred between the electron and the cavity. This is small compared to the energy resolution of the KATRIN main spectrometer of 1 eV, and would not result in a significant loss of resolution. The expected change in cavity energy compared to thermal energy stored in the cavity at room temperature was calculated to be 1.7 for 100 mV on the cavity. Despite the large change in energy, there seemed to be no way to take advantage of it. Instead, only the change in voltage was useful. The voltage change was expected to be 36 nV. The cavity was cooled by a pulse tube cooler to around 66 K, however, even at 4.2 K the thermal voltage fluctuations would still be 5.4 μV.

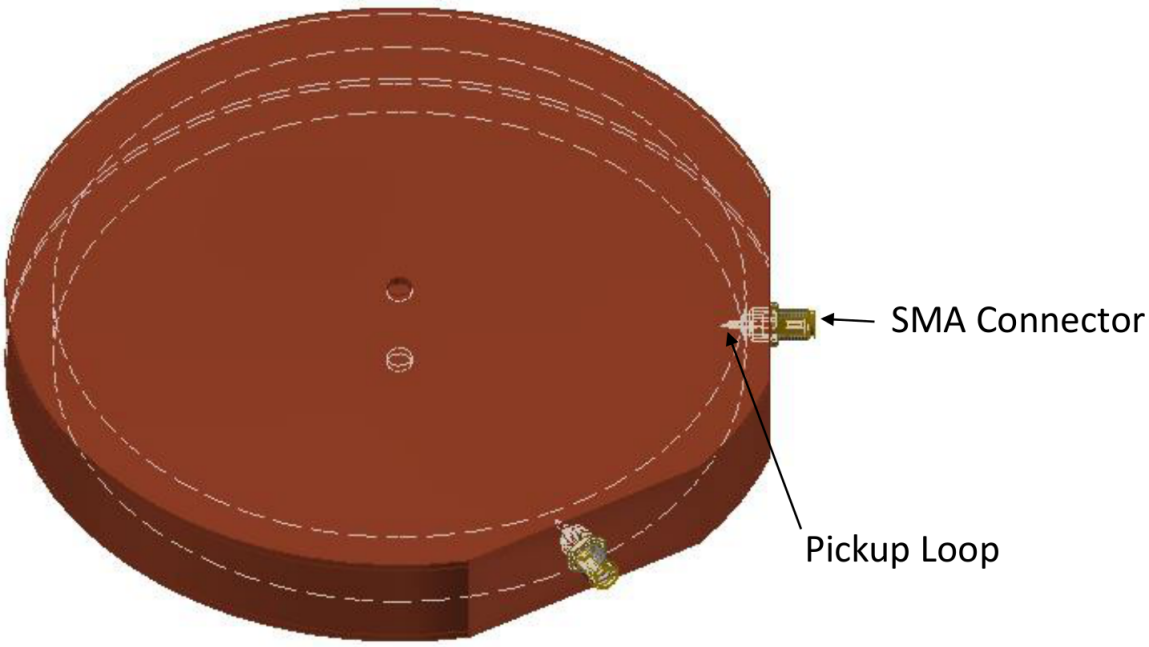

Figure 6.3: Cylindrical cavity. The SMA connectors connected to loops to ground inside the cavity, coupling was adjusted by rotating the connectors. The connections were identical and could be used for signal or for cavity drive. The electron beam went through the holes along the axis of the cylinder.

6.2.2 Ring Resonator

The cylindrical cavity has a substantial problem: in order to allow for a 10 cm aperture, the cavity would need to be quite large. Aside from the difficulty of installing such a large cavity inside a magnet in the beam line, this would also result in a large cavity capacitance, reducing the change in voltage for a passing electron. A different type of resonator was constructed where a ring suspended by coils acts as a pickup (see figure 6.4). The resonant frequency was determined by the capacitance of the ring to the resonator body, and the inductance of the coils. Pickup coils on the end of long coaxial tubes allowed coupling to the magnetic field of the coils, and the coupling could be adjusted by rotating the pickups.

The energy exchange with the resonator was determined using Comsol simulation to determine the electric field. The root-mean-square energy exchange was determined by averaging over all electron trajectories and pitch angles of the electron to the magnetic field that would be expected were it installed in the KATRIN beamline, as well as all cavity phases when the electron entered. The total field energy and energy exchange with a passing electron was used to determine what the change in voltage on the ring would be, which was independent of excitation as was shown in section 6.2. The can geometry was fixed by available space to install the resonator, and the ring size by the diameter of the beam line. The resonant frequency was chosen to maximize the RMS energy exchange. The energy exchange was not highly sensitive to oscillation frequency, so the nearest quiet band at 151.5 MHz was chosen. The cavity was loaded to attain a loaded quality of 151, so the signal would have a decay time of 160 ns. For an RMS energy exchange of 1 eV a cavity voltage of 2.3 V was calculated. The cavity capacitance was estimated at 6.7 pF. A passing electron was expected to produce a voltage change of 10 nV, while the thermal fluctuations at 50 K would be 14 μV.

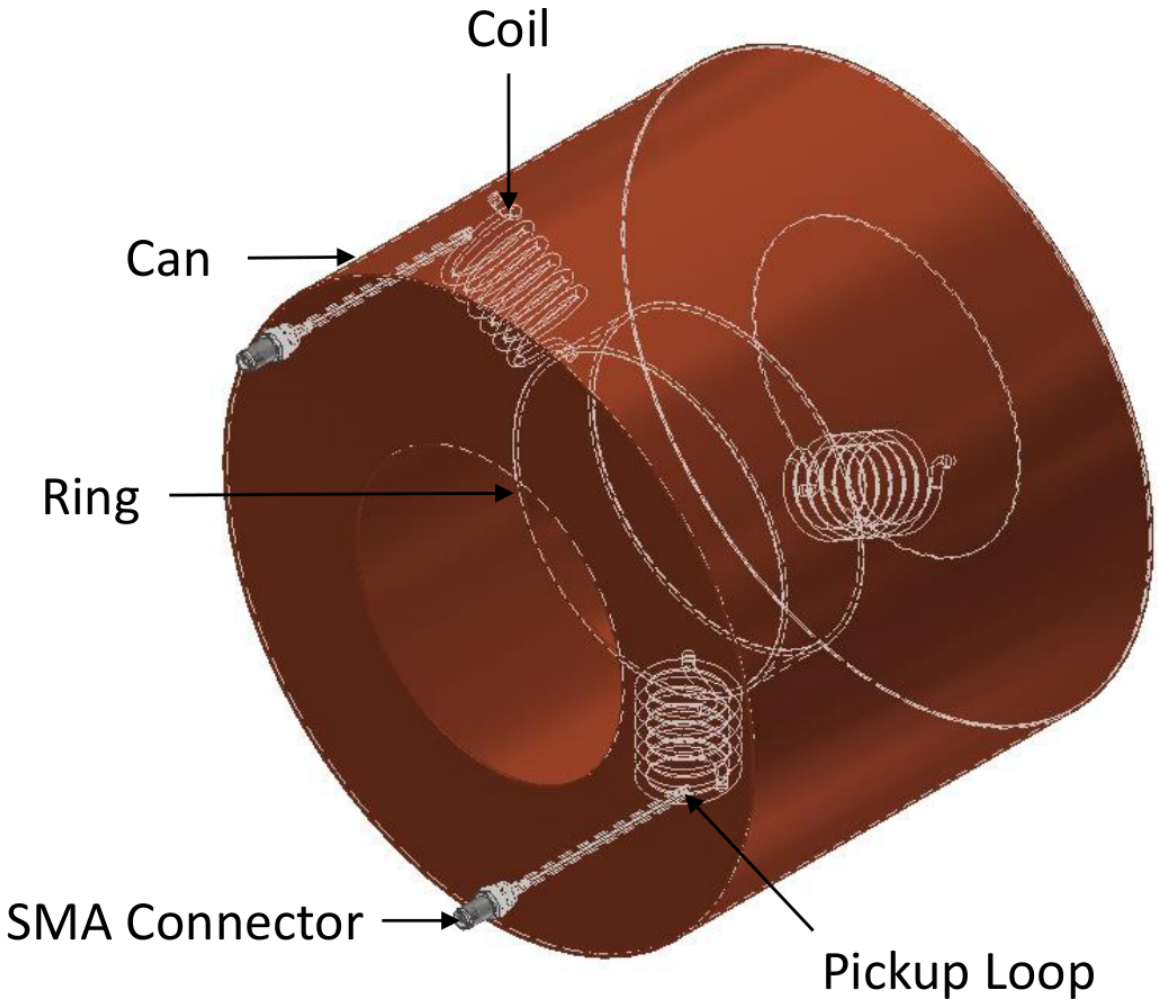

Figure 6.4: Ring resonator. The loop inside was connected to the resonator outer can by three coils, forming an LC resonator with the loop to can capacitance and the coil inductance. Loops on the end of coaxial tubes coupled to the inductor field, and the coupling is adjusted by rotating the SMA connectors. The connections are identical and can be used for signal or resonator drive.

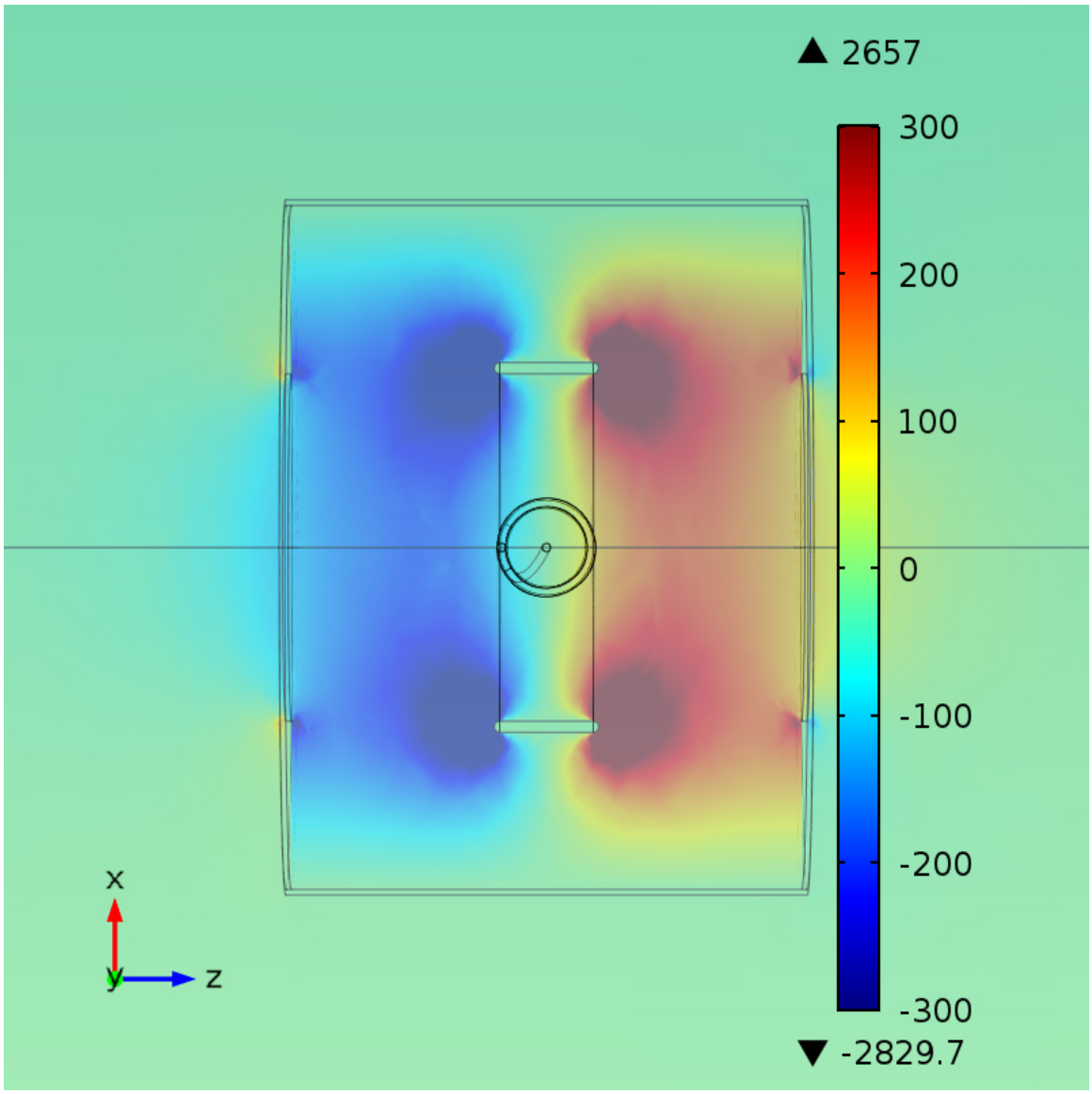

Figure 6.5: Ring resonator electric field, axial component. The field oscillates in time and is shown for and arbitrary instant. The scale is arbitrary, the energy exchanged and stored energy were scaled using the maximum voltage on the ring for calculations.

6.2.3 Energy Exchange with Cavity for Any Mode

Previously only the lowest order mode was considered. But, the electron can exchange energy with higher-order cavity modes as well, allowing a single cavity to act as multiple detectors. Because the energy exchanged with each mode will have a different dependence on electron speed, this could be used to determine the electron pitch angle. As in the previous section, this energy exchange is calculated for each cavity mode by integrating the electric field along the cylinder axis. Since there is no axial component of electric field for the transverse electric modes, only the transverse magnetic modes are needed. The axial component of electric field is given by:

$$E_z(r, z, \theta, t) = E_0 J_m(k_n r) Cos(m\theta) Cos(k_l z) \cos(\omega t) \tag{6.28}$$

The axial wave number is:

$$k_l = \frac{\pi l}{d} \tag{6.29}$$

where d is the length of the cavity and extends from $z = 0$ to $z = d$. The radial wave number is:

$$k_n = \frac{j_{mn}}{a} \tag{6.30}$$

where a is the radius of the cavity. The angular frequency of cavity oscillation is:

$$\omega = c\sqrt{k_n^2 + k_l^2} \tag{6.31}$$

where c is the speed of light, J_m is the m^{th} Bessel function of the first kind, and j_{mn} is the n^{th} zero of the m^{th} Bessel function.

As $J_m(0) = 0$ for any value of m other than 0, only the $m = 0$ modes will exchange energy with the electron.

$$\triangle W = e\int_0^d E_z(0,z,\theta,\frac{z}{v}+t_0)dz \tag{6.32}$$

The change in stored energy can also be related to the change in the electric field in the cavity. For the TM_{0nl} modes the axial electric field is:

$$E_z(r,z,\theta,t) = E_0 J_0(k_n r)Cos(k_l z)\cos(\omega t) \tag{6.33}$$

The radial electric field is:

$$E_r(r,z,\theta,t) = E_0\frac{-k_l}{k_n}J_1(k_n r)Cos(k_l z)\cos(\omega t) \tag{6.34}$$

And the radial magnetic field is:

$$H_r(r,z,\theta,t) = E_0\frac{-\epsilon_0\omega}{k_n}J_1(k_n r)Cos(k_l z)\sin(\omega t) \tag{6.35}$$

For $m = 0$ the azimuthal electric and magnetic field are zero ($E_\theta = H_\theta = 0$), and for transverse magnetic (TM) modes $H_z = 0$. The stored energy is:

$$W = \iiint \frac{\epsilon_0 E\cdot E}{2} + \frac{\mu_0 H\cdot H}{2} \tag{6.36}$$

$$W = \begin{cases} \epsilon_0 E_0^2 \frac{\pi a^2 d\, J_1(j_{0n})^2}{2} & l = 0 \\ \epsilon_0 E_0^2 \frac{\pi a^2\, J_1(j_{0n})^2(\pi^2 a^2 l^2 + d^2\, j_{0n}^2)}{4d\, j_{0n}^2} & l > 0 \end{cases} \tag{6.37}$$

where ϵ_0 and μ_0 are the is the permittivity and permeability of free space. $l = 0$ is a special case, where there are no axial nodes in the cavity. The averaging of a cosine squared function in the field energy causes all other nodes to have half the energy compared to a mode where $l = 0$. With no nodes the maximum energy exchange occurs when the electron travels through the cavity quickly compared to the cavity oscillation period, and the maximum energy exchanged is $eE_0 d$. Treating the cavity like a capacitor, where the voltage on the capacitor is $E_0 d$, and solving $W = \frac{1}{2}CV^2$ for C gives the effective cavity capacitance in

equation 6.19. Defining cavity voltage as the integral of the electric field along the axis when the field is maximum makes sense for $l = 0$, but for other values of l this will result in 0 unless the time dependence is included. Still, as it is directly proportional to E_0, and therefore to the signal any probe will see, it is a good definition to use.

$$V = E_0 d \tag{6.38}$$

Using this relation forces the cavity capacitance, using the formula $W = \frac{1}{2}CV^2$, to:

$$C = \begin{cases} \frac{\epsilon_0 \pi a^2 J_1(j_{0n})^2}{d} & l = 0 \\ \frac{\epsilon_0 \pi a^2 J_1(j_{0n})^2 (\pi^2 a^2 l^2 + d^2 j_{0n}^2)}{2 d^3 j_{0n}^2} & l > 0 \end{cases} \tag{6.39}$$

To get an estimate of how the performance of a cavity might work for an electron tagger accessing many modes, we first determine the expected energy exchange with any mode. Assuming a random cavity phase (ϕ) when the electron arrives:

$$\Delta W\left(v, \phi\right) = eE_0 \int_0^d \cos(k_l z) \cos(\omega \frac{z}{v} + \phi) dz \tag{6.40}$$

where v is the electron's speed. The RMS energy exchange is calculated by integrating over all phase angles.

$$\left\langle \Delta W\left(v\right)^2 \right\rangle = \frac{1}{2\pi} \int_0^{2\pi} \left(\triangle W\left(v, \phi\right)\right)^2 d\phi \tag{6.41}$$

$$\left\langle \Delta W\left(v\right)^2 \right\rangle = \left(e\,V\right)^2 \left(\frac{s}{\pi l}\right)^2 \frac{1 - \left(-1\right)^l \cos\left(\frac{\pi l}{s}\right)}{\left(1 - s^2\right)^2} \tag{6.42}$$

where $s = {}^{v\,k_l}/_{\omega}$. Values for RMS energy exchange for different electron speed and values for l are shown in figure 6.6. The expected energy exchange can be reasonably approximated by assuming it takes the value $\frac{1}{2}\left\langle \Delta U \left(\frac{\omega}{k_l}\right)^2 \right\rangle$ over an interval between $\omega = \frac{v}{d}\frac{2\pi l^2}{2l \pm \pi}$. This gives a frequency range of:

$$\Delta v = \frac{d\omega}{l^2} = \frac{\pi c\, d}{l^2} \sqrt{\frac{n^2}{a^2} + \frac{l^2}{d^2}} \tag{6.43}$$

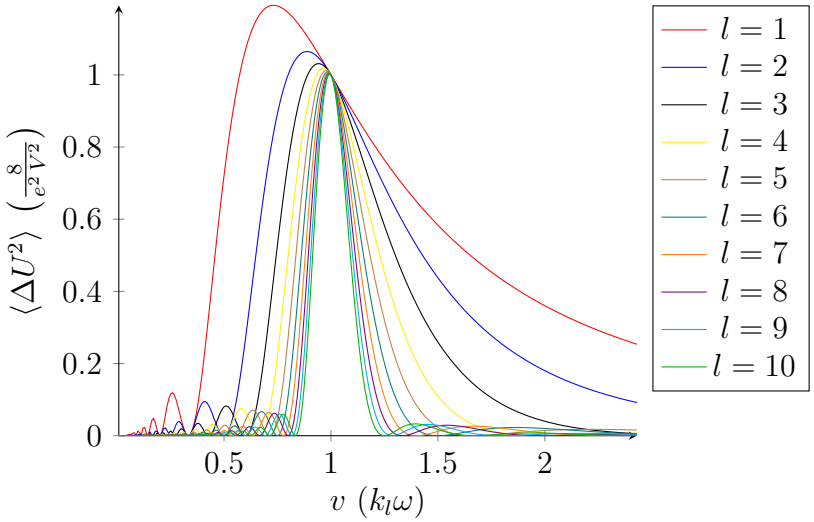

Figure 6.6: Mean cavity energy exchange squared. Normalized in both particle speed and cavity voltage.

Note that the case of $l = 0$ is not considered, as it is divergent. Using many high-order modes will not contribute much signal, as the useful range of speed rapidly drops. Select modes could be helpful in some cases, but this is especially problematic for KATRIN where the electron varies in pitch angle so a range of speed is expected. When $s = 1$ the charge traverses the cavity such that it crosses nodes every half period. This is approximately where the maximum energy is exchanged for large l, the maximum occurs at slower speed for small values of l, but it still makes a good approximation of the maximum energy exchange:

$$\left\langle \Delta W \left(\omega / k_l\right)^2 \right\rangle = \frac{e^2 V^2}{8} \tag{6.44}$$

From equation 6.24 the expected signal of a mode is:

$$\left\langle \Delta V \left(v\right)^2 \right\rangle = \frac{\left\langle \Delta W \left(v\right)^2 \right\rangle}{C^2 V^2} \tag{6.45}$$

$$\left\langle \Delta V \left(\omega / k_l\right)^2 \right\rangle = \frac{e^2}{8C^2} \tag{6.46}$$

and the expected noise is:

$$\left\langle \Delta V_{noise}^2 \right\rangle = \frac{k_b T}{C} \tag{6.47}$$

The low capacitance modes have the best signal-to-noise ratio, making them most desirable.

$$J_1 \left(j_{0n}\right)^2 \approx \frac{2}{\pi^2 n} \tag{6.48}$$

$$j_{0n} \approx \pi n \tag{6.49}$$

$$C \approx \frac{\epsilon_0 a^2 \left(a^2 l^2 + d^2 n^2\right)}{\pi d^3 n^3} \tag{6.50}$$

Not only are large values of l undesirable due to the narrow response range for varying speed, but they also have a higher capacitance. This appears to favor large values for n, to keep the capacitance down, however it actually increases capacitance due to the radius needing to be large. Assuming $l = 1$ and $n \gg 1$ the speed for a node is:

$$v_{n \gg l=1} \approx c \frac{d}{a} n \tag{6.51}$$

For a fixed electron speed and cavity length the ratio n/a is fixed, so as n increases a^2/n increases, and the capacitance grows proportional to n. The response range is:

$$\Delta v_{n \gg l=1} \approx \pi c \frac{d}{a} n \tag{6.52}$$

Only a couple of nodes can ever be expected to have suitable overlap in response. Also, for a fixed speed and cavity length the ratio n/a is also fixed. Thus the capacitance can actually be expected to grow proportional to n due to the increase in cavity size. This makes readout of multiple cavity modes unlikely to provide better overall performance than simply reading out the TM_{101} mode. However, reading out multiple modes could still be useful for determining pitch angle — using the large speed dependence in the response of the higher order modes.

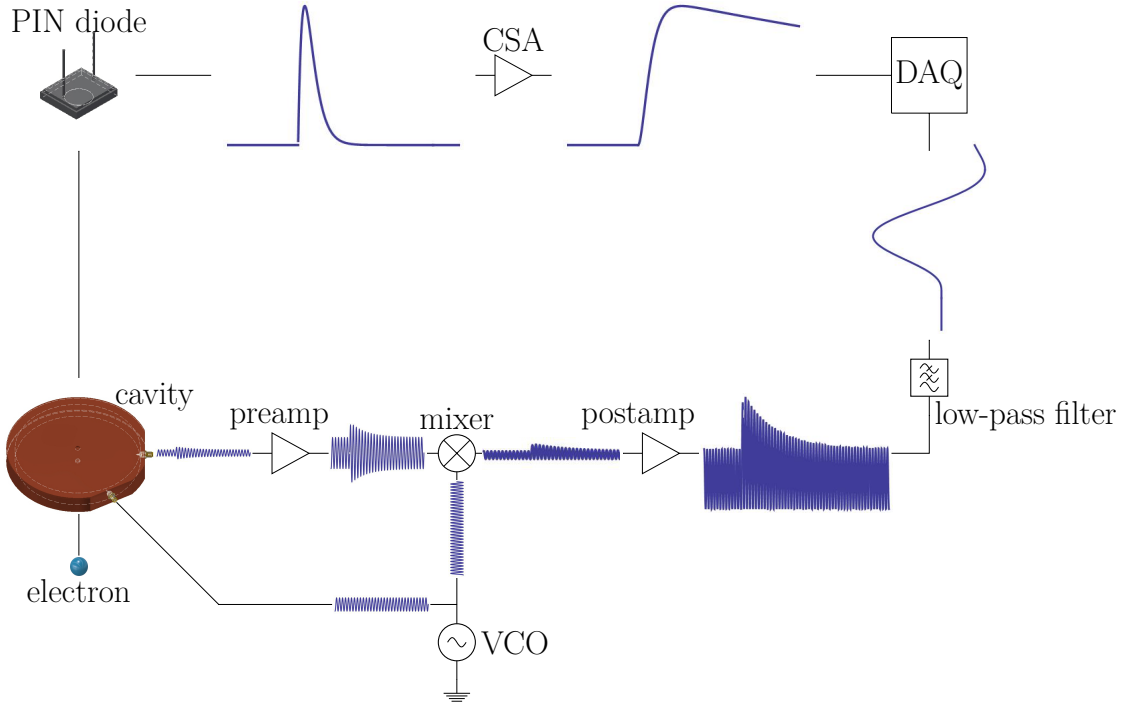

Figure 6.7: Simplified cavity readout electronics. The actual electronics consisted of three preamplifiers, and a series of two postamplifiers each followed by a low-pass filter.

6.2.4 Readout Electronics

The readout system used for both cavities is shown in figure 6.7 and is similar to an AM radio. The cavity was driven by a Voltage Controlled Oscillator (VCO), which also drove the mixer. A passing electron would change the amplitude of the cavity oscillations, so that the carrier was removed and the change in carrier amplitude appeared as DC. The higher order harmonics of the carrier were removed by low-pass filters and the DC signal component was amplified, and digitized by an oscilloscope connected to a Data AcQuisition (DAQ) computer. A pin diode connected to a Charge-Sensitive Amplifier (CSA) was also connected to the same oscilloscope, and used as a trigger. Thus the cavity signal timing was known even if the signal was too small to see.

As the cavity was just as likely to give the electron energy as take it, the average of

the signal was zero. It was attempted to draw the signal out of the noise by averaging the Root-Mean-Square (RMS) of many signals. Since the RMS was used for each signal, this means the noise was unipolar as well as the signal. So the noise level doesn't approach 0, but it does settle down to a constant background, which could allow a small signal to appear above it. However, since it's the RMS of the noise the convergence doesn't go as the square root of times, but rather the fourth root! Even after millions of events no signal became visible.

The carrier increased energy exchange with the electron, but, this didn't actually improve the signal strength. After mixing, only the change in the DC signal remained. This corresponds to the voltage change in the carrier, and is independent of carrier power. Robinson [59, p. 11] claimed that the useful signal is the voltage, and not the energy, giving a formula for the least-discernible change in signal power of:

$$P_{min} = k_b T \Delta f \tag{6.53}$$

$$\delta V = \sqrt{4R\, k_b\, T\, \Delta f} \tag{6.54}$$

$$\delta P = 2\sqrt{P\, k_b\, T\, \Delta f} \tag{6.55}$$

where k_b is Boltzmann's constant, T is temperature, R is resistance of the signal source, and V is signal source voltage. As power is proportional to energy, and the change in energy is proportional to the electric field while the stored energy is proportional to the field squared, this would suggest that exciting the cavity was pointless. Indeed, no readout method was discovered that would take advantage of the larger energy exchange due to exciting the cavity. It does leave narrowing the bandwidth (Δf) as a means of discerning the signal from the noise, raising the possibility of using a high quality resonator.

Some cavity excitation may still be useful to ensure the energy change in the cavity won't even be a single quanta of energy. For an oscillator, the energy between quantum excitation

states is:

$$\Delta E = \hbar\omega \tag{6.56}$$

where $\hbar$ is Planck's constant divided by 2π and ω is the angular frequency of the resonator. For the 1660 MHz cavity ΔE is $1.1 \cdot 10^{-24}$ J. If the cavity were unexcited, so the voltage went from 0 to 49 nV, that would only be $2.4 \cdot 10^{-27}$ J or 0.002 quanta of excitation. To get an expected energy exchange of at least one quantum only requires a cavity voltage of 11 μV, which is the expected thermal excitation for 9 K. Since it is desirable to keep the cavity as cold as possible, some sort of cavity excitation may be necessary just to ensure at least one quantum of energy is exchanged, even if the readout is only sensitive to a change in voltage. A readout sensitive to a phase change could possibly avoid this limit.

6.2.4.1 Varactor Diode Oscillator

One could construct a resonant circuit with an element that changes the circuit frequency as the electron passes, like a voltage-controlled oscillator using a varactor diode. For a resonator using a varactor diode the phase shift for an applied voltage is:

$$\Delta\phi = \frac{\omega}{2C}\frac{dC}{dV}\int \Delta V dt \tag{6.57}$$

where ω is the oscillator frequency, C is the resonator capacitance, V is the varactor voltage, and ΔV is the change in V due to the passing electron. However, the same problems arise from voltage noise, as any element that produces a phase shift for a change in voltage due to a passing electron will also produce a phase shift for any other voltage source. So it is still a problem of detecting a small voltage change in a large voltage noise.

6.2.5 Loop Pickup

After the cavity and ring resonator experience, and the realization that increasing energy exchange didn't actually help, optimizing the pickup was explored.

From simulations with the ring resonator and shortening the length of the ring, it was determined that the optimum ring was a ring that wasn't extended. A resonant circuit could be constructed using the ring, an inductor, and a capacitor with a feedback amplifier:

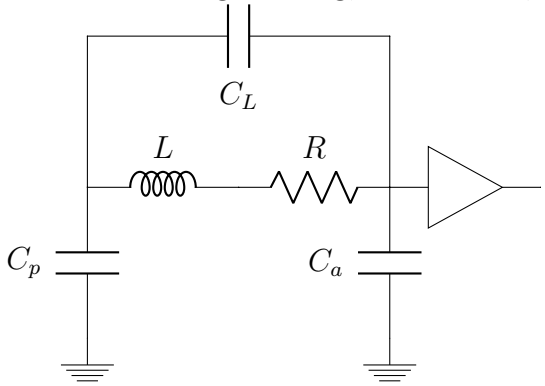

6.2.5.1 Signal

Circuit Response This circuit can be viewed as a series RLC resonant circuit with an effective capacitance. The homogeneous solution to this circuit is known to be a decaying sine and cosine function. For an impulse response initial current through the inductor is zero, therefore the cosine term must be zero.

$$i_L(t) = A\sin(\omega t)\, e^{-\lambda t} \tag{6.58}$$

$$\lambda = \frac{R}{2L} \tag{6.59}$$

$$\omega^2 = \frac{1}{LC_{eff}} - \lambda^2 \tag{6.60}$$

$$C_{eff} = C_L + \frac{C_p C_a}{C_p + C_a} \tag{6.61}$$

We assume a charge q is placed on the probe and the circuit is left to decay until no current flows. The initial charge applied to the effective capacitance to ground seen by the probe gives the initial probe voltage. The initial amplifier input voltage can be determined

from the initial probe voltage and the capacitive voltage divider formed by C_L and C_a. The final voltage across C_L must be zero as there is no current flow across the inductor and resistor after the resonant circuit has completely decayed away, and the charge q is now shared between C_p and C_a.

$$C_{peff} = C_p + \frac{C_L C_a}{C_L + C_a} \tag{6.62}$$

$$V_p(0) = \frac{q}{C_{peff}} \tag{6.63}$$

$$V_a(0) = V_p(0) \frac{C_L}{C_L + C_a} \tag{6.64}$$

$$V_p(\infty) = V_a(\infty) = \frac{q}{C_p + C_a} \tag{6.65}$$

The capacitors start out in a stable condition and the inductor is the sole source of the charging current. Thus, the voltage on the probe and amplifier must be proportional to the integral of the inductor current, with constants determined by the boundary conditions.

$$V(t) = (V(0) - V(\infty)) \left(\cos(\omega t) + \frac{\lambda}{\omega} \sin(\omega t) \right) e^{-\lambda t} + V(\infty) \tag{6.66}$$

The amplitude of the oscillations at the amplifier input is the term of most interest, as the signal amplitude is directly proportional to this term, and the constant term is of no interest:

$$V_a(0) - V_a(\infty) = \frac{-q C_p C_a}{(C_a + C_p)(C_L C_p + C_L C_a + C_p C_a)} \tag{6.67}$$

Using the response to an impulse as the kernel, the circuit response to an arbitrary input can be determined.

$$G_a(t') = \frac{-C_p C_a}{(C_a + C_p)(C_L C_p + C_L C_a + C_p C_a)} \left(\cos(\omega t') + \frac{\lambda}{\omega} \sin(\omega t') \right) e^{-\lambda t'} + \frac{1}{C_p + C_a} \tag{6.68}$$

$$V_a(t) = \int^{t} G_a(t - t')\, i(t')\, dt' \tag{6.69}$$

Where $i(t')$ is the applied current.

Applied Signal For a charged particle with a charge e, traveling through a toroid with a major radius R and minor radius r, traveling along the axis of the toroid at a speed v, the charge on the ring can be closely approximated by:

$$Q_i(t) = \frac{eC_p}{4\pi\epsilon_0 R} \left(1 + \frac{r}{2R}\right) \frac{1}{\sqrt{1 + \left(\frac{vt}{R}\right)^2}} \tag{6.70}$$

This may initially look like it favors a large capacitance, but, the capacitance is proportional to R, and the response is inversely proportional to R. Thus the induced charge depends only on the geometry and is not improved by using a larger probe with a larger capacitance. The capacitance of a toroid is given by:

$$16\epsilon_0 \sqrt{A^2 - r^2} \sum_{n=0}^{\infty} \frac{1}{1 + \delta_{n,0}} \frac{Q_n\left(\frac{A}{r}\right)}{P_n\left(\frac{A}{r}\right)} \tag{6.71}$$

where A is the difference between the major radius and minor radius, P_n are the Legendre functions, Q_n are the Legendre functions of the second kind, and the coefficient weighs the $n = 0$ function by half and doesn't affect the others.

The equipotentials for a ring of charge and a point charge do not quite form toroids, but, for a charge lying on the axis of the toroid they do come very close. These equipotentials were numerically determined for a few ratios of the ring diameter and wire diameter. The resulting ring charge was compared to a simple model of the charge on a toroid. The toroid charge was assumed to be that required to charge up the toroid capacitance to a voltage

equal to the voltage due to the point charge, at the center of the wire of the toroid. The small correction constant $\left(1+\frac{r}{2R}\right)$ resulted in an approximation that, for a minor radius one tenth the major radius, was accurate to 1% in the center of the toroid. However, this approximation does result in around 5% error at long distances. As the electric field far from the toroid is greatly reduced it is more important to be accurate close to the toroid.

Optimum response The optimum frequency for this response can be found by maximizing the integral of the applied current with the kernel function for an impulse. As long as the circuit is of high quality, the sine term in the kernel can be ignored. The constant term representing the DC offset has no frequency dependence, nor is it of interest when looking for a signal at the circuit resonance, and can be dropped.

$$i\left(t'\right)=\frac{d}{dt}Q_i\left(t\right)=-\frac{eC_p}{4\pi\epsilon_0 R}\left(1+\frac{r}{2R}\right)\frac{v^2}{R^2}\frac{t'}{\left(1+\left(\frac{vt'}{R}\right)^2\right)^{\frac{3}{2}}} \tag{6.72}$$

$$G\left(t-t'\right)\approx\frac{-C_pC_a}{\left(C_a+C_p\right)\left(C_LC_p+C_LC_a+C_pC_a\right)}\cos\left(\omega\left(t-t'\right)\right)\Theta(t-t') \tag{6.73}$$

where $\Theta\left(t-t'\right)$ is the Heaviside function. We want to maximize, for some arbitrarily large t:

$$\int_{-\infty}^{t} i\left(t'\right)G\left(t-t'\right)dt' \tag{6.74}$$

$$\cos\left(\omega\left(t-t'\right)\right)=\cos\left(\omega t\right)\cos\left(\omega t'\right)+\sin\left(\omega t\right)\sin\left(\omega t'\right) \tag{6.75}$$

The ωt terms oscillate in time, but don't contribute to the overall amplitude of the signal just the phase at a specific time, and are thus of no interest. As the current is an odd function, the cosine term will vanish after the electron passes (that this happens for signal, but doesn't happen for shot noise, becomes a useful feature in section 6.2.6). Thus the maximum response can be determined solely from the sine term, and we can maximize the response by maximizing:

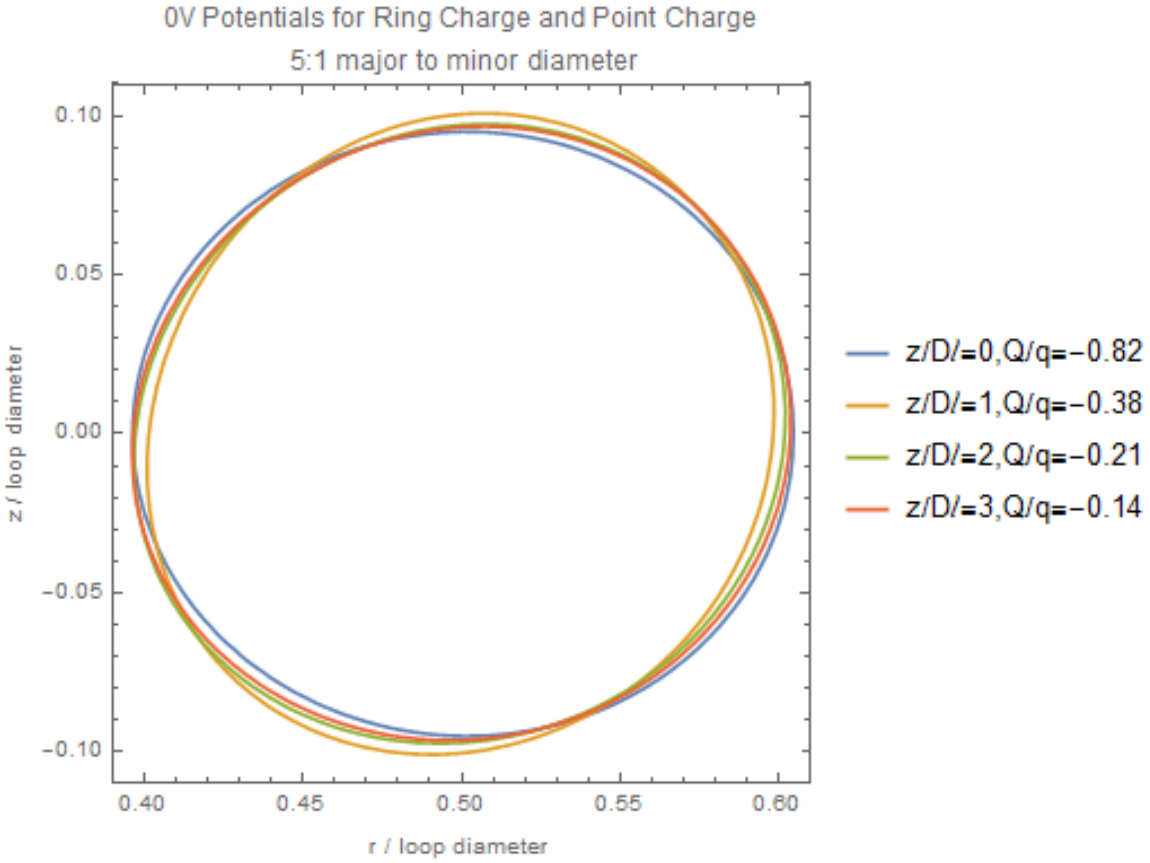
0V Potentials for Ring Charge and Point Charge
5:1 major to minor diameter
z / loop diameter
r / loop diameter
0.10
0.05
0.00
−0.05
−0.10
0.40
0.45
0.50
0.55
0.60
z/D/=0,Q/q=−0.82
z/D/=1,Q/q=−0.38
z/D/=2,Q/q=−0.21
z/D/=3,Q/q=−0.14

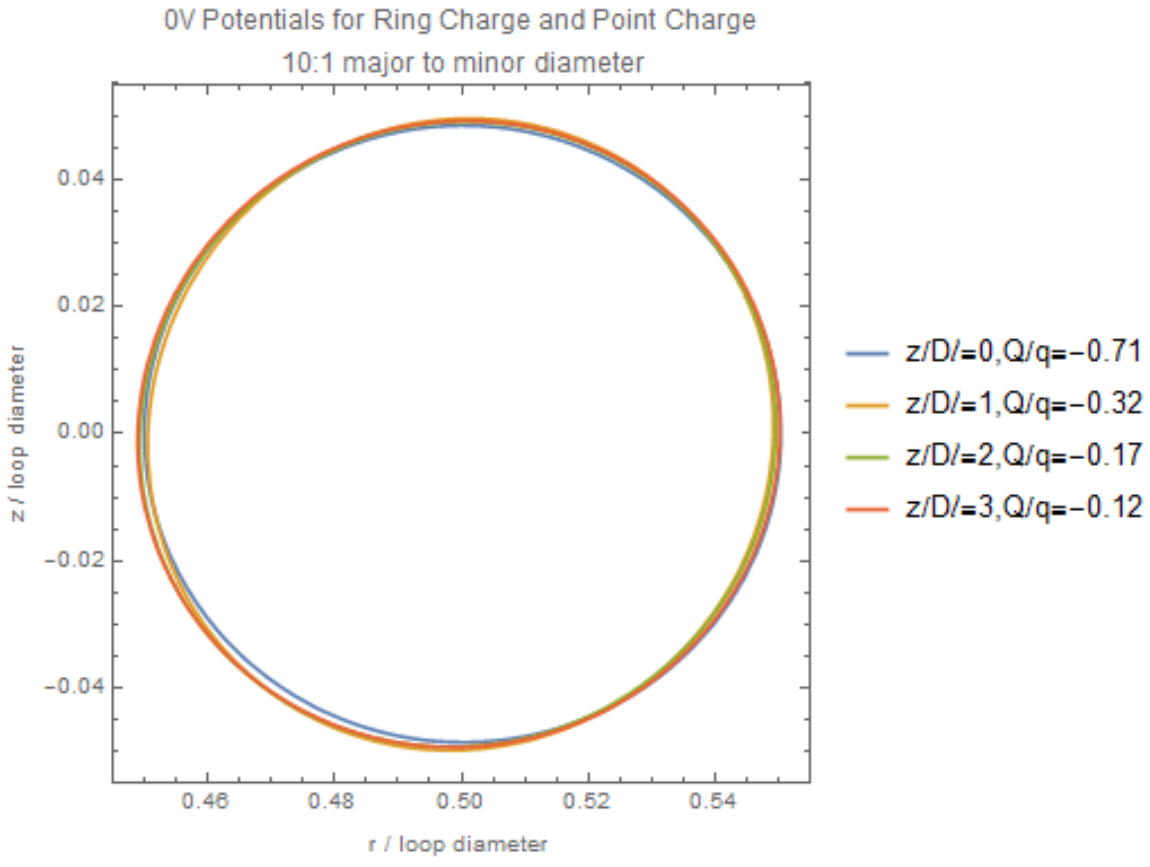
0V Potentials for Ring Charge and Point Charge
10:1 major to minor diameter
z / loop diameter
r / loop diameter
0.04
0.02
0.00
−0.02
−0.04
0.46
0.48
0.50
0.52
0.54
z/D/=0,Q/q=−0.71
z/D/=1,Q/q=−0.32
z/D/=2,Q/q=−0.17
z/D/=3,Q/q=−0.12

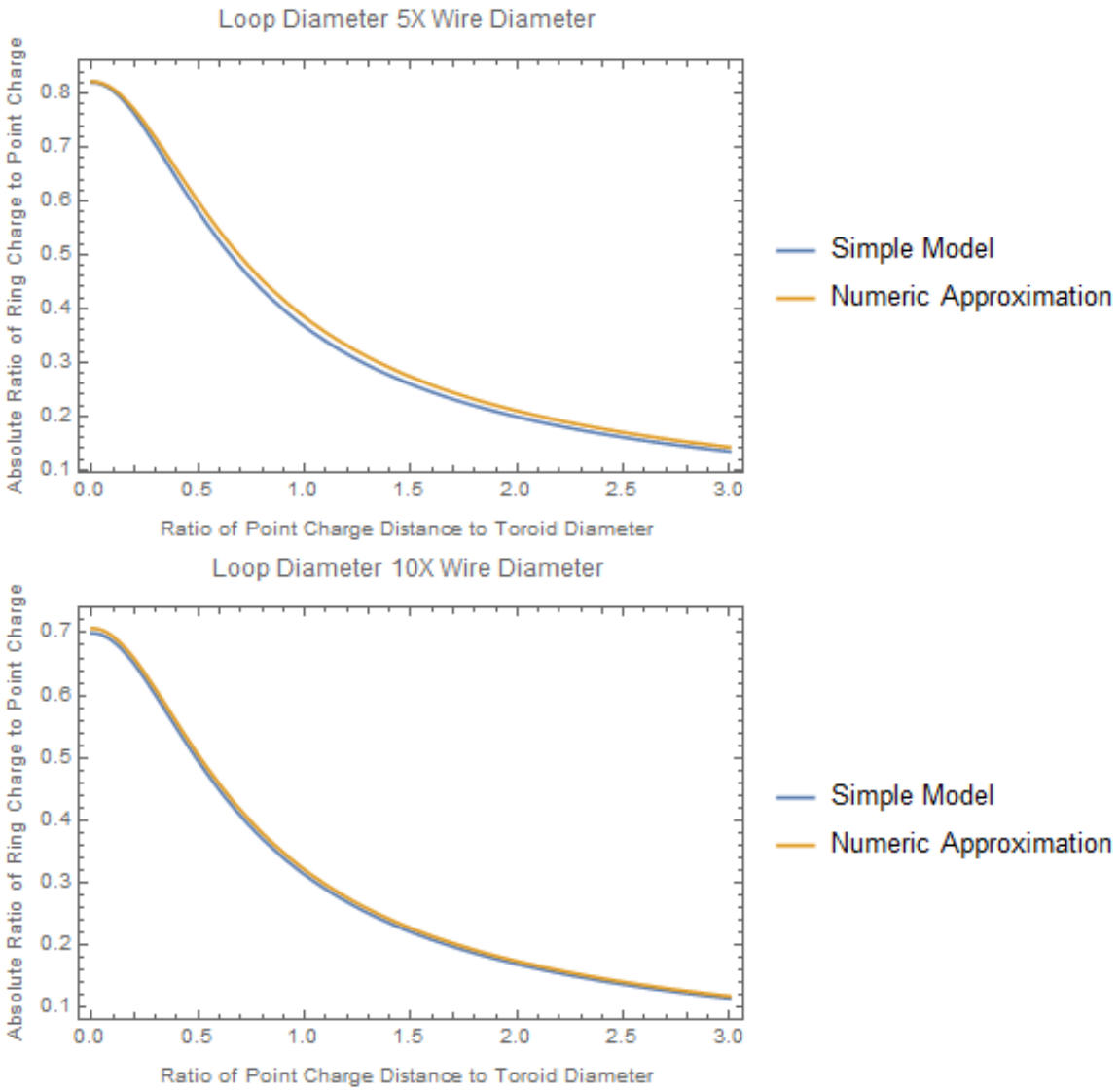

Figure 6.9: Comparison of image charge calculated by simple model to best fit approximation using ring of charge and point charge.

$$k \int_{-\infty}^{\infty} \frac{v^2}{R^2} \frac{t' \sin(\omega t')}{\left(1 + \left(\frac{vt'}{R}\right)^2\right)^{\frac{3}{2}}} dt = 2k \left(\frac{\omega R}{v}\right) K_0 \left(\frac{\omega R}{v}\right) \tag{6.76}$$

$$k = \frac{C_p}{4\pi\epsilon_0 R} \left(1 + \frac{r}{2R}\right) \frac{e}{C} \tag{6.77}$$

$$C = \frac{(C_p + C_a)(C_L C_p + C_L C_a + C_p C_a)}{C_p C_a} \tag{6.78}$$

Where K_0 is the zeroth modified Bessel function of the second kind. When $\omega = 0.595 \frac{v}{R}$ equation 6.76 reaches its maximum value of 0.933 k, assuming the radius and particle speed are given and the response is maximized by changing frequency.[2] For a reasonable ratio of wire diameter to loop diameter and a loop diameter matched to the particle speed this gives a signal response of:

$$V_s = \frac{\eta e}{C} \tag{6.79}$$

the relative response (η) depends on the ratio of the toroid major radius to minor radius. It is likely to be around 0.5, see figure 6.10. While a larger ratio may appear to be favorable from figure 6.10, as it gives a larger η, the effective capacitance (C) grows due to the change in probe capacitance (C_p), favoring thinner loops with a lower capacitance.

---

[2]For a loop diameter of 10 cm and a speed of 0.2 c, the optimum frequency comes out to 114 MHz. Fortunately, the response isn't strongly peaked. There is a radio quiet band at 150 MHz. Using 150 MHz reduces the response from 0.933 to 0.908.

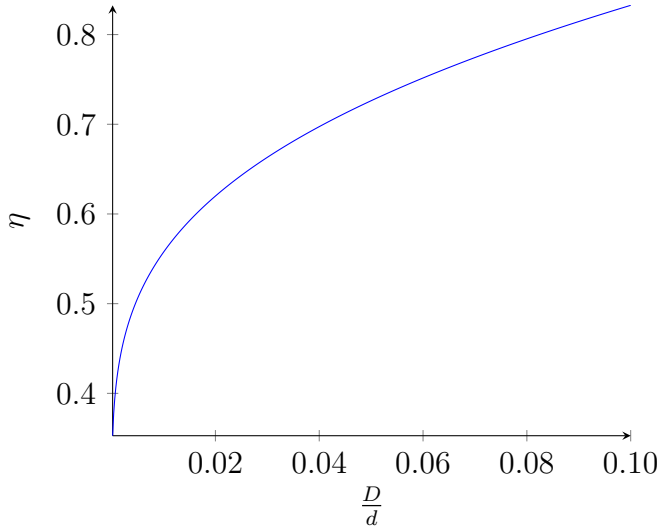

Figure 6.10: Relative response of loop pickup (η), when loop diameter and oscillation frequency is optimized for speed of passing charge, for ratio of wire diameter (d) to loop diameter (D).

6.2.5.2 Noise

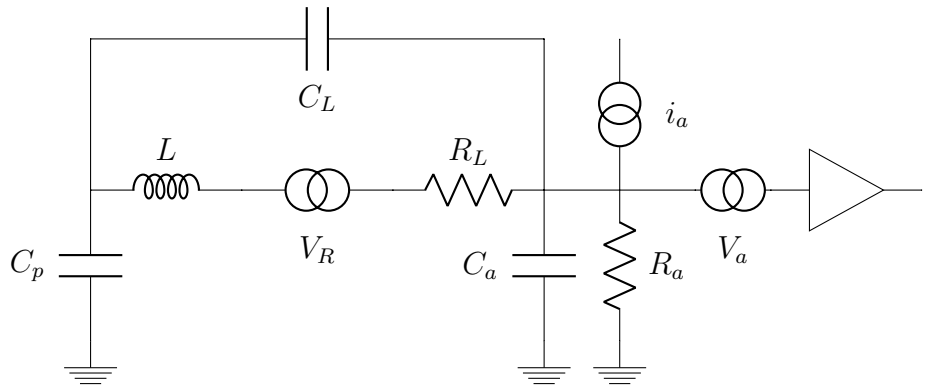

The resistor thermal voltage noise sees an effective series impedance:

$$Z_{VR} = (Z_1 \parallel Z_2) + Z_3 \tag{6.80}$$

$$Z_a = \frac{1}{i\omega C_a} \parallel R_a \tag{6.81}$$

$$Z_1 = Z_a + \frac{1}{i\omega C_p} \tag{6.82}$$

$$Z_2 = \frac{1}{i\omega C_L} \tag{6.83}$$

$$Z_3 = i\omega L + R_L \tag{6.84}$$

where the parallel operator $a \parallel b = \frac{a \cdot b}{a+b}$. The resistor noise voltage (V_R) develops a current though this impedance, which is split by the two current paths, and develops a noise voltage from the current on the amplifier input:.

$$V_{n,R} = \frac{V_R}{Z_{VR}} \frac{Z_2}{Z_1 + Z_2} Z_a \tag{6.85}$$

Substitute in the Johnson-Nyquist formula for voltage noise on a resistor, the noise contribution for the resonator resistance is:

$$V_{n,R}^2 = 4k_b T\, R_L \left(\frac{Z_2}{Z_1 + Z_2} \frac{Z_a}{Z_{VR}} \right)^2 \tag{6.86}$$

The series voltage noise from the amplifier input is developed on R_a, and since R_a goes right to ground this is trivially the voltage applied to the amplifier input. The current noise sees three current paths, and the current is split among them. The current of concern is through the path with impedance Z_1, and develops a noise voltage across Z_a. This results in a voltage noise at the amplifier input of:

$$V_{n,i}^2 = 2i_a e \left(Z_a \frac{Z_3 Z_2}{Z_1 Z_2 + Z_2 Z_3 + Z_1 Z_3} \right)^2 \tag{6.87}$$

where e is the charge on an electron and i_a is the amplifier leakage current. The amplifier voltage noise, the resonator voltage noise, and the amplifier current noise, add in quadrature to a total noise seen at the amplifier input. An example noise calculation is done using a new readout method in section 6.2.6.

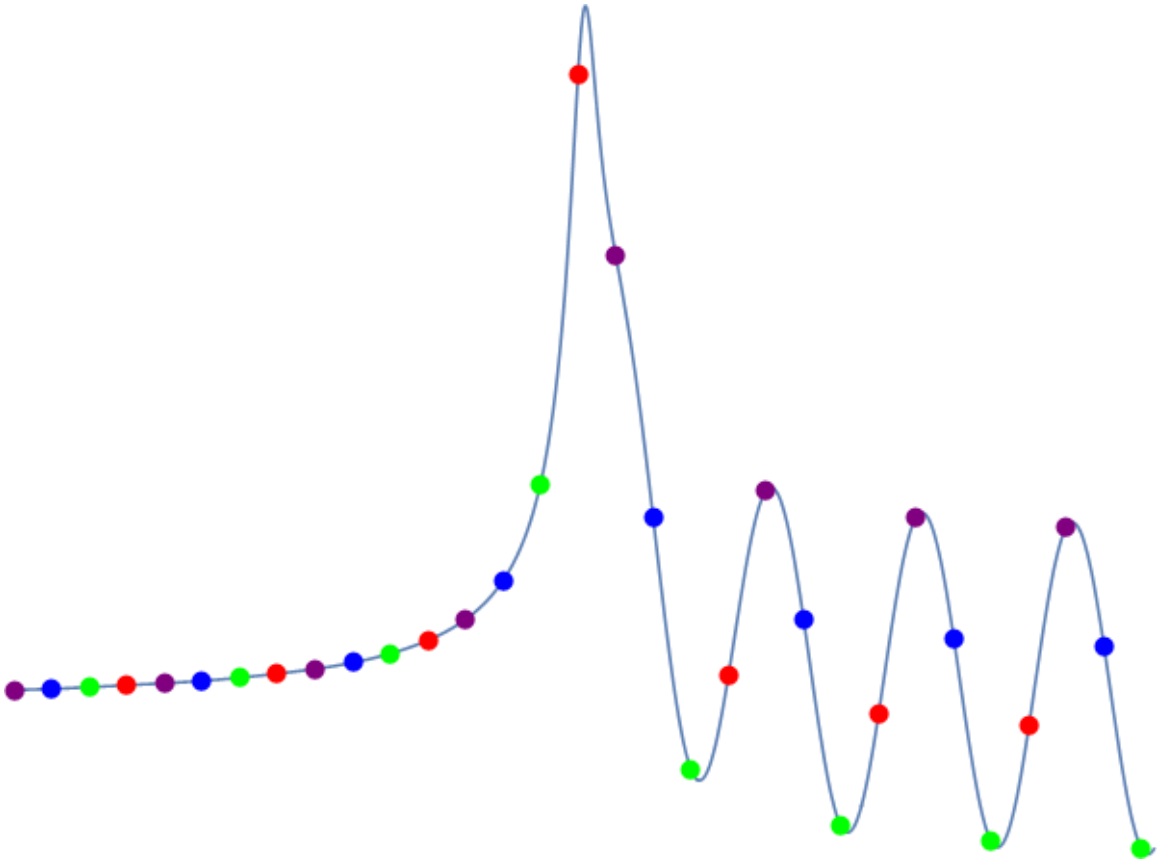

Figure 6.11: Expected signal and readout sample points. Each color point represents where the points for one of the sums could be taken, depending on the relative phase of the signal and sampling.

6.2.6 Improved Readout Technique

The noise amplitude in the resonant circuit is much larger than the signal, but for a high-quality resonator it varies very slowly. A filtering scheme is proposed where signal samples quarter-periods apart are combined such that the output would be highly sensitive to sudden changes, but insensitive to slow changes. Assume the signal is sampled every quarter period. For sums are calculated, each sum containing samples one period apart and the sums are spaced a quarter period apart. By looking at the differences in sums half a period apart a

value proportional to the sine of the phase of the signal, and a value proportional to the cosine of the phase of the signal are computed. The sum of the squares of these two differences results in a measurement of signal amplitude, independent of signal phase. After the passing of the electron, when the resonant circuit is oscillating at an amplitude of $\frac{\eta e}{C_s}$, this will build up to a maximum signal of:

$$S^2 = (S_0 - S_2)^2 + (S_1 - S_3)^2 = 4N^2 \left(\frac{\eta e}{C_s}\right)^2 \tag{6.88}$$

$$S_m = \sum_{n=1}^{N} \frac{\eta e}{C_s} sin\left(\phi + \omega t_{n,m}\right) \tag{6.89}$$

$$t_{n,m} = \frac{2\pi n}{\omega} + \frac{m\pi}{2\omega} \tag{6.90}$$

where e is the electron charge, ω is the angular oscillation frequency of the resonator, C_s is the effective circuit capacitance for signal development (see equation 6.78), ϕ is the relative phase of the signal and sampling, and η is proportionality constant relating the expected change in cavity voltage to a passing charge. Before the electron passes S^2 will be zero, allowing the difference in S^2 from consecutive sums over N resonator oscillation periods to be used to reject noise. This difference will build up to the maximum over N oscillation periods, then drop back down to zero over another N oscillation periods. This can be realized by just tracking the change, adding a new event each time and subtracting the value N samples ago — which requires a buffer of $4N$ samples.

The resonant circuit will also be oscillating due to thermal noise, with an expected voltage variance given by:

$$\left\langle \Delta V_n^2 \left(\Delta\omega\right)\right\rangle = \frac{k_B T}{C_n} \frac{2Q}{\pi\omega\left(1 + \left(\frac{2Q\triangle\omega}{\omega}\right)^2\right)} \tag{6.91}$$

where C_n is the effective capacitance of the resonator seen by the noise generator, k_b is Boltzmann's constant, and T is temperature. The shape of the noise spectrum is a Lorentzian with a width determined by the resonator quality (Q). The voltage noise is reduced by the

voltage divider formed by the amplifier input capacitance (C_a) and the probe capacitance (C_p). For a frequency away from the oscillator resonance of $\Delta\omega$ the voltage is:

$$V_n(\Delta\omega) = Asin(\omega t + \Delta\omega t) + Bcos(\omega t + \Delta\omega t) \tag{6.92}$$

$$\left\langle A^2 + B^2 \right\rangle = \frac{k_B T}{C_n} \left(\frac{C_p}{C_a + C_p} \right)^2 \frac{2Q}{\pi\omega \left(1 + \left(\frac{2Q\triangle\omega}{\omega} \right)^2 \right)} \tag{6.93}$$

$$C_n = C_L + \frac{C_a C_p}{C_a + C_p} \tag{6.94}$$

To determine the effect of resonance noise on the sums, first determine the effect for a single frequency.

$$S_m = \sum_{n=1}^{N} Asin(\omega t_{n,m} + \Delta\omega t_{n,m}) + Bcos(\omega t_{n,m} + \Delta\omega t_{n,m}) \tag{6.95}$$

Using the sum of angles formula for sine and cosine, and the values of t given by equation 6.90 gives:

$$S_0 = \sum_{n=1}^{N} Asin(\Delta\omega t) + Bcos(\Delta\omega t) \tag{6.96}$$

$$S_1 = \sum_{n=1}^{N} Acos(\Delta\omega t) - Bsin(\Delta\omega t) \tag{6.97}$$

$$S_2 = \sum_{n=1}^{N} -Asin(\Delta\omega t) - Bcos(\Delta\omega t) \tag{6.98}$$

$$S_3 = \sum_{n=1}^{N} -Acos(\Delta\omega t) + Bsin(\Delta\omega t) \tag{6.99}$$

Assuming that $m \ll N \ll Q$, then $\Delta\omega t \ll 1$ and sine and cosine terms can be approximated by their series expansions.

$$\sum_{n}^{N} sin(\Delta\omega t) \approx \sum_{n}^{N} \frac{\Delta\omega}{\omega} \left(2n\pi + \frac{m\pi}{2} \right) \approx 2\pi \frac{\Delta\omega}{\omega} \frac{N^2}{2} \tag{6.100}$$

$$\sum_{n}^{N} cos(\Delta\omega t) \approx \sum_{n}^{N} 1 - \frac{\left(\frac{\Delta\omega}{\omega}\left(2n\pi + \frac{m\pi}{2}\right)\right)^2}{2} \approx N - \left(2\pi\frac{\Delta\omega}{\omega}\right)^2 \frac{N^3}{3} \tag{6.101}$$

The signal is processed by looking for a change in S by taking the difference between S calculated for N samples and subtracting S for the previous N samples, the zeroth order terms in the noise cancel.

$$\begin{aligned} S_{noise}\left(\Delta\omega\right) = &\sum_{n=N+1}^{2N} Asin\left(\omega t + \Delta\omega t\right) + Bcos\left(\omega t + \Delta\omega t\right) \\ &- \sum_{n=1}^{N} Asin\left(\omega t + \Delta\omega t\right) + Bcos\left(\omega t + \Delta\omega t\right) \end{aligned} \tag{6.102}$$

$$S_{noise}^2\left(\Delta\omega\right) \approx 4\left(2\pi\frac{\Delta\omega}{\omega}\right)^2 N^4 \left\langle A^2 + B^2 \right\rangle \tag{6.103}$$

assuming $N\Delta\omega \ll \omega$. For the noise from the resonator itself, using the expected voltage noise from equation 6.93, is:

$$S_{noise}^2\left(\Delta\omega\right) \approx 4\left(2\pi\frac{\Delta\omega}{\omega}\right)^2 N^4 \frac{k_B T}{C_n}\left(\frac{C_p}{C_a + C_p}\right)^2 \frac{2Q}{\pi\omega\left(1 + \left(\frac{2Q\triangle\omega}{\omega}\right)^2\right)} \tag{6.104}$$

The small angle approximation overestimates the noise if integrated over too wide a range of frequencies, which causes the integral to diverge. It can be reasonably approximated by an integral over the width of the resonance at half maximum.

$$S_{noise}^2 \approx \frac{8N^4\pi}{Q^2}\frac{k_B T}{C_n}\left(\frac{C_p}{C_a + C_p}\right)^2 \tag{6.105}$$

This yields a signal-to-noise ratio of:

$$\frac{S^2}{S_{noise}^2} \approx \frac{Q^2}{2\pi N^2}\left(\frac{\eta e}{C_s}\right)^2 \frac{C}{k_B T}\left(\frac{C_p + C_a}{C_p}\right)^2 = \frac{Q^2\eta^2 e^2}{2\pi N^2 k_B T}\frac{C_a^2}{\left(C_a + C_p\right)\left(C_L C_p + C_L C_a + C_p C_a\right)} \tag{6.106}$$

This favors high values for the resonator quality Q, small values for N.

There is an additional white noise from the amplifier to account for. For a white noise with spectral density of $\langle V_n^2 \rangle$, the voltage averaged over a time Δt is Gaussian with a variance [60]:

$$\left\langle V^2 \right\rangle = \frac{\langle V_n^2 \rangle}{2\Delta t} \tag{6.107}$$

The filter technique results in a sum of $8N$ voltage measurements, averaged over a time from equation 6.90 of:

$$\Delta t = \frac{\pi}{2\omega} \tag{6.108}$$

This gives a total expected signal variance of:

$$S^2_{whitenoise} = 8\frac{N\omega}{\pi}V_n^2 \tag{6.109}$$

The shot noise comes in as single electrons of charge. Therefore, if the tagger is sensitive enough to detect single electron events, shot noise events should also be individually resolvable and look similar to a passing electron. However, a passing electron induces around one electron of image charge then removes the same charge as it passes, leaving a net charge on the resonant circuit of zero. A shot noise event will leave a net charge of one electron on the circuit. While equation 6.88 will give a signal of $4N^2\left(\frac{e}{C}\right)^2$ for shot noise, another filter using the sum:

$$S^2_{shot} = (S_0 + S_1 + S_2 + S_3)^2 \tag{6.110}$$

will give a result of $16N^2\left(\frac{e}{C}\right)^2$, for an effective circuit capacitance seen at the amplifier input. This sum will instead be zero for a passing electron, as there is no net charge, providing a means of identifying and removing shot noise events. The amplifier $1/f$ noise can be added to the existing white noise, which should only be necessary if the $1/f$ knee frequency is above $1/N\Delta t$.

Another source of noise arises due to the need to provide a DC ground path for the amplifier. Along the inductor there is a virtual ground, at a position determined by C_p and

C_a. Placing a DC ground path at this position will provide no AC loading and prevent reducing the resonator quality.

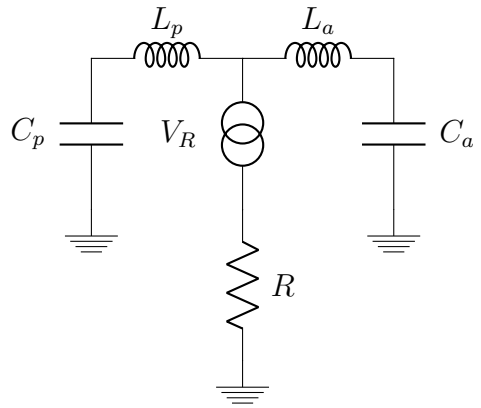

For a voltage between the amplifier and probe, the voltage at the ground point due to the capacitive voltage divider should equal the voltage between the inductors due to the inductive voltage divider. This is satisfied when:

$$C_p L_p = C_a L_a \tag{6.111}$$

A conservative estimate of the Johnson noise due to the resistor is to assume the voltage is applied to the series combination of the resistor (R) and the capacitive impedance of the resonator capacitance (C), as the inductance impedance will serve only to reduce the voltage seen at the amplifier input even further.

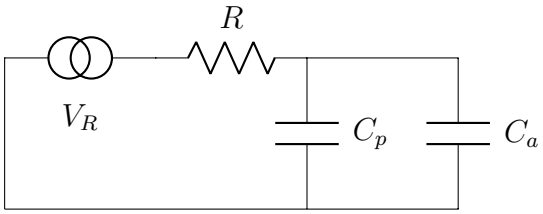

This gives an expected voltage noise spectral density limited to:

$$\left\langle V^2\left(\omega\right)\right\rangle < 4\,k_b T\,R\frac{C^2\omega^2}{R^2 + C^2\omega^2} \tag{6.112}$$

$$C = C_p + C_a \tag{6.113}$$

which can be kept arbitrarily small by using a sufficiently large resistor. To keep this noise smaller than the signal:

$$4\,k_b T\,R\frac{C^2\omega^2}{R^2+C^2\omega^2} < \left(\frac{\eta e}{C_s}\right)^2 \tag{6.114}$$

6.2.6.1 Example

Using a 10 cm inner diameter loop made of 0.1 mm diameter wire, with electrons traveling at 0.2 c, $\eta = 0.44$, probe capacitance $C_p = 2.6$ pF, and the angular frequency of oscillation $\omega = 7.14 \cdot 10^8\,{}^{\text{radians}}/_{\text{second}}$. Using values for an ATF-35143 pHEMT from Avago Technologies: $C_a = 2.3$ pF and $R_a = 100$ mΩ. The 60A582C inductor from Murata Power Solutions has a stray capacitance, estimated from its self-resonant frequency, around $C_L = 4.5$ pF and a series resistance of $R_s = 5$ mΩ with near the 4.8 μH inductance needed to resonate at the optimum frequency. Treating the input resistance of the FET package as an additional series resistance to the resonator, this puts Q at around 9000. The parallel resistance of the FET is assumed to be large enough that is not a significant noise contribution. Noise isn't specified for colder than -40 C, but using the noise factor for -40 C the ATF-35143 will have a voltage noise around $80\,{}^{\text{pV}}/\sqrt{\text{Hz}}$. Assuming the circuit is cooled to 4.2 K for the thermal noise of the resonant circuit, this gives a peak signal-to-noise ratio of 0.020 at N=188. The desired timing resolution of 1 μs limits N to 114, for a signal-to-noise ratio of 0.018. The signal-to-noise ratio is plotted against N, for contours of resonator quality (Q) and transistor voltage noise spectral density (V_n), with the expected performance using an ATF-35143 shown in figure 6.12.

6.2.6.2 Down Conversion

The improved readout scheme doesn't have to be done at a sampling frequency of four times the resonator frequency. Assume the signal is:

$$V_r = A\sin(\omega_r) + B\cos(\omega_r) \tag{6.115}$$

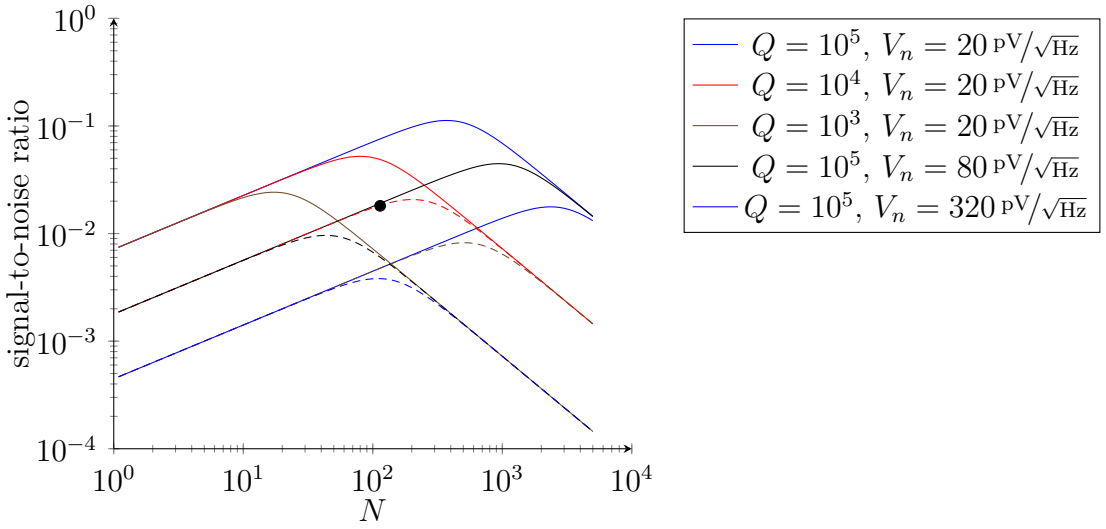

Figure 6.12: Loop and LC π resonator signal-to-noise. Contours are in powers of 10 for quality (Q), and powers of 4 for amplifier voltage noise (V_n). The legend labels the best amplifier voltage noise and quality lines, the other contours follow the same pattern. The point is for the expected performance using an ATF-35143 amplifier and 60A582C inductor.

and it is mixed with a signal from a local oscillator:

$$V_l = a \sin(\omega_l) + b \cos(\omega_l) \tag{6.116}$$

If the sampling is done on quarter periods of an angular frequency:

$$\omega_s = \omega_r - \omega_l \tag{6.117}$$

Then as long as the following condition is met:

$$\omega_r = \omega_l(1 + 1/n) \tag{6.118}$$

where n is an integer, the result of the summing scheme in equation 6.88 will be:

$$S^2 = \begin{cases} 4\,N^2\,b^2\,(A^2 + B^2) & n\ even \\ 4\,N^2\,B^2\,(a^2 + b^2) & n\ odd \end{cases} \tag{6.119}$$

If the local oscillator is synchronized to the samples, then it is possible to force $b = 1$. Thus for an even value of n, the full signal amplitude can still be sampled. This allows a high-frequency resonant structure to be sampled with a lower frequency analog-to-digital converter (ADC).

6.2.6.3 Multiple Detectors

If the available space were increased, it would be possible to add multiple detectors. Cross talk could be minimized by placing ground planes between pick up loops, which should allow for a maximum detector spacing with minimum stray capacitance for some detector spacing on the order of the loop diameter. Simply summing up S^2 from each detector wouldn't provide much improvement, as both the noise and the signal would add in quadrature. Adding up the S_m sums from each detector, with a weighted contribution based on electron speed, would result in a the signal adding linearly and the noise adding in quadrature —

giving an improvement as the square root of the number of detectors. Since the weighting of the S_m's depends on electron speed, this could also determine electron pitch angle.

6.2.7 Sense Current with SQUID

Another option is to sense the current in the circuit instead, by sensing the flux on an inductor. The change in current in the resonator is independent of excitation, for the same reason the voltage is. So instead of $\Delta V = \eta \frac{e}{C}$ use $\Delta i = \eta e \omega$. Just as in section 6.1.4 the large inductance becomes a problem if trying to use the inductor coupled to the SQUID as the circuit inductance. But, a much smaller inductor in series with a large inductor could be used to achieve the desired frequency. Assuming $\eta \approx 0.5$, a resonant frequency of 151 MHz, and $L \approx 10\,\text{nH}$ for 1 cm diameter single loop inductor: the flux would be $\sim 3 \cdot 10^{-4}\,\Phi_0$, where Φ_0 is a flux quanta. To meet the measurement time resolution of 1 μs a SQUID would have to have a flux sensitivity around $3 \cdot 10^{-7}\,\Phi_0/\sqrt{\text{Hz}}$. This is on the order of the sensitivity of a good SQUID. It will also be riding on thermal noise. From the equipartition theorem the expected thermal current amplitude will be:

$$\langle i_n \rangle = \sqrt{\frac{2k_b T}{L_T}} \tag{6.120}$$

where k_b is Boltzmann's constant, T is the temperature of the resonator, and L_T is the total inductance of the resonator. Using $T = 4.2\,\text{K}$ and $L_T = 4.8$ μH, the amplitude on a 10 nH single loop inductor would be $0.024\,\Phi_0$. As long as the resonator is high quality, this should be a steady background that can be filtered out.

6.3 Electron Tagger Conclusions

The energy exchange with a resonant structure is still being explored. The optimum response is well understood. The performance depends on the voltage noise of the amplifier (V_a) and the quality of the resonator (Q). For the model using off-the-shelf components Q around 9000 can be expected. The timing resolution needs to be about $1\,\mu s$, which for a 10 cm

loop limits N to about 100. Having a Q far greater than 100,000 will ensure the noise is dominated by the amplifier voltage noise.

The quality of a series RLC resonator goes as $1/RC$. The resistance is dominated by the FET package, which could be reduced by using a bare die FET. The capacitance includes a significant contribution from the stray capacitance of the inductor (C_L, see equation 6.94). This stray capacitance also results in a reduction of signal amplitude (see equation 6.78). This means the major focus should be on reducing C_L as it not only reduces noise, but raises signal. For the example model used (see section 6.2.6.1) C_L reduces the signal to 21% of what would be expected for $C_L = 0$. Using a super conductor to construct a long, thin inductor will reduce the stray capacitance.

The limits of noise temperature for a HEMT is around 1K at 50 Ω, for a voltage noise spectral density of $50\,\mathrm{pV}/\sqrt{\mathrm{Hz}}$. Were this the only limit, then limiting N to 114 for timing resolution and eliminating C_L would give a signal-to-noise ratio (SNR) of around 0.14 for a Q of 100,000. It may be possible to achieve a lower voltage noise, as the amplifier need not be matched to 50 Ω.

The SQUID measurement of current may be a better option. However, there are likely a number of unaccounted for issues that will result in it being a borderline method. And there are a number of improvements that can be made for the HEMT method. Both are still worth pursuing, since there is no clear indication one method is better at this time.

Chapter 7

ELECTRON TAGGER BACKGROUND

7.1 Sources Considered

An electron tagger would detect not only the electrons that make it to the focal-plane detector, but all other electrons that pass its position in the beamline. The tagger must be placed before the main spectrometer, but should be placed in a low-rate area. It is also favorable to have the flux tube through the tagger have a small diameter. Just after the center of the 4.5 T magnet between the pre-spectrometer and main spectrometer, so that magnetic reflection reduces the flux through the tagger for ions trapped in the pre-spectrometer, is a good position. There are two major sources of electrons that have been considered at this point in the beam line.

- Electrons from the source that make it through the pre-spectrometer, are reflected by the retarding potential in the main spectrometer, and then go back through the pre-spectrometer and are absorbed in the rear section. These will each pass the electron tagger twice.

- Electrons from the source that make it through the pre-spectrometer, are reflected by the main spectrometer, but lack the energy to make it back through the pre-spectrometer and become trapped. These electrons could pass the electron tagger millions of times.

7.1.1 Electrons Passing Through the Pre-spectrometer

Electrons from the source that pass the pre-spectrometer retarding potential, and the magnet at the end of the pre-spectrometer, make two passes passes through the tagger. From

equation 2.2 applied to the pre-spectrometer, with a source magnetic field of 3.6 T and the magnet at the end of the pre-spectrometer at 4.5 T we find the magnet reflects all electrons with a starting angle at the source greater than 63 degrees. Solving equation 5.1 for E when the parallel velocity is zero, we find the minimum initial kinetic energy to pass through the pre-spectrometer is given by:

$$E_{min}(\theta, U, B) = \frac{e^2U^2 - 2\left(eU + k - 1\right)mc^2}{2eU + k - 1} \tag{7.1}$$

$$k = \sin^2\theta \frac{B}{B_s}$$

where e is the electron charge, m is the electron mass, θ is the starting angle at the source, U is the retarding potential of the pre-spectrometer, B_s is the magnetic field in the source, and B is the magnetic field at the retarding plane of the pre-spectrometer.

Combining equations 1.8 and 7.1 we find the average rate of electrons from the pre-spectrometer passing the electron tagger is:

$$2\int_0^{\theta_{pre}} \frac{2\pi\, sin\,\theta}{4\pi} d\theta \int_{E_{min}}^{E_0} \frac{dN}{dE}(E) \tag{7.2}$$

where E_0 is the maximum kinetic energy of the electron, θ_{pre} is the maximum starting angle in the source to avoid magnetic reflection before the electron tagger, and $\frac{dN}{dE}(E)$ is the rate at the source for electrons with kinetic energy E, given by equation 1.8 and the source strength. The 2 is due to each electron making two passes. This assumes that all electrons that make it through the pre-spectrometer, are reflected by the main spectrometer, then make it back through the pre-spectrometer and are absorbed in the rear section — which the vast majority are. The rate will depend on the pre-spectrometer retarding potential and is shown in figure 7.1.

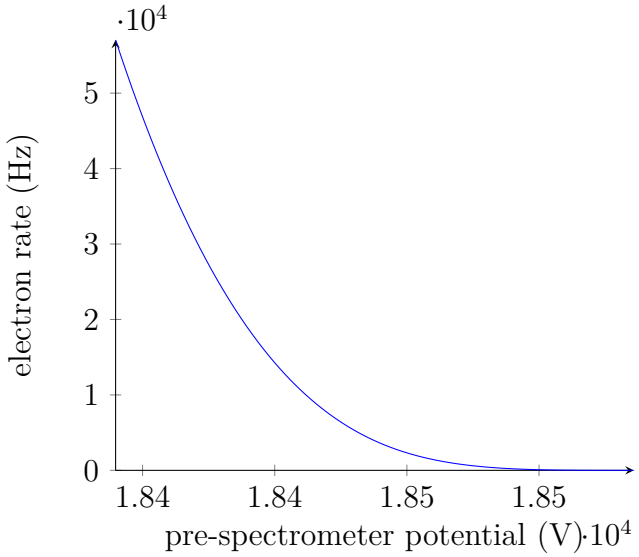

Figure 7.1: Rate from source electrons, which make it through the pre-spectrometer, each passing the electron tagger twice.

7.1.2 Electrons Trapped in the Penning Trap

The magnetic field constraining the electrons between the high retarding potential of the pre-spectrometer and main spectrometer form a Penning trap. Once electrons are trapped in this region they will pass the electron tagger at a rate on the order of 10^5 times per second. For the region of interest for an electron that makes it to the detector, there will be on the order of one background event for every trapped electron. These will occur at a regular interval with two alternating periods between passes, one for travel through the pre-spectrometer and another for the main spectrometer. If the number of trapped electrons is kept low it is expected their signal can be identified and removed.

7.1.2.1 Electrons Trapped by Radiating

Electrons which make it though the pre-spectrometer and are reflected by the main spectrometer radiate a small amount of energy before returning to the pre-spectrometer. This

radiation in a uniform magnetic field would serve only to reduce the kinetic energy associated with the charged particle movement perpendicular to the magnetic field. The pitch angle would reduce, but the velocity parallel to the magnetic field would be unchanged.

Consider a boost parallel to the magnetic field, to a frame where the electron is in uniform circular motion. In this frame the magnetic field is changed in amplitude, but is still in the same direction and only causes force on the electron in the plane of motion. As seen in the electromagnetic field tensor [54, p. 556] the electric field that results from the boost is all in the plane of motion, and only causes force on the electron in the plane of motion as well. The electron is radiating energy due to its motion, but, as the motion is all in one plane the radiation must be symmetrical across the plane. Therefore the electron will never gain momentum perpendicular to this plane of motion. Returning to the lab frame, the motion of the electron parallel to the magnetic field never changes.

However, since this energy is radiated in the high magnetic field region, where the motion perpendicular to the magnetic field is maximal, and when the electrostatic filter is applied the magnetic field is low, the change in energy is almost entirely associated with momentum parallel to the magnetic field due to magnetic collimation. To a good approximation, all the lost energy results in reduced ability of the electron to overcome the electrostatic filter in the pre-spectrometer. The lost energy from cyclotron radiation is given by the Larmor formula previously given in equation 6.1. In the Larmor formula the change in four-momentum depends on the pitch angle the electron has with the magnetic field while it is radiating, which changes due to adiabatic collimation. The ratio of the electron speed perpendicular to the magnetic field to the speed of light is given by:

$$\beta_{\perp}\left(\theta, E, B, U\right) = \frac{sin\,\theta\,\sqrt{\frac{B}{B_s}}\,mc^2}{E + mc^2 - eU} \tag{7.3}$$

where θ is the initial pitch angle in the source, E is the electron energy ignoring the retarding potential, U is the change in potential along the path, B is the magnetic field along the path, B_s is the magnetic field in the source, e is the electron charge, m is the electron

mass, and c is the speed of light. The energy lost per pass from the pre-spectrometer to the main spectrometer is given by

$$\Delta E\left(\theta, E\right) = -\int_{a}^{b} dz \frac{P\left(\beta_{\perp}\left(\theta, E, B\left(z\right), U\left(z\right)\right), B\left(z\right)\right)}{v_{\parallel}} \tag{7.4}$$

where a and b are the points in the pre-spectrometer and main spectrometer where the electron speed parallel to the magnetic field $\left(v_{\parallel}\right)$ is zero (see equation 5.1). Radiated power (P) is proportional to the square of magnetic field and the square of the transverse velocity. From equation 7.3, the square of the transverse velocity is also proportional to magnetic field. Thus radiated power is proportional to the cube of the magnetic field. Away from the coil of the magnet the magnetic field falls off as the distance cubed. So radiated power falls of as the ninth power of distance from the coil.

$$P \propto \beta_{\perp}^{2} B^{2} \propto B^{3} \propto z^{-9}$$

It is reasonable to approximate the energy lost each pass as that due to a constant field magnetic field of 4.5 T for a distance of 50 cm, the strength of the magnetic field and length of the bore of the magnet between the spectrometers.

$$\Delta E\left(\theta, E\right) = -L \frac{P\left(\theta, E, B\right)}{\beta_{\parallel}\left(\theta, E\right) c} \tag{7.5}$$

where θ is the initial angle at the source. Assuming the electron comes back to the same retarding potential in the pre-spectrometer, to become trapped it must be in the narrow window in the energy spectrum above E_{min} given by equation 7.1, but below $E_{min} + \Delta E$. SinceΔE is small compared to the slope of the spectrum, we can approximate the energy spectrum as constant over this energy. The rate of electrons becoming trapped is approximately:

$$\int_{0}^{\theta_{pre}} \frac{dN}{dE}\left(E_{min}\right) \Delta E\left(\theta, E_{min}\right) \frac{2\pi \, sin\, \theta}{4\pi} d\theta \tag{7.6}$$

Where $\frac{dN}{dE}(E)$ is the rate of electrons generated in the source given by equation 1.8 and θ_{pre} is the maximum pitch angle in the source that makes it through the pre-spectrometer (determined by equation 2.2 using the source magnetic field and the strongest magnet before the pre-spectrometer).

It was assumed that the electrons returned to the exact same point in the pre-spectrometer, and the only reason for not overcoming the retarding potential was due to radiated energy. But, the electron could return to a different point with a higher retarding potential or a stronger magnetic field and become trapped. It is also likely an electron that would have become trapped will return to a point with a lower retarding potential or weaker magnetic field and make it back through the pre-spectrometer after only a few passes. From equation 7.4 the energy lost per pass takes its maximum value of 1.0 meV at θ_{pre},the gyration radius in the retarding plane of the pre-spectrometer at θ_{pre} is around 1.5 mm. This may seem a very small number for the low field region, but the collimation causes the electrons to align with the magnetic field reducing their pitch angle. From equation 7.1 we find that it takes a magnetic field difference in the retarding plane of only 2.4 mG to result in a 1.0 meV difference in the minimum energy needed to pass through the pre-spectrometer. The magnetic field in the pre-spectrometer varies by about $50\,{}^{\mathrm{G}}/_{\mathrm{m}}$ [40, p. 96], but it should cancel out with the rate of trapped electrons being freed to first order. While this does indicate the trapping rate isn't accurate, it still provides an estimate of the scale at which trapping by radiation losses occurs. The rate assuming the field inhomogeneity is just as likely to trap an electron as free an electron, which depends on pre-spectrometer retarding potential, is shown in figure 7.2.

Electrons radiating through gyration in a magnetic field lose transverse momentum, but their longitudinal momentum does not change, lowering their pitch angle. The number of passes for a trapped electron was estimated using a modification of formula 7.5. Instead of keeping track of the angle of the electron as it radiates, the initial speed through the magnet was determined and assumed to be constant. The initial transverse momentum was separated out to solve for the radiation power, and the energy stored in transverse momentum ($E_{\perp}$)

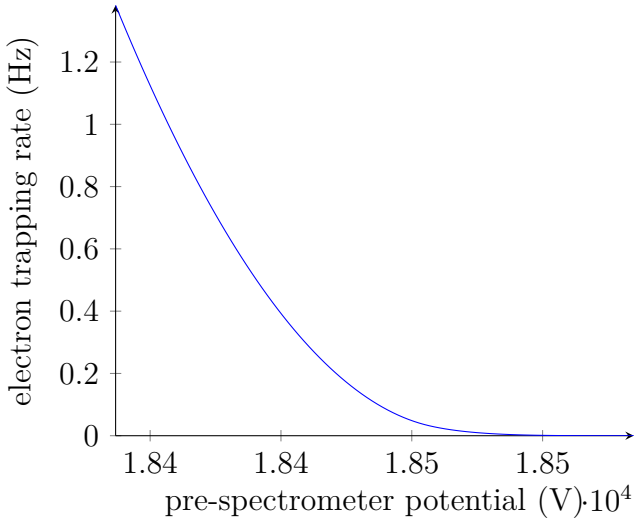

Figure 7.2: Rate of source electrons trapped due to cyclotron radiation.

was considered to be the only energy that changes. Integrating from some initial energy to a final energy over the energy lost per pass gives an estimate of the number of passes a trapped electron will make while still radiating:

$$\int_{E_i}^{E_f} \frac{dE_\perp}{\triangle E_\perp(v_\parallel, E_\perp)} \tag{7.7}$$

where initial energy (E_i) is taken to be the energy where the electron just barely makes it through the pre-spectrometer, given by equation 7.1.

If the final energy(E_f) is simply 0, the integral comes out to about $16 \cdot 10^6$ passes for each trapped electron, the value varies slightly depending on pre-spectrometer potential, as the trapped electrons will start with higher energy for a higher potential. Taking into account that a tagger sensing radiation would have a minimum sensitivity reduces this. Assuming the tagger only recognizes electrons emitting at least 10% of the power of an endpoint electron at the maximum pinch angle, $8 \cdot 10^6$ passes would be expected for each trapped electron.

This would be a reasonable estimate if the detection method were cyclotron radiation,

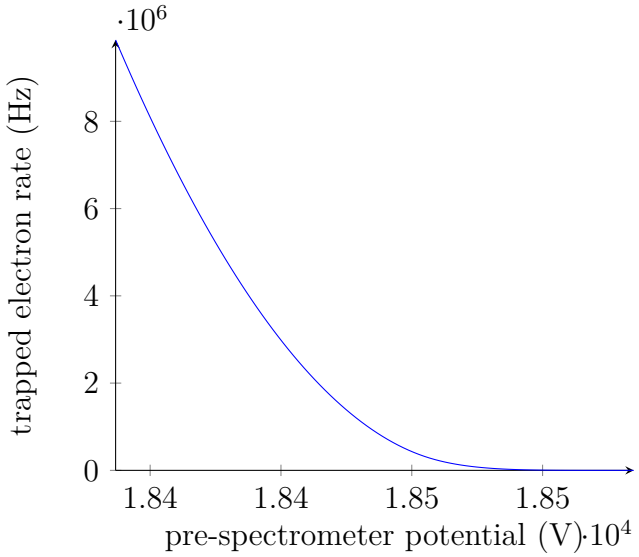

Figure 7.3: Rate of electrons trapped due to radiation passing the electron tagger, assuming the electron tagger detection threshold is 10% of the maximum radiated power and the electrons never become untrapped.

but not for detection of the image charge as the energy associated with momentum parallel to the magnetic field isn't reduced by radiating. The number of passes for electrons that must scatter to be freed can be determined from the mean free path (see section 7.1.2.2).

Using equations 7.6 and 7.8 we find the total rate of trapped electrons passing the electron tagger will build up to be:

$$\int_{0}^{\theta_{pre}} \int_{E_i(\theta,E)}^{E_f(\theta,E)} \frac{dE_\perp}{\Delta E_\perp(v_\parallel(\theta,E),E_\perp)} \frac{dN}{dE}(E_{min})\,\Delta E(\theta,E_{min})\,\frac{2\pi\,sin\,\theta}{4\pi} d\theta \tag{7.8}$$

7.1.2.2 Filling by Scattering

For tritium data runs the spectrometer system will be baked prior to operation, resulting in a very long mean free path for electrons. The total scattering cross section can be approximated as [54, p. 643]:

$$\sigma = \pi a^2 \left(\frac{1}{4\pi\epsilon_0} \frac{2Ze^2}{\hbar\nu} \right)^2 \tag{7.9}$$

where ν is the electron speed, e is the electron charge, Ze is the nucleus charge, and $a \approx 1.4\, a_0\, Z^{-1/3}$ is the classical atomic radius and a_0 is the Bohr radius. This formula is only a rough approximation, and is intended for atoms not molecules, but it's good enough for an order of magnitude estimate. Using the post baking residual gas measurement from the 2016 main spectrometer commissioning [46], the mean free path for an electron at 18.6 keV is approximately $4 \cdot 10^9$ m. Depending on the pre-spectrometer potential, up to 60,000 electrons could be passing through the pre-spectrometer per second, but that's still only on the order of one electron trapped per hour. Trapped electrons can be expected to pass the tagger $\sim 10^9$ times before scattering.

7.1.3 Penning Trap Wipers

As the time-of-flight through the main spectrometer for an electron of interest is 10s of μs, removing trapped electrons will be required to implement time-of-flight mode. Trapped electrons will pass through the tagger with a period on the order of time-of-flight for electrons through the main spectrometer, resulting in even a single electron usually causing a spurious signal in the region of interest for every event at the focal plane detector. However, the trapped electrons will pass the tagger at a regular interval, with one delay determined by their travel through the pre-spectrometer and another for the main spectrometer. As long as the rate from trapped electrons doesn't rise beyond the time resolution of the tagger they should be identifiable. Assuming the tagger has about the same time resolution as the focal plate detector this would allow eliminating the background from around a hundred trapped electrons.

Trapped electrons also build up until the trap empties, possibly resulting in a damaging discharge to the FPD wafer. Wipers were installed in the beam line which serve to empty the penning trap between the spectrometers. However, once the penning trap starts to fill it

fills exponentially until discharge. Therefore, no safe frequency for wiper operation has been found that will keep the penning trap from causing damaging discharges. Either a wiper will need to be permanently positioned in the beam line, which would obscure a few pixels, or some way of detecting filling of the penning trap is needed.

An electron tagger that is not sufficient for single electron detection may still be able to fulfill this purpose. Each trapped electron would pass the tagger about 10^5 times a second. This should register as a detectable rise in background level, even for a tagger with well below single-electron sensitivity.

Chapter 8

CONCLUSIONS

Because they are so weakly interacting, neutrinos are a useful observational tool, providing information that more strongly interacting particle can't. They play an important role in testing the standard solar model, and reconciliation of the neutrino flux prediction with observation disproved a long-held assumption of the standard model of particle physics: neutrino oscillation showed that neutrinos do have mass and it is at least $0.02\,{}^{\mathrm{eV}}/_{\mathrm{c}^2}$. Neutrinos made an important imprint on early cosmological evolution, and a direct measurement of neutrino mass may help in development of more accurate cosmological models.

The first limit on neutrino mass came in 1932, when Fermi introduced his model for beta decay and it was used to interpret existing data. Upper limits continue to be placed using the shape of the beta decay spectrum. The current direct neutrino mass measurement limit for the electron antineutrino is $2.05\,{}^{\mathrm{eV}}/_{\mathrm{c}^2}$, from the combined results of the Mainz and Troitsk. Both used a MAC-E spectrometer measuring the spectrum of tritium beta decay, and the Troitsk experiment used a gaseous source while the Mainz experiment used a solid source. KATRIN's design goal is to push this limit down to $0.2\,{}^{\mathrm{eV}}/_{\mathrm{c}^2}$ (90% confidence level), or measure it if larger than $0.35\,{}^{\mathrm{eV}}/_{\mathrm{c}^2}$, using a MAC-E spectrometer and a gaseous source — an improvement of two orders of magnitude in mass squared.

Performance of the detector is critical to achieving the design sensitivity. The illumination device has achieved better than 10:1 uniformity, sufficient to allow testing all pixels using the electron source — previously some pixels had such high rates they would swamp the DAQ hardware and inhibit testing of the lower-rate pixels. The electron source meter allows measuring the absolute detection efficiency of the detector system. It also has other applications as a high-rate detector, like checking beam intensity prior to exposing the more

sensitive silicon wafer.

The background in KATRIN is currently higher than was expected, which may prevent it from reaching design sensitivity. Detector resolution has been worsening, an issue still under investigation at the time of this writing. The automated wafer tester resulted in ensuring the wafer-flange assembly has 100% working pixels prior to installation. Equipment initially developed for the wafer tester has been used in testing other aspects of the wafer, helping to narrow down possible causes of the reduced detector resolution.

In addition to detector resolution issues, years of radon exposure have left a higher than expected background in the KATRIN main spectrometer [61]. Implementing a time-of-flight mode could result in not only a background reduction, but allow measuring the energy of each electron instead of the integrated spectrum above the retarding potential. This could provide a substantial improvement in time required to reach the same statistical accuracy, if an electron tagger sensitive to single electrons can be developed.

While single electrons have been detected moving between quantum dots [53], the goal of non-destructive detection of electrons through a large aperture remains to be achieved. Multiple methods towards this end were considered:

Detection of image charge with a single electron transistor.

Detection of magnetic field change from a passing electron.

Detection of cyclotron radiation emission.

Detecting the image current with a SQUID.

Detecting change in oscillations of a resonant structure caused by a passing electron.

The effect on a resonant structure seems promising. While the voltage change caused by a passing electron is much smaller than expected thermal fluctuations, the effect persists long after the electron has passed. This improvement in readout time allows detection of the signal in a much narrower bandwidth than methods that must make a measurement while the electron is present in the detection region. Though a single detector may not achieve the required sensitivity, summing the signal from multiple detectors may provide single electron sensitivity. An added benefit of multiple detectors could be electron pitch

angle determination, which would result in better energy resolution of either the time-of-flight mode or high-pass-filter mode.

One fundamental limit was identified for this scheme: energy exchange should be sufficient to excite the resonator, so it should be greater than the excitation quanta spacing of $\hbar\omega$. Thermal excitation will likely be sufficient — if not, then a small drive signal may be applied.

BIBLIOGRAPHY

[1] C. D. Ellis and W. A. Wooster. "The Average Energy of Disintegration of Radium E". In: *Proceedings of the Royal Society of London A: Mathematical, Physical and Engineering Sciences* 117.776 (Dec. 1927), pp. 109–123. DOI: 10.1098/rspa.1927.0168.

[2] W. Pauli. "Dear radioactive ladies and gentlemen". In: *Phys. Today* 31N9 (1978), p. 27.

[3] J. Chadwick. "Possible Existence of a Neutron". In: *Nature* 129.3252 (Feb. 1932), pp. 312–312. DOI: 10.1038/129312a0.

[4] E. Fermi. "Versuch einer Theorie der β-Strahlen. I". In: *Zeitschrift für Physik* 88.3 (1934), pp. 161–177. DOI: 10.1007/BF01351864.

[5] H. Bethe and R. Peierls. "The "Neutrino"". In: *Nature* 133.3362 (Apr. 1934), pp. 532–532. DOI: 10.1038/133532a0.

[6] S.M. Bilenky. "Neutrino. History of a unique particle". In: *The European Physical Journal H* 38.3 (Dec. 2013), pp. 345–404. DOI: 10.1140/epjh/e2012-20068-9.

[7] F. Reines and C. L. Cowan. "Detection of the Free Neutrino". In: *Phys. Rev.* 92.3 (3 Nov. 1953), pp. 830–831. DOI: 10.1103/PhysRev.92.830.

[8] Raymond Davis. "Attempt to Detect the Antineutrinos from a Nuclear Reactor by the $Cl^{37}(\overline{\nu}, e^{-})A^{37}$ Reaction". In: *Phys. Rev.* 97.3 (3 Feb. 1955), pp. 766–769. DOI: 10.1103/PhysRev.97.766.

[9] T. D. Lee and C. N. Yang. "Question of Parity Conservation in Weak Interactions". In: *Phys. Rev.* 104.1 (1 Oct. 1956), pp. 254–258. DOI: 10.1103/PhysRev.104.254.

[10] C. S. Wu et al. "Experimental Test of Parity Conservation in Beta Decay". In: *Phys. Rev.* 105.4 (4 Feb. 1957), pp. 1413–1415. DOI: 10.1103/PhysRev.105.1413.

[11] M. Goldhaber, L. Grodzins, and A. W. Sunyar. "Helicity of Neutrinos". In: *Phys. Rev.* 109.3 (3 Feb. 1958), pp. 1015–1017. DOI: 10.1103/PhysRev.109.1015.

[12] T. D. Lee and C. N. Yang. "Parity Nonconservation and a Two-Component Theory of the Neutrino". In: *Phys. Rev.* 105 (5 Mar. 1957), pp. 1671–1675. DOI: 10.1103/PhysRev.105.1671.

[13] R. P. Feynman and M. Gell-Mann. "Theory of the Fermi Interaction". In: *Phys. Rev.* 109 (1 Jan. 1958), pp. 193–198. DOI: 10.1103/PhysRev.109.193.

[14] Sheldon L. Glashow. "Partial-symmetries of weak interactions". In: *Nuclear Physics* 22.4 (Feb. 1961), pp. 579–588. DOI: 10.1016/0029-5582(61)90469-2.

[15] Steven Weinberg. "A Model of Leptons". In: *Phys. Rev. Lett.* 19.21 (21 Nov. 1967), pp. 1264–1266. DOI: 10.1103/PhysRevLett.19.1264.

[16] Abdus Salam. "Weak and Electromagnetic Interactions". In: *Conf. Proc.* C680519 (1968), pp. 367–377. DOI: 10.1142/9789812795915_0024.

[17] F.J. Hasert et al. "Observation of neutrino-like interactions without muon or electron in the gargamelle neutrino experiment". In: *Physics Letters B* 46.1 (1973), pp. 138–140. DOI: 10.1016/0370-2693(73)90499-1.

[18] C.Y. Prescott et al. "Parity non-conservation in inelastic electron scattering". In: *Physics Letters B* 77.3 (1978), pp. 347–352. DOI: 10.1016/0370-2693(78)90722-0.

[19] Raymond Davis. "A review of the homestake solar neutrino experiment". In: *Progress in Particle and Nuclear Physics* 32 (Jan. 1994), pp. 13–32. DOI: 10.1016/0146-6410(94)90004-3.

[20] Raymond Davis, Don S. Harmer, and Kenneth C. Hoffman. "Search for Neutrinos from the Sun". In: *Phys. Rev. Lett.* 20.21 (21 May 1968), pp. 1205–1209. DOI: 10.1103/PhysRevLett.20.1205.

[21] G. Danby et al. “Observation of High-Energy Neutrino Reactions and the Existence of Two Kinds of Neutrinos”. In: *Phys. Rev. Lett.* 9.1 (1 July 1962), pp. 36–44. DOI: 10.1103/PhysRevLett.9.36.

[22] M. L. Perl et al. “Evidence for Anomalous Lepton Production in $e^+ - e^-$ Annihilation”. In: *Phys. Rev. Lett.* 35.22 (22 Dec. 1975), pp. 1489–1492. DOI: 10.1103/PhysRevLett.35.1489.

[23] B. Pontecorvo. “Neutrino Experiments and the Problem of Conservation of Leptonic Charge”. In: *Sov. Phys. JETP* 26 (1968). [Zh. Eksp. Teor. Fiz.53,1717(1967)], pp. 984–988.

[24] L. Wolfenstein. “Neutrino oscillations in matter”. In: *Phys. Rev. D* 17.9 (9 May 1978), pp. 2369–2374. DOI: 10.1103/PhysRevD.17.2369.

[25] S.P. Mikheev and A.Y. Smirnov. “Resonance enhancement of oscillations in matter and solar neutrino spectroscopy”. In: *Sov. J. Nucl. Phys. (Engl. Transl.); (United States)* 42.6 (Dec. 1985).

[26] Y. Fukuda et al. “Evidence for Oscillation of Atmospheric Neutrinos”. In: *Phys. Rev. Lett.* 81.8 (8 Aug. 1998), pp. 1562–1567. DOI: 10.1103/PhysRevLett.81.1562.

[27] B. Aharmim et al. “Combined analysis of all three phases of solar neutrino data from the Sudbury Neutrino Observatory”. In: *Phys. Rev. C* 88 (2 Aug. 2013), p. 025501. DOI: 10.1103/PhysRevC.88.025501.

[28] C. Patrignani et al. “Review of Particle Physics”. In: *Chin. Phys.* C40.10 (Oct. 2016), p. 100001. DOI: 10.1088/1674-1137/40/10/100001.

[29] David Griffiths. *Introduction to Elementary Particles*. Wiley VCH Verlag GmbH, Aug. 11, 2008. ISBN: 978-3-527-40601-2.

[30] Ettore Majorana. “Teoria simmetrica dell’elettrone e del positrone”. In: *Il Nuovo Cimento (1924-1942)* 14.4 (1937), p. 171. DOI: 10.1007/BF02961314.

[31] Werner Rodejohann. "NEUTRINO-LESS DOUBLE BETA DECAY AND PARTICLE PHYSICS". In: *International Journal of Modern Physics E* 20.09 (2011), pp. 1833–1930. DOI: 10.1142/S0218301311020186.

[32] Planck Collaboration et al. "Planck 2013 results. XVI. Cosmological parameters". In: *A&A* 571 (2014), A16. DOI: 10.1051/0004-6361/201321591.

[33] Julien Lesgourgues and Sergio Pastor. "Neutrino Mass from Cosmology". In: *Advances in High Energy Physics* 2012 (2012), p. 34. DOI: 10.1155/2012/608515.

[34] P. A. R. Ade et al. "Planck2015 results". In: *Astronomy & Astrophysics* 594 (Sept. 2016), A13. DOI: 10.1051/0004-6361/201525830.

[35] Adam G. Riess et al. "A 3% Solution: Determination of the Hubble Constant with the Hubble Space Telescope and Wide Field Camera 3". In: *The Astrophysical Journal* 730.2 (2011), p. 119. DOI: 10.1088/0004-637X/730/2/119.

[36] J. N. Bahcall and S. L. Glashow. "Upper limit on the mass of the electron neutrino". In: *Nature* 326.6112 (Apr. 1987), pp. 476–477. DOI: 10.1038/326476a0.

[37] Jia-Shu Lu et al. "Constraining absolute neutrino masses via detection of galactic supernova neutrinos at JUNO". In: *Journal of Cosmology and Astroparticle Physics* 2015.05 (2015), p. 044. DOI: 10.1088/1475-7516/2015/05/044.

[38] L. I. Bodine, D. S. Parno, and R. G. H. Robertson. "Assessment of molecular effects on neutrino mass measurements from tritium β decay". In: *Phys. Rev. C* 91 (3 Mar. 2015), p. 035505. DOI: 10.1103/PhysRevC.91.035505.

[39] E Holzschuh. "Measurement of the neutrino mass from tritium beta -decay". In: *Reports on Progress in Physics* 55.7 (1992), p. 1035. DOI: 10.1088/0034-4885/55/7/004.

[40] KATRIN collaboration. *KATRIN design report*. Jan. 2005.

[41] G Beamson, H Q Porter, and D W Turner. "The collimating and magnifying properties of a superconducting field photoelectron spectrometer". In: *Journal of Physics E: Scientific Instruments* 13.1 (1980), p. 64. DOI: 10.1088/0022-3735/13/1/018.

[42] V.M. Lobashev and P.E. Spivak. "A method for measuring the electron antineutrino rest mass". In: *Nuclear Instruments and Methods in Physics Research Section A: Accelerators, Spectrometers, Detectors and Associated Equipment* 240.2 (Oct. 1985), pp. 305–310. DOI: 10.1016/0168-9002(85)90640-0.

[43] A. Picard et al. "A solenoid retarding spectrometer with high resolution and transmission for keV electrons". In: *Nuclear Instruments and Methods in Physics Research Section B: Beam Interactions with Materials and Atoms* 63.3 (1992), pp. 345–358. DOI: 10.1016/0168-583X(92)95119-C.

[44] Ch Kraus et al. "Final results from phase II of the Mainz neutrino mass search in tritium β decay". In: *The European Physical Journal C - Particles and Fields* 40.4 (Apr. 2005), pp. 447–468. DOI: 10.1140/epjc/s2005-02139-7.

[45] V. N. Aseev et al. "Upper limit on the electron antineutrino mass from the Troitsk experiment". In: *Phys. Rev. D* 84.11 (11 Dec. 2011), p. 112003. DOI: 10.1103/PhysRevD.84.112003.

[46] M. Arenz et al. "Commissioning of the vacuum system of the KATRIN Main Spectrometer". In: *Journal of Instrumentation* 11.04 (2016), P04011. DOI: 10.1088/1748-0221/11/04/p04011.

[47] J.F. Amsbaugh et al. "Focal-plane detector system for the KATRIN experiment". In: *Nucl. Instrum. Meth.* A778 (2015), pp. 40–60. DOI: 10.1016/j.nima.2014.12.116.

[48] B.A. VanDevender et al. "Performance of a TiN-coated monolithic silicon pin-diode array under mechanical stress". In: *Nuclear Instruments and Methods in Physics Research Section A: Accelerators, Spectrometers, Detectors and Associated Equipment* 673 (2012), pp. 46–50. DOI: 10.1016/j.nima.2012.01.033.

[49] B.L. Wall et al. "Dead layer on silicon p-i-n diode charged-particle detectors". In: *Nuclear Instruments and Methods in Physics Research Section A: Accelerators, Spec-*

trometers, Detectors and Associated Equipment 744.0 (Apr. 2014), pp. 73–79. DOI: 10.1016/j.nima.2013.12.048.

[50] F. S. Goucher et al. "Theory and Experiment for a Germanium $p - n$ Junction". In: *Phys. Rev.* 81 (4 Feb. 1951), pp. 637–638. DOI: 10.1103/PhysRev.81.637.2.

[51] Simon M. Sze and Kwok K. Ng. *Physics of Semiconductor Devices*. JOHN WILEY & SONS INC, Nov. 14, 2006. 815 pp. ISBN: 9780471143239.

[52] Nicholas Steinbrink et al. "Neutrino mass sensitivity by MAC-E-Filter based time-of-flight spectroscopy with the example of KATRIN". In: *New Journal of Physics* 15.11 (Nov. 2013), p. 113020. DOI: 10.1088/1367-2630/15/11/113020.

[53] Lin-Jun Wang et al. "A graphene quantum dot with a single electron transistor as an integrated charge sensor". In: *Applied Physics Letters* 97.26 (2010), p. 262113. DOI: 10.1063/1.3533021.

[54] John David Jackson. *Classical Electrodynamics*. Third Edition. JOHN WILEY & SONS INC, Aug. 11, 1998. 832 pp. ISBN: 978-0-471-30932-1.

[55] K.K. Likharev. "Single-electron devices and their applications". In: *Proceedings of the IEEE* 87.4 (Apr. 1999), pp. 606–632. DOI: 10.1109/5.752518.

[56] K. M. Lewis et al. "Charge transformer to enhance noise performance of single-electron transistor amplifiers in high-capacitance applications". In: *Applied Physics Letters* 80.1 (Jan. 2002), pp. 142–144. DOI: 10.1063/1.1431393.

[57] Ç. Kurdak and K. M. Lewis. "Noise analysis and optimization of a charge transformer, a noise-matching device for single electron transistors". In: *Journal of Applied Physics* 93.6 (Mar. 2003), pp. 3364–3369. DOI: 10.1063/1.1544412.

[58] *Principles of Microwave Circuits (IEEE Electromagnetic Waves Series)*. The Institution of Engineering and Technology, 1986. ISBN: 0863411002.

[59] F.N.H. Robinson. *Noise Fluctuations in Electronic Devices and Circuits*. Oxford University Press, 1974. ISBN: 9780198593195.

[60] V.Radeka. “Low-noise techniques in detectors”. In: *Annueal Review of Nuclear and Particle Science* 38 (1988), pp. 217–77. DOI: 10.1146/annurev.nucl.38.1.217.

[61] F.Harms (for the KATRIN collaboration). “A model for Rydberg-atom induced backgrounds resulting from deposition of Rn progeny in the KATRIN Main Spectrometer”. In: June 2017.

Appendix A

MAXIMUM CURRENT AND INSTANTANEOUS CHARGE LIMITS OF FPD

A.1 Maximum Current Derivation

The KATRIN Focal-Plane Detector (FPD) wafer is susceptible to damage caused by excessive localized heating. Based on allowing a 200 K temperature rise on the focal-plane detector, the heat conduction of the FPD wafer, and an approximation of the charge deposition, maximum continuous current and instantaneous charge limits were derived. To ensure these limits are not exceeded, the KATRIN detector system is first exposed to the main spectrometer with the electron source disk inserted. The electron source disk is the same size as the beam line for the nominal field configuration, and a small magnetic field adjustment can ensure it completely blocks the detector from the beam line, thus it will absorb any electrons coming from the main spectrometer before they hit the detector. The electron-source current meter (PULCINELLA) measures the current on the disk to ensure no damage will come to the detector. PULCINELLA is capable of measuring currents of up to 600 pA or charge bursts of up to 6 pC in 10 ms. In order to prevent damage to the FPD wafer, continuous current must be limited to 40 μA and discharges to 200 pC. Thus if the current and discharges are within range of PULCINELLA the detector will be safe from damage.

The charge deposition profile and the heat conduction to the FPD flange were modeled by easily calculable approximations. It isn't necessary that these approximations be accurate, only that the heat conduction calculated is less than or equal to the actual heat conduction.

Restricting the heat flux to particular directions makes the model easier, and results in a conservative estimate. The problem was broken up into stages, portions of some stages overlap which results in a conservative estimate. Heat transfer was calculated for four stages

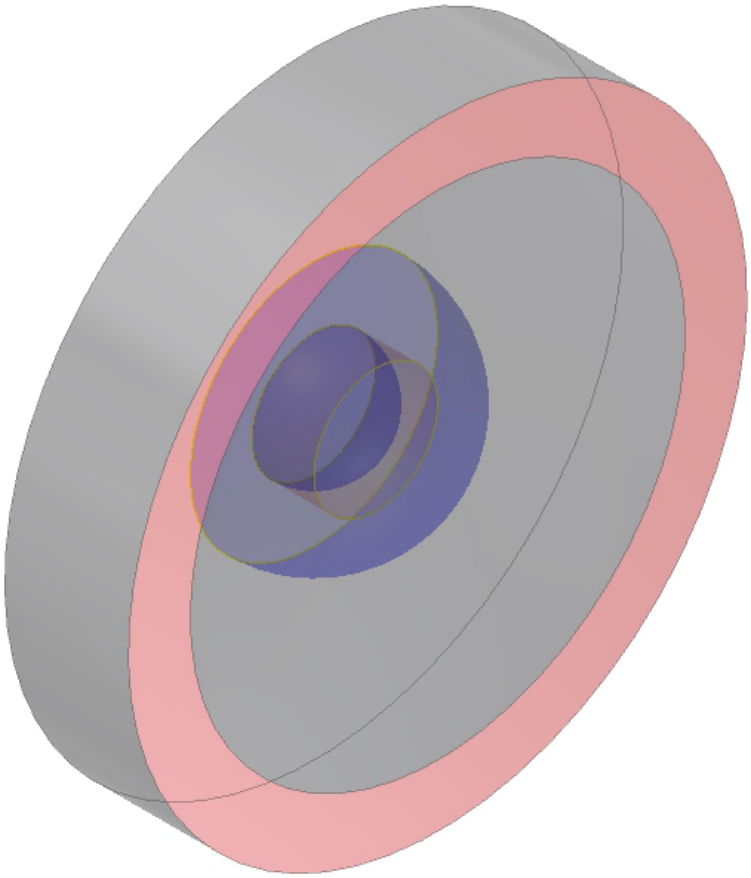

Figure A.1: Heat transfer stages used to calculate maximum charge deposition in FPD: Cylinder for #1 in yellow, two hemispheres for #2 in blue, larger blue hemisphere to edge of gray disk for #3, and through red Kapton ring for #4. Drawing not to scale.

(see figure A.1):

1. From a thin disk on the surface of the center of the FPD, where power is deposited, to a cylinder with the same height as the deposition radius.

2. From the hemisphere contained by the cylinder from the first region, to a hemisphere with the same radius as the thickness of the wafer.

3. From the hemisphere of the second step to edge of the wafer.

4. From the edge of the wafer to the flange.

A.1.1 Deposition Disk to Cylinder

Heat flux is restricted to be parallel to the axis of the wafer.

$$q(x) = \frac{P}{\pi r^2} \tag{A.1}$$

This gives a temperature rise of:

$$\triangle T = \int_0^r \frac{q(x)dx}{k} = \frac{P}{k\pi r} \tag{A.2}$$

The overall heat transfer coefficient for this stage is:

$$U_d = \frac{P}{\triangle T} = k\pi r \tag{A.3}$$

where r is the radius of the hemisphere energy is deposited over. Assume the deposition depth is small and all the power (P) is deposited on the surface.

Thermal conductivity (k) for silicon is lower at higher temperature, use the value of $76\,{}^{\mathrm{W}}/_{\mathrm{m\cdot K}}$ for silicon at 500 K to be conservative.

A.1.1.1 Radius of Deposition

Assume the radius is the radius of gyration for electrons accelerated by the main spectrometer that just barely made it through the pinch magnet, so all their kinetic energy is in transverse motion at the pinch magnet.

$$v_{\perp pinch} = \sqrt{\frac{2\,E}{m}} \tag{A.4}$$

$$v_{\perp det} = v_{\perp pinch}\sqrt{\frac{Bdet}{Bpinch}} \tag{A.5}$$

$$r = \frac{m\,v_{\perp}}{e\,B} = \frac{1}{e}\sqrt{\frac{2\,m\,E}{Bdet\,Bpinch}} \tag{A.6}$$

$$U_d = \frac{k\pi}{e}\sqrt{\frac{2\,m\,E}{Bdet\,Bpinch}} \tag{A.7}$$

where e is the electron charge. Assuming: magnetic field of the pinch magnet (B_{pinch}) is 6 T, of the detector magnet (B_{det}) is 3.6 T, and the electron kinetic energy (E) is 20 keV (maximum of the electron source) results in $r = 100$ μm.

U_d increases as the square root of the applied potential, but power increases linearly with applied potential. So assuming a higher voltage is conservative.

$U_d = 25\,{}^{\mathrm{mW}}/_{\mathrm{K}}$.

A.1.2 Hemispherical Region

Restrict heat flux to be radial from the center of face of wafer. This has a small amount of double coverage with the previous region.

$$q(r) = \frac{P}{2\pi r^2} \tag{A.8}$$

$$\triangle T = \int_r^t \frac{q(r)dr}{k} = \frac{P(1/r - 1/t)}{2\pi k} \tag{A.9}$$

$$U_s = \frac{P}{\triangle T} = \frac{2\pi k}{1/r - 1/t} \tag{A.10}$$

The thickness of the wafer (t) is 500 μm. $U_s = 62\,^{\mathrm{mW}}/_{\mathrm{K}}$.

A.1.3 Wafer Region

Restrict flux to be parallel to plane of wafer.

$$q(r) = \frac{P}{2\pi r\, t} \tag{A.11}$$

$$\triangle T = \int_{r_1}^{r_w} \frac{q(r)dr}{k} = \frac{P\, ln\, \frac{r_w}{r_1}}{2\pi k\, t} \tag{A.12}$$

$$U_w = \frac{2\pi k\, t}{ln\, \frac{r_w}{r_1}} \tag{A.13}$$

where r_w is the radius of the wafer and r_1 is the distance from the wafer axis to the edge of the hemispherical region for the heat transfer along the plane parallel to the wafer. Restricting the flux parallel to the wafer and integrating over the wafer thickness, r_l changes over the depth in the wafer.

$$U_w = k \int_0^t \frac{2\pi dz}{ln\, r_w - \frac{1}{2} ln\, (t^2 - z^2)} \tag{A.14}$$

Integrate the geometry factor numerically. The result differs slightly from assuming a cylinder with the same radius as the wafer thickness, but as it is a smaller result it is less conservative to use a cylinder approximation.

The FPD wafer radius is 57 mm.

$\int_0^t \frac{2\pi dz}{ln\, r_w - \frac{1}{2} ln\, (t^2 - z^2)} = 627$ mm

$U_w = 48\,^{\mathrm{mW}}/_{\mathrm{K}}$

A.1.4 Wafer to Flange

$$U_f = \frac{A}{\frac{1}{h_1} + \frac{1}{h_2} + \frac{t}{k}} \tag{A.15}$$

Area of contact (A) is 2400 mm^2.

Thermal conductivity (k) for Kapton is 0.12 $^{\mathrm{W}}/_{\mathrm{m \cdot K}}$.

For the thermal contacts h_1 and h_2, silicon to Kapton, and Kapton to steel, assume they are no worse than lapped aluminum. The pressure is 10 kPa which for lapped aluminum in vacuum yields a contact conductance around 100 $^{\mathrm{W}}/_{\mathrm{m^2 K}}$.

$U_f = 115\ ^{\mathrm{mW}}/_{\mathrm{K}}$

A.1.5 Overall

$$U = \frac{1}{\frac{1}{U_d} + \frac{1}{U_s} + \frac{1}{U_f} + \frac{1}{U_f}} \tag{A.16}$$

$U = 12\ ^{\mathrm{mW}}/_{\mathrm{K}}$

Assume an allowed temperature rise of 200K and calculate the maximum continuous current:

$$I = e\frac{P}{E} = e\frac{U \triangle T}{E} \tag{A.17}$$

The deposition radius was calculated for 20 kV, assume another 30 kV is added by post acceleration and that the electric field is parallel to the magnetic field. Thus the power is higher, but the area it is deposited over is unchanged by post acceleration.

Maximum continuous current is 46 μA, PULCINELLA will over-range at 600 pA.

A.2 Maximum Instantaneous Charge Derivation

Assume the depth is the penetration depth at the maximum pitch angle.

The overall heat capacity is:

$$C = c\pi r^2 d \tag{A.18}$$

For 50 kV electrons in silicon the penetration depth (d) is: 4.9 μm$\sqrt{1 - \frac{B_{det}}{B_{pinch}}} = 3.1$ μm.

r was calculated in section A.1.1.1.

Specific heat capacity (c) of silicon is $1.64\,{}^{\mathrm{J}}/_{cm^3\mathrm{K}}$.

$C = 160\,{}^{\mathrm{nJ}}/_{\mathrm{K}}$

Assume a 200 K allowed temperature rise:

$$\triangle T = \frac{Q\,E}{e\,C} \tag{A.19}$$

This gives a maximum instantaneous charge deposition of:

$$Q = \frac{e\,C\,\triangle T}{E} \tag{A.20}$$

$Q = 640$ pC. PULCINELLA will over-range at 6 pC.

Appendix B

ELECTRON SOURCE ILLUMINATION LED DRIVE CIRCUIT

B.1 Description

The UV LEDs are driven by individual op-amp voltage-to-current transducers, driven by a common input but with individually adjustable gains to control relative LED intensity (see figure B.2). In parallel with the LED is a current path with a Zener diode in series with a FET, and another parallel path with only a FET. Current is initially applied with the Zener diode containing path conducting, but not the path with just a FET. The 4.7 V Zener diode reverse-bias-breakdown voltage is just below the minimum LED forward-bias voltage of 5V, and this charges up the LED capacitance. When the Zener diode containing bypass path is opened the LED quickly turns on as the LED capacitance is precharged. The current path with only a FET is used to quickly discharge the LED to turn it off. The $0.39\,\mu$F pulse-bypass capacitor and the $50\,\Omega$ series combination of the current-sensing resistor (R_S) and pulse-current-limiting resistor (R_P) limit the LED to a current pulse of 200 mA for 10 μs. The $175\,\Omega$ combination of the DC-limiting resistor (R_{DC}), the pulse-limiting resistor, and the current-sensing resistor, limited the DC current to 30 mA. These are the maximum ratings of the LED. The 10 pF feedback capacitor stabilizes the op-amp to prevent high-frequency oscillation.

The LED amplitude is set by a common analog voltage, and each UV LED has an attenuation stage to adjust relative gain. The timing is accomplished by the circuit of monostable multivibrators (see figure B.1). The FET drive signals from the timing circuit pass though ultra-high current pin drivers (EL7158 from Intersil) to improve switching time. The pin drivers have a high voltage output for a logic zero input, inverting the polarity of the drive signal from the timing circuit.

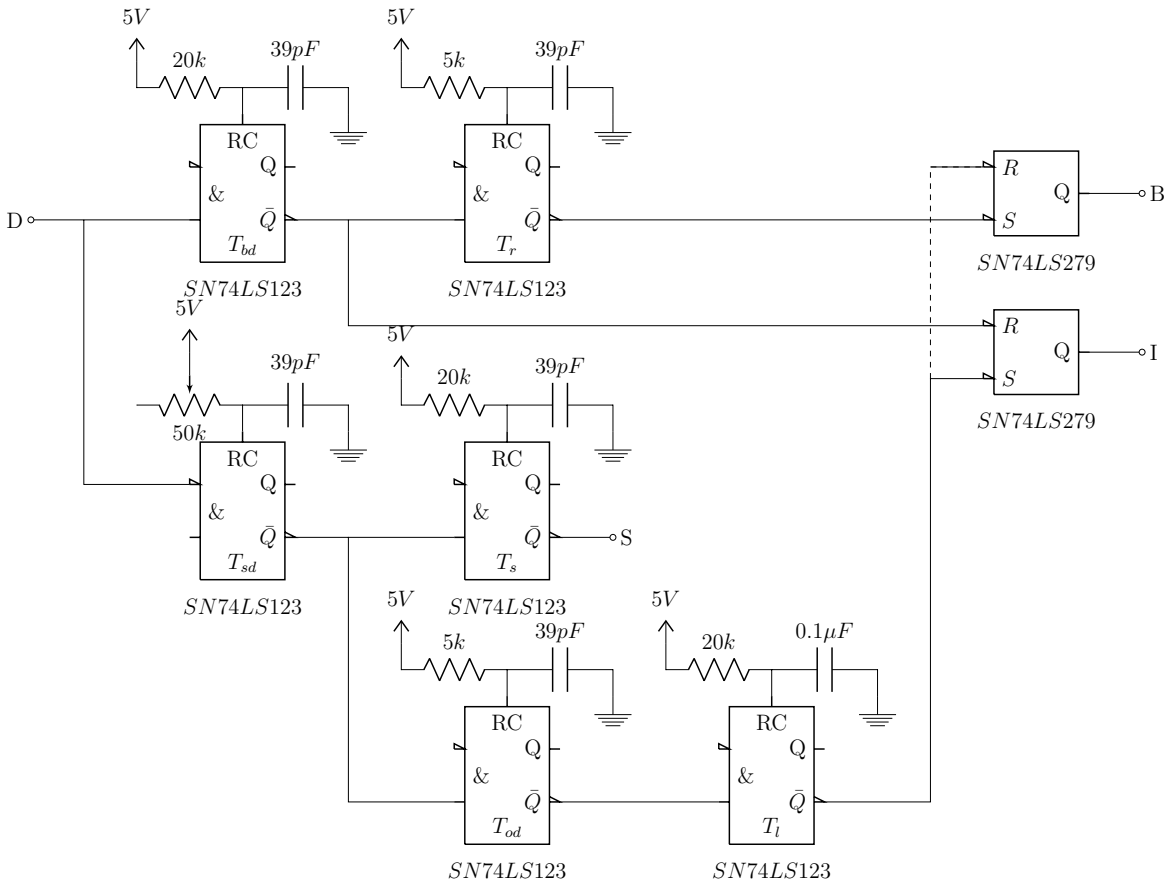

Figure B.1: LED timing circuit using monostable multivibrators and RS flip-flops.

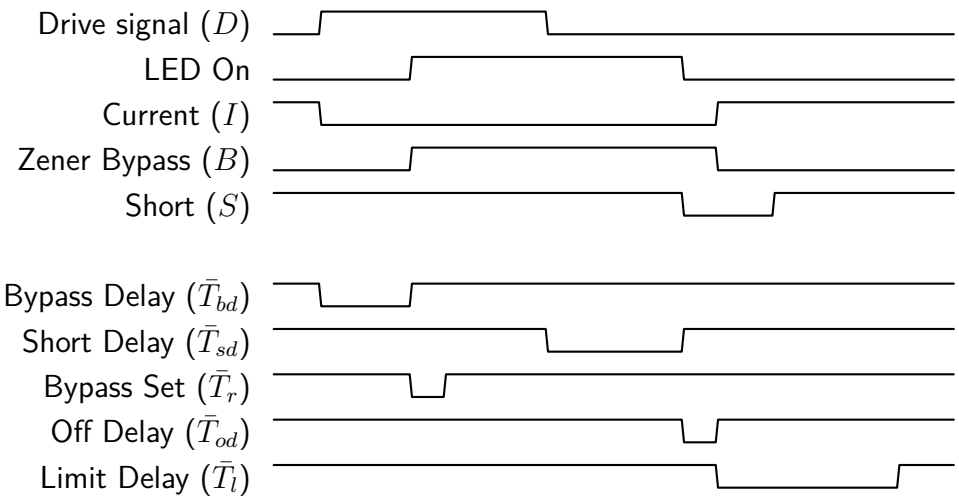

B.2 Timing

Initially I is high (current switch is open), B is low (Zener bypass switch is shut), and S is high (short circuit bypass switch is open). When a pulse comes in on D:

- On rising edge of D, I goes low and current starts to flow charging the LED capacitance up to the Zener diode reverse-bias-breakdown voltage.

- T_{bd} (400 ns) after the rising edge of D, B goes high, which removes the Zener diode containing bypass current path and the LED turns on.

- T_{sd} (100 to 1100 ns) after the falling edge of D, S goes low, which turns on the short-circuit bypass and turns the LED off.

- T_o (150 ns) after S goes low, I goes high and B goes low, turning off current and turning on the Zener diode containing bypass path.

- T_s (400 ns) after S goes low, S goes high removing the short-circuit path. T_s is sufficiently longer than T_d to ensure current stops flowing before the LED is no longer shorted.

T_{sd} adjusts the LED pulse width compared to the input pulse width. T_l of 800 ns prevent pulsing significantly faster than 1kHz.

A red LED is also included to measure the linearity of the detector. The red LED is mounted in a light pipe in the middle of the UV LEDs. The LED is driven by a similar circuit as the UV LED (see figure B.2), but with different resistances and a forward-biased silicon diode instead of a Zener diode. The current-sensing resistor is $5\,\Omega$, the pulse-current-limiting resistor is $5\,\Omega$, the DC-limiting resistor is $330\,\Omega$, and the pulse-bypass capacitor is $1\,\mu$F. This limits the pulse current to 1 A for $10\,\mu$s, and the DC current to 30 mA, which are the limits of the LED. A photodiode (ODD-1 from Opto Diode) is used to provide a direct measurement of the light from the LED. The light is measured with an op-amp integrating circuit with a $22\,\mu$s time constant (see figure B.3). The feedback and non-inverting input have matched components so that both respond the same to transients and provide a stable output.

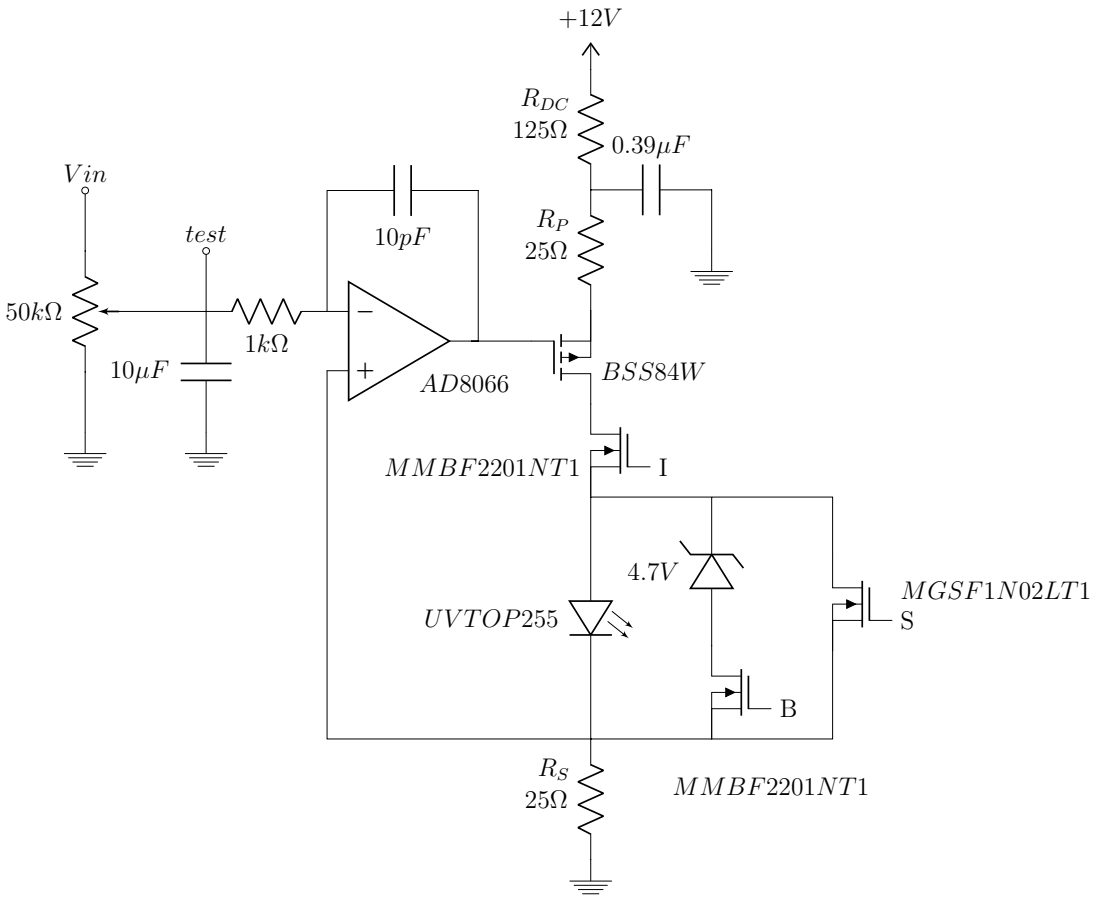

Figure B.2: UV LED driver circuit.

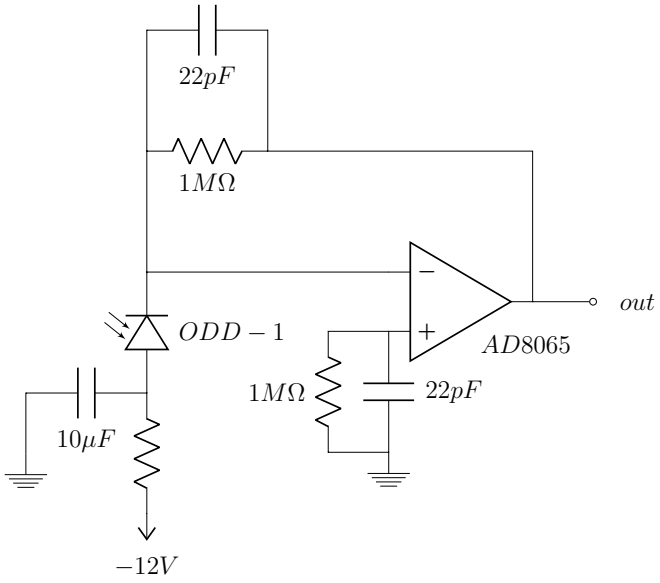

Figure B.3: Red LED sensor circuit. Generates an output proportional to the integral of the light sensed by the photodiode.